Interface tracking method for prediction of droplet motion in the presence of solid geometry

Abhinav Dhar

(Degree)
博士（工学）

(Date of Degree)
2015-03-25

(Date of Publication)
2016-03-01

(Resource Type)
doctoral thesis

(Report Number)
甲第6445号

(URL)
https://hdl.handle.net/20.500.14094/D1006445

Doctoral Dissertation

Interface tracking method for prediction of droplet motion in the presence of solid geometry

固体存在下の液滴挙動を予測するための界面追跡法に関する研究

January 2015

Department of Mechanical Engineering, Graduate School of Engineering,
Kobe University

Abhinav Dhar

Table of Contents

List of Tables

List of Figures

Nomenclature

A_F	area fraction of the fluid phase	
b	pitch between two adjacent tubes	[m]
C	Courant number	
Ca	Capillary number	
CLSVOF	coupled level set and volume-of-fluid	
D	channel width	[m]
DA	donor-acceptor	
d	diameter of bubble/drop	[m]
d_T	tube diameter	[m]
d_v	hydraulic diameter of the tube	[m]
E_S	error in shape	
E_V	error in total volume conservation	
Err_P	error in pressure	
$\boldsymbol{F}_{ST}$	surface tension force per unit volume	[N/m^3]
f_{tube}	friction factor across a bundle of cylindrical tubes	
$\boldsymbol{g}$	acceleration due to gravity	[m^2/s]
H	height of water column	[m]
h	height of the interface from a reference base	[m]
IB	immersed boundary	
J	flux of the phase indicator	[m^3]
L	width of water column	[m]
La	Langmuir number	
$\boldsymbol{N}$	normal to the interface	[1/m]
N	aspect ratio of water column	
N_T	number of tube	
n_c	effective number of tubes per unit length of the cross-section	[1/m]

$\boldsymbol{n}$	unit normal to the interface	
P	pressure	[Pa]
R	radius of drop	[m]
Re_v	Reynolds number	
$\boldsymbol{S}$	surface element vector of a cell face	[m^2]
Se	Surface coverage of the surfactant	
s	normalized coordinate	
T	height of the computational domain	[m]
T^*	normalized time	
THAINC	tangent of hyperbola with adaptive slope for interface capturing	
THINC	tangent of hyperbola for interface capturing	
t	time	[s]
U_{CL}	velocity of contact line	[m/s]
U_{in}	channel inlet velocity	[m/s]
U_{max}	maximum velocity between the tubes	[m/s]
$\boldsymbol{V}$	velocity	[m/s]
$\boldsymbol{V}_{MAX}$	maximum spurious current	[m/s]
V_{IM}	impact velocity	[m/s]
V_T	terminal velocity of air bubble	[m/s]
VOF	volume-of-fluid	
W	width of the computational domain	[m]
We	Weber number	
WLIC	weighted linear interface calculation	
Z	water front tip position	[m]
Z^*	normalized water front tip position	

Greek symbols

α	volume fraction of a phase with respect to the cell	
Δt	time step size	[s]
Δx	cell size in the x-direction	[m]
Δy	cell size in the y-direction	[m]
Δz	cell size in the z-direction	[m]
δ	delta function	
ζ	line fraction of the fluid at an edge	
η	volume fraction of a phase in the fluid	
κ	mean curvature of the interface	[1/m]
μ	viscosity	[Pa·s]
θ	volume of computational cell	[m^3]
ρ	density	[kg/m^3]
σ	surface tension between gas and liquid phases	[N/m]
τ	artificial time	
ϕ	level set function	
ϕ_0	level set function at the beginning of the reinitialization	
Φ_D	dynamic contact angle	[deg]
Φ_E	equilibrium contact angle	[deg]
Ω	fluid volume transported through the cell face	[m^3]

Subscript

ALE	arbitrary Lagrangian-Eularian like scheme
BFA	balanced-force algorithm
CSF	continuum surface force model
HF	height function
TH	theoretical value
F	fluid

G	gas phase
i	cell index for x-direction
iD	cell index for donor cell
j	cell index for y-direction
k	cell index for z-direction
L	liquid phase
S	solid phase
x	x-component
y	y-component
z	z-component

Superscript

n	index for time
l	lower value
u	upper value
*	intermediate value after advection in the x-direction
**	intermediate value after advection in the y-direction

Chapter 1

Introduction

1.1 Background

The recent advancement in the field of printing and coating has promoted their application as a manufacturing technique. Some examples are inkjet printing, spin coating, spray coating etc. These are applied to the manufacturing of LEDs, solar cells etc. Inkjet printing has several advantages such as high speed, low cost etc. The complete coating process involves several steps such as injection of a fluid from a nozzle head, coating on a solid surface, drying of the fluid etc. The desired component for coating a surface is generally a solid or liquid with very high viscosity. Hence, the injection fluid is prepared by dissolving the component in a solvent to facilitate the use of inkjet. The component may act as a surface active agent affecting the bulk property of the injection fluid such as surface tension and the quality of the coating process. The problem is complicated by the presence of complex solid geometries such as coating objects and nozzle heads. The shape of nozzles is of vital importance since it affects the drop size as well as the stability and repeatability in the fluid injection. The droplets of interest are often of the sizes ranging from sub-mili to sub-micron meters. These demonstrate the complexity of the problem which involve gas-liquid interface of sub-micron meter length scale in the presence of complicated solid geometry. Each stage in the coating process is affected by the motion of the gas-liquid

interface. Hence, the design and optimization of such processes require in-depth understanding of the dynamic behaviour of a droplet, especially on a solid surface.

The dynamic motion of gas-liquid interface is affected by various factors such as surface tension force, viscous force etc. The surface tension force becomes more and more dominant as the length scale of gas-liquid interface becomes smaller and can be the most dominant force affecting the behaviour of sub-micron meter droplets. The wetting behaviour of a droplet on a solid surface is also affected by the motion of contact line, along which both fluid phases co-exist with the solid. The behaviour in the proximity of contact line is affected by the contact angle, which is the angle between the gas-liquid interface and the solid surface. This contact angle depends on the surface energy of gas-liquid, solid-liquid, and gas-solid interfaces as well as surface roughness.

Analytical solutions of droplet shapes on solid surfaces are available for a few simple cases where the motion of the gas-liquid interface has been neglected (Iwata *et al.*, 2012). The complexity of the geometry, small length scale and current limitations in the measurement techniques often limit the amount of engineering information that is required for design and optimization of coating processes. The progress in the computer performance has enabled us to use computational fluid dynamics (CFD) to predict the behaviour of flows containing gas-liquid interface. Hence, CFD can be an alternative tool that can be used for the design and optimization of coating processes.

Many numerical methods have been developed for simulating flows containing the gas-liquid interface. The interface tracking method is a class of numerical methods that can directly simulate the dynamics of the gas-liquid interface and has been a popular choice for simulating wetting behaviour of a drop (Sikalo *et al.*, 2005; Yokoi, 2009). This method requires the mesh size much smaller than the size of the bubbles/drops in order to be able to adequately resolve the gas-liquid interface, resulting in a high computational cost. The recent progress in the computer performance along with programming techniques such as parallel computing has made it possible to enhance the efficiency of the interface tracking

method in direct numerical simulations of various phenomena occurring around the gas-liquid interface.

Hence, the interface tracking method is appropriate for carrying out the design and optimization of coating processes since the dynamic behaviour of the gas-liquid interface, especially on the solid surface, can be predicted. There are various interface tracking methods such as VOF (Volume-of-Fluid) (Hirt and Nichols, 1981), Level Set (Sussman *et al.*, 1994), Front tracking (Unverdi and Trygvasson, 1992), BFC (Boundary-fitted coordinate) (Ryskin and Leal, 1984) etc.

Most of the experimental and numerical investigation of the dynamic behaviour of the gas-liquid interface has been restricted to millimeter size drops on a simple solid geometry (Sikalo *et al.*, 2005; Yokoi, 2009). Some simulations (Wu *et al*., 2004(a) & (b)) of coating processes involving micron meter size droplets have been carried out in the literature using a conventional method for calculating surface tension force, continuum surface force (CSF) model (Brackbill *et al*. ,1992). This method has been reported to suffer from relatively large numerical errors (Rudman, 1998). Apart from the surface tension force calculation, errors are also introduced due to inappropriate handling of solid objects. For example, tapered nozzle head was generated using stair-step configuration in a structured orthogonal mesh such that the computational cells were either completely filled with solid or fluid as shown in Fig. 1.1. These are rough boundaries and would cause numerical errors.

(a) Nozzle shape (b) Nozzle in the simulation

Fig. 1.1 Inkjet nozzle

A numerical method which can accurately predict the behaviour of sub-micron meter droplets in the presence of complex solid geometries is required to obtain useful information such as the effect of nozzle shape on the droplet size, dynamic wetting behaviour of sub-micron droplets on a solid surface etc. for design and optimization of coating processes. Hence, along with the ability to handle the presence of complex solid geometries, the method must accurately estimate the surface tension force and ensure a proper treatment at the contact line at such small length scales of the gas-liquid interface. The method should not be computationally intensive to ensure practical applicability to industrial problems.

1.2 Interface tracking method

Various numerical methods can be classified under the interface tracking method. Tomiyama *et al.* (2006) compared and summarized their respective characteristics as shown in Table 1.1. The details of these methods will be discussed in this section.

Table 1.1 Comparison of different interface tracking methods

A: Excellent, B: Good, C: Poor

Requirements	VOF	Front tracking	Level set	BFC
(a) Volume conservation	B	A	C	A
(b) Interface sharpness	B	B	B	A
(c) Surface tension force	C	A	A	A
(d) Density ratio	A	C	A	C
(e) Multiple interface	A	A	C	C

1.2.1 BFC

The BFC method has been used to study the motion of gas-liquid interface (Takagi *et al.*, 1997; Ponoth and Mclaughlin, 2000). An orthogonal mesh is generated such that the gas-liquid interface coincides with one of the boundaries of the computational domain (Duraiswami and Properetti, 1992) as shown in Fig. 1.2. The governing equations for the motion, transformed into the orthogonal curvilinear coordinates, are solved over the generated mesh. The mesh points on the bubble surface are then transported using the calculated velocity in a Lagrangian way to determine the shape of the interface at the next time step. This method has good volume conservation and interface sharpness but is poor at handling systems consisting of high density ratio and multiple interfaces. It is also computationally intensive as the mesh has to be recalculated at each time step.

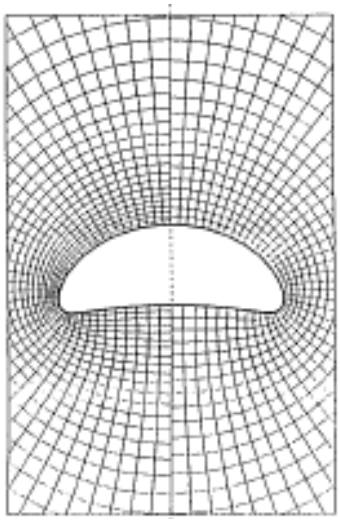

Fig. 1.2 Grid in boundary-fitted coordinate (Takagi *et al.*, 1997)

1.2.2 Front tracking

This method was first developed by Unverdi and Trygvasson (1992) and has been improved to deal with several problems involving the motion of gas-liquid interface. The

gas-liquid interface is marked with connected marker points as shown in Fig. 1.3. The marker points are connected using elements which is a line in two-dimensions and a triangular face in three-dimensions. These are advected in a Lagrangian way based on the velocity field obtained by solving the governing equations for the flow on a fixed grid. The location of marker points is updated by

$$\frac{\mathrm{d}\boldsymbol{x}_p}{\mathrm{dt}} = \boldsymbol{V}_p \tag{1.1}$$

where $\boldsymbol{x}_p$ is the location of a marker point and $\boldsymbol{V}_p$ the velocity at that point. The front tracking method, while having good volume conservation and easiness of evaluation of surface tension force, cannot easily deal with fluid systems of high density ratios which are usually common in industrial problems. Also, the topological changes such as coalescence and breakup of bubbles and drops require special treatment in the front tracking method.

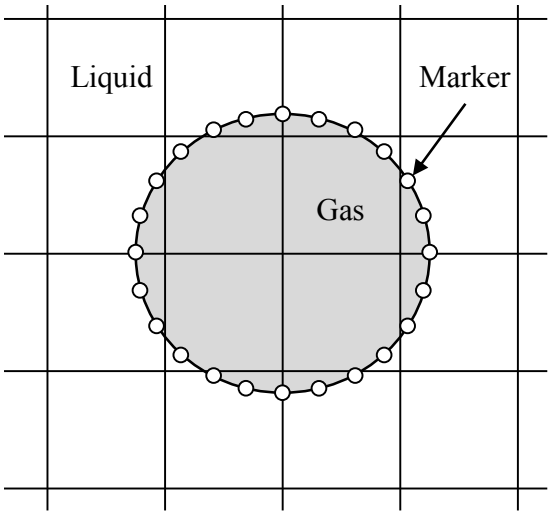

Fig. 1.3 Gas-liquid interface marked by a front

1.2.3 Level set

The level set method was originally introduced by Osher and Sethian (1988) and further developed by Sussman *et al.* (1994). The interface is represented using the level set function, ϕ. It is the signed normal distance, a, from the interface such that it is positive in the liquid phase and the negative in the gas phase:

$$\phi(x) = \begin{cases} +a, & \text{if } x \text{ is in the liquid phase} \\ -a, & \text{if } x \text{ is in the gas phase} \end{cases} \tag{1.2}$$

where x is a point in space. The interface is represented by $\phi = 0$ as shown in Fig. 1.4. The level set function is transported by

$$\frac{\partial \phi}{\partial t} + \boldsymbol{V} \cdot \nabla \phi = 0 \tag{1.3}$$

where t is the time and $\boldsymbol{V}$ the velocity. ϕ has been reported to lose the property of the distance function after being transported for a couple of time steps (Prosperetti and Tryggvason, 2007) which results in an overall loss of accuracy such as volume conservation. Hence, it is necessary to reinitialize the level set function to keep ϕ as a signed distance function. Sussman *et al.* (1994) proposed an iterative approach to reinitialize ϕ using

$$\frac{\partial \phi}{\partial \tau} = \mathrm{sgn}(\phi_0)(1 - |\nabla \phi|) \tag{1.4}$$

where τ is an artificial time, ϕ_0 the initial ϕ at the beginning of the reinitialization, and sgn the sign function defined by

$$\mathrm{sgn}(\phi_0) = \begin{cases} 1, & \phi_0 > 0 \\ 0, & \phi_0 = 0 \\ -1, & \phi_0 < 0 \end{cases} \tag{1.5}$$

The local interface curvature calculated using the level set function is accurate due to the continuous nature of the level set function. Hence, the level set method is able to accurately evaluate the surface tension force which is very important for accurate prediction of the motion of gas-liquid interface but suffers from errors in volume conservation as well as numerical diffusion of the interface. Several approaches have been proposed to solve these problems such as the use of a finer grid for the advection of the level set function as compared to the flow equations (Hermann, 2008), conservative level set methods (Olsson *et al.*, 2007) etc. But these can also be considered to further increase the computational cost since they involve the iterative reinitialization or finer grids.

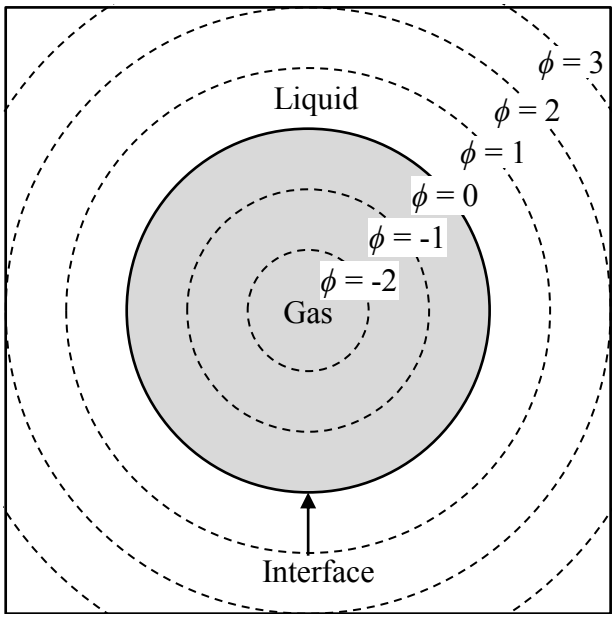

Fig. 1.4 Level set function distribution for a gas bubble

1.2.4 VOF

The origin of this method can be traced back to the work of Noh and Woodward (1976) but has been popularized by Hirt *et al.* (1981). The interface is represented with the help of the volume fraction of a fluid phase, α, in the computational cell. As an example, α is 1

when the cell is completely filled with the gas phase and 0 when it is completely filled with the liquid phase as shown in Fig. 1.5. A value between 0 and 1 denotes the presence of an interface. The volume fraction is advected based on the following transport equation:

$$\frac{\partial \alpha}{\partial t} + \boldsymbol{V} \cdot \nabla \alpha = 0 \tag{1.6}$$

The key point of this method is the accurate reconstruction/representation of the interface for accurate transport of the gas-liquid interface without causing numerical diffusion of the interface. Several schemes have been proposed to carry this out (Kunugi, 1997; Rider and Kothe, 1998; Xiao *et al.*, 2005; Yokoi, 2007). While none of them are iterative in nature as compared to the level-set method, they have their own limitations such as difficulty in extension to three-dimensions, shape preservation etc. The errors are also caused in the evaluation of surface tension force when using a conventional method (Brackbill *et al.*, 1992) with the volume fraction. The VOF method is able to handle large density ratios with good volume conservation but requires a sufficient resolution. As an example, the number of cells required for reasonable prediction of bubbles or drops should be greater than 5 (Cerne *et al.*, 2002).

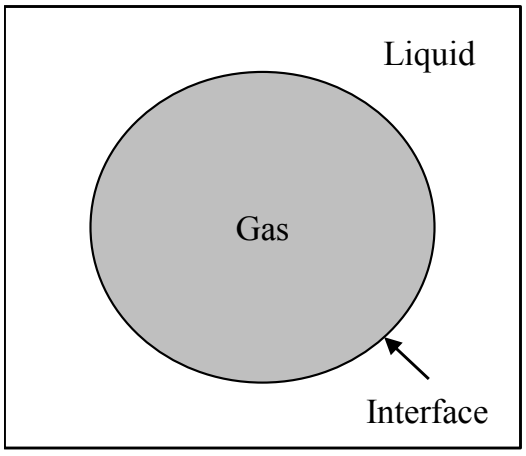

0	0	0	0	0	0
0	0.3	0.8	0.8	0.3	0
0	0.8	1	1	0.8	0
0	1	1	1	1	0
0	0.8	1	1	0.8	0
0	0.3	0.8	0.8	0.3	0
0	0	0	0	0	0

Fig. 1.5 Volume fraction distribution

1.3 Treatment of complex solid geometries in the flow domain

Many industrial problems also consist of complex geometries around or within the flow domain. Most of the methods, however, have been restricted to simple geometries such as rectangular and cylindrical domains. One of the reasons for this restriction is the use of a structured grid. Although it facilitates programming, it suffers from problems when dealing with complex geometries. Some of the methods for handling the complex geometries are shown in Fig. 1.6. The stair-step configuration for the complex boundary is easy to implement but yields inaccurate results especially when sharp changes in the topology is present. Commercial codes adopt unstructured grids. In lieu of the benefit of an accurate treatment of flow geometry, the code may suffer performance shortfalls with respect to (1) the degree of accuracy, (2) ease of programming, (3) memory size, and (4) CPU time. The other methods, such as boundary-fitted coordinates (Koshizuka *et al.*, 1990) and block cells (Landsberg, 1997), were developed to deal with complex geometries by using the structured grids. However, they have their own limitations such as instability and high computational costs.

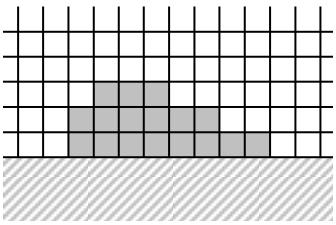

(a) Stair-step

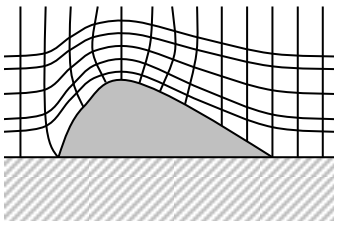

(b) Boundary-fitted coordinates

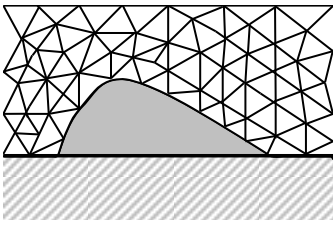

(c) Unstructured grid

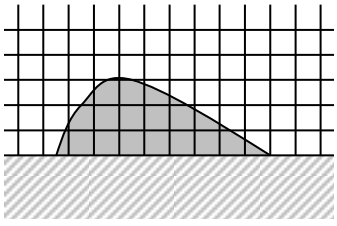

(d) Immersed boundary

Fig. 1.6 Numerical techniques for handling the presence of complex geometries in the flow domain

The immersed boundary (IB) method deals with the shape of a solid body in an orthogonal structured grid. This method was developed by Peskin (1977), and recently has been actively pursued by many researchers. It can be further categorized based on differences in treatments of the solid geometry (Briscolini and Santangelo, 1989; Goldstein *et al.*, 1993; Tuanya *et al.*, 2009; Fadlun *et al.*, 2000; Kim *et al.*, 2001). The immersed boundary methods predict the flow consisting of complex solid geometries based on structured grids and hence do not suffer from the performance shortfalls mentioned above. Most of the studies based on immersed boundary methods are, however, limited to single phase flows.

1.4 Objectives

A versatile numerical method is necessary for a better understanding of phenomena associated with the motion of gas-liquid interface in the presence of complex solid geometries for better design and optimization of coating processes. The above discussion suggests VOF as a promising method for predicting the motion of gas-liquid interface if the errors in surface tension calculation that are found in conventional methods can be eliminated. Several numerical methods for surface tension force evaluation with low numerical errors have been proposed recently but their performance at sub-micron meter length scale and in the presence of solids is still unknown, and therefore, must be investigated to ensure applicability to coating processes. The immersed boundary method is suitable for the handling of the presence of complex solid geometries in and around the flow domain. Hence, the combination of VOF and immersed boundary method would be suitable to coating problems. In addition, the method must satisfy the following requirements for practical applicability:

(1) The numerical method should be easily programmed and with low computational cost.

(2) The volume conservation and the interface sharpness must be preserved.

(3) Presence of complex solid geometries in two-phase flow problems must be handled.

(4) Behaviour of droplets of sub-micron sizes can be accurately predicted.

(5) Fluid systems contaminated with surface-active agents must be effectively handled.

A new numerical method with the above mentioned features will be proposed in this study and its applicability to problems involving drops of sizes ranging from mili to sub-micron meters as well as contamination will be checked by comparing the predicted results with experimental results.

1.5 Preview

In Chapter 2, a simple yet efficient interface tracking method is proposed which can predict the motion of gas-liquid interface. The accuracy of the proposed method is validated by carrying out one-, two- and three-dimensional advection tests. The results are also compared with the existing methods to demonstrate the performance of the proposed method. Then, simulations of a rising bubble and a drop on a solid surface are carried out and compared with the results reported in the literature.

In Chapter 3, an immersed boundary method is implemented into the developed interface tracking method to enable it to handle the presence of complex solid geometries. The occurrence of errors in advection due to the presence of solid in the computational cell is checked by carrying out advection tests. Next, the proper implementation of the immersed boundary method in the flow calculation is checked by carrying out simulation of single phase flow past a staggered arrangement of cylindrical tubes and comparing the pressure drop across the tube bundles obtained from the simulation with the results reported in the literature. Finally, simulation of two-phase flow past the same staggered arrangement of cylindrical tubes and the dam-break problem in the presence of a triangular dyke is

carried out to demonstrate the ability of the method to predict the motion of gas-liquid interface in the presence of complex solid geometries.

In Chapter 4, the effect of numerical treatments for evaluation of surface tension force on the prediction of gas-liquid interface motion is investigated. The effect of drop size and wall treatment on the errors is also investigated to ensure the applicability to processes involving sub-micron droplets by carrying out numerical tests on neutrally buoyant droplets and droplets adhering to walls. Next, the motion of a clean water drop on a solid surface is predicted using the method for surface tension force with the lowest errors and compared with the experimental results. Finally, the motion of a sub-micron meter clean water droplet on a solid surface is also predicted to check the applicability to droplets in practical coating processes.

In Chapter 5, the developed numerical method is applied to problems containing contamination. Falling contaminated drop experiments are carried out and data such as contact angle are obtained using image processing. The reliability of the experimental data is also checked. The contact angle obtained from the experiment is modelled using a dynamic contact angle model. The motion of contaminated drops on a solid surface is predicted and compared with the experimental results. Finally, a simulation of a coating process is carried out to demonstrate the applicability of the proposed method to practical problems.

In Chapter 6, the concluding remarks of this study are summarized.

References

Brackbill, J., Kothe, D., Zemach, C., A continuum method for modeling surface tension, *Journal of Computational Physics*, 1992, 100, pp. 335–354.

Briscolini, M., Santangelo, P., Development of the mask method for incompressible unsteady flows, *Journal of Computational Physics*, 1989, 84, pp. 57-75.

Cerne, G., Petelin, S., Tiselj, I., Nuemrical errors of the volume-of-fluid interface tracking algorithm, *International Journal for Numerical Methods in Fluids*, 2002, 38, pp. 329-350.

Duraiswami, R., Prosperetti, A., Orthogonal mapping in two dimensions, , *Journal of Computational Physics*, 1992, 98, pp. 254-268.

Fadlun, E. A., Verzicco, R., Orlandi, P., Mohd-Yusof, J., Combined immersed-boundary finite-difference methods for three-dimensional complex flow simulations, *Journal of Computational Physics*, 2000, 161, pp. 35-60.

Goldstein, D., Handler, R., Sirovich, L., Modeling a no-slip flow boundary with an external force field, *Journal of Computational Physics*, 1993, 105, pp. 354-366.

Hermann, M., A balanced force refined level set grid method for two-phase flows on unstructured flow solver grids, *Journal of Computational Physics*, 2008, 227, pp. 2674-2706.

Hirt, C. W., Nichols, B. D., Volume of fluid (VOF) method for the dynamics of free boundaries, *Journal of Computational Physics*, 1981, 39, pp. 201-225.

Iwata, S., Suzuki, H., Mori, H., Measurement of Surface Tension and Contact Angle by Analysis of Force Balance along a Bubble/Droplet Surface, *Kagaku Kougaku Ronbunshu*, 2010, 36, 2, pp. 441-448.

Kim, J., Kim, D., Choi, H., An immersed-boundary finite-volume method for simulations of flow into complex geometries, *Journal of Computational Physics*, 2001, 171, pp. 132-150.

Koshizuka, S., Oka, Y., Kondo, S., A staggered differencing technique on boundary-fitted curvilinear grids for incompressible flows along curvilinear or slant walls, *Computational Mechanics*, 1990, 7, pp. 123-136.

Kunugi, T., Direct numerical algorithm for multiphase flow with free surfaces and interfaces, *Nihon Kikai Gakkai Ronbunshu*, 1997, 63, 609, pp. 1576 – 1584.

Landsberg, A. M., The virtual cell embedding method: A simple approach for gridding complex geometries, *AIAA*, 1997, 97-1982.

Noh, W. F., Woodward, P. R., SLIC (simple line interface method), *Lecture notes in Physics*, 1976, 59.

Olsson, E., Kreiss, G., Zahedi, S., A conservative level set method for two phase flow, *Journal of Computational Physics*, 2007, 225, pp. 785-807.

Osher, S., Sethian, J. A., Fronts propogating with curvature-dependant speed: Algorithms based on Hamilton-jacobi formulations, *Journal of Computational Physics*, 1988, 79, pp. 12-49.

Peskin. C. S., Numerical analysis of blood flow in the heart, *Journal of Computational Physics*, 1977, 25, pp. 220-252.

Ponoth, S. S., Mclaughlin, J. B., Numerical simulation of mass transfer for bubbles in water, *Chemical Engineering Science*, 2000, 55, pp. 1237-1255.

Prosperetti, A., Tryggvason, G., Computational methods for multiphase flows, *Cambridge University Press*, 2007.

Rudman, M., A volume-tracking method for incompressible multifluid flows with large density variations, *International Journal for Numerical methods in Fluids*, 1998, 28, pp. 357-378.

Ryskin, G., Leal, L. G., Numerical solutions of free-boundary problems in fluid mechanics. Part 1. The finite-difference technique, *Journal of Fluid Mechanics*, 1984, 148, pp. 1-17.

Sikalo, S., Wilhelm, H. D., Roisman, I. V., Jakirlic, S., Tropea, C., Dynamic contact angle of spreading droplets: Experiments and simulations, *Physics of Fluids*, 2005, 17, 6, 062103, pp. 1-13.

Sussman, M., Smereka, P., Osher, S., A level set approach for computing solutions to incompressible two-phase flow, *Journal of Computational Physics*, 1994, 114, pp. 146-159.

Takagi, S., Matsumoto, Y., Huang, H., Numerical analysis of a single rising bubble using boundary-fitted coordinate system, *JSME International Journal*, 1997, 40, 1, pp. 42-50.

Rider, W. J., Kothe, D. B., Reconstructing volume tracking, *Journal of Computational Physics*, 1998, 141, pp. 112–152.

Takewaki, H., T.,Yabe, The Cubic-Interpolated Pseudo Particle (CIP) Method: Application to Nonlinear and Multi-Dimensional Hyperbolic Equations, , *Journal of Computational Physics*, 1987, 70, pp. 355-372.

Tomiyama, A., Sakoda, K., Hayashi, K., Sou., A., Shimada, N., Hosokawa, S., Modelling and hybrid simulation of bubbly flow, *Multiphase Science and Technology*, 2006, 18, pp. 73-110

Tuanya T. M. Y. S., Takeuchi, S., Kajishima, T., Ueyama, A., Immersed boundary method (body force) for flow around thin bodies with sharp edges, *International Journal of Mechanical and Materials Engineering*, 2009, 4,1, pp. 98-102.

Unverdi, S. O., Tryggvason, G., A front tracking method for viscous, incompressible,

multi-fluid flows, *Journal of Computational Physics*, 1992, 100, pp. 25-37.

Xiao, F., Honma, Y., Kono, T., A simple algebraic interface capturing scheme using hyperbolic tangent function, *International Journal for Numerical Methods in Fluids*, 2005, 48, pp. 1023–1040.

Yokoi, K., Efficient implementation of THINC scheme: A simple and practical smoothed VOF algorithm, *Journal of Computational Physics*, 2007, 226, pp. 1985–2002.

Yokoi, K, Vadillo , D., Hinch J., Hutchings, I., Numerical studies of the influence of the dynamic contact angle on a droplet impacting on a dry surface, *Physics of Fluids*, 2009, 21, 072102, pp.1-12.

Wu, H., Hwang, W., Lin, H., Development of a three-dimensional simulation system for micro-inkjet and its experimental verification, *Materials Science and Engineering*, 2004, 373, pp. 268-278.

Wu., H., Lin, H., Kuo, Y., Hwang, W., Simulation of droplet ejection for a piezoelectric inkjet printing device, *Materials Transcations*, 2004, 45, 3, pp. 893-899.

Chapter 2

Development of a simple interface tracking method based on VOF

2.1 Introduction

The VOF method is suitable for prediction of the dynamic motion of gas-liquid interface and various phenomena affected by it. The method requires modelling of the gas-liquid interface within a computational cell for which several schemes have been proposed. Methods such as multi-interfaces advection and reconstruction (MARS) (Kunugi, 1997) and piecewise linear interface calculation – VOF (PLIC-VOF) (Rider and Kothe, 1998) carry out a geometric reconstruction of the interface within a cell by assuming the interface to be a straight line or a plane, in the case of two-dimensions or three-dimensions respectively. These methods are able to well preserve the sharpness of the interface but are difficult to program and extend to three-dimensional problems. The other methods such as solution algorithm – VOF (SOLA-VOF) (Hirt and Nichols, 1981), cubic-interpolated pseudo particle (CIP) (Takewaki and Yabe, 1987), tangent of hyperbola for interface capturing (THINC) (Xiao *et al.*, 2005) use a mathematical function to reconstruct the gas-liquid interface. These methods are easier to program and can be very easily extended to three-dimensions but suffer from problems such as numerical diffusion of the gas-liquid interface, artificial distortion of the shape etc.

In this chapter, a new method, tangent of hyperbola with adaptive slope for interface capturing (THAINC), is developed for tracking the gas-liquid interface. This method employs a mathematical function similar to THINC (Xiao *et al.*, 2005) for interface reconstruction. Hence, it possesses all the preferable characteristics of THINC such as excellent volume conservation, no overshooting ($\alpha>1$)/under shooting ($\alpha<0$) as well as easy programmability and extension to three-dimensions. The method is also able to well preserve the sharpness of the interface. The problems with THINC such as shape distortion etc. are overcome with this method. Its performance is evaluated based on (1) advection tests, (2) simulation of a rising bubble, and (3) simulation of dynamic wetting behaviour of a drop.

2.2 Numerical method

2.2.1 Transport equation of gas-liquid interface

The motion of gas-liquid interface is tracked by carrying out the transport of a phase-indicator function. The phases are assumed to be immiscible with no phase change and the computational cell is completely occupied by fluid. The volume of a computational cell is therefore given by

$$\theta = \theta_G + \theta_L \tag{2.1}$$

where θ is the volume of the computational cell and the subscripts G and L denote the gas and liquid phases, respectively. The volume fraction, α, of a fluid phase used as the phase-indicator function is defined by

$$\alpha_K = \frac{\theta_K}{\theta} \qquad (K = \mathrm{G}, \mathrm{L}) \tag{2.2}$$

and α_G and α_L satisfy

$$\alpha_G + \alpha_L = 1 \tag{2.3}$$

Since the phases are treated as continuous materials with no phase change, the transport of the volume fraction is then governed by

$$\frac{D_K \alpha_K}{Dt} = 0 \tag{2.4}$$

where D_K/Dt is the material derivative defined by

$$\frac{D_k}{Dt} = \frac{\partial}{\partial t} + \boldsymbol{V}_K \cdot \nabla \tag{2.5}$$

where $\boldsymbol{V}_K$ is the velocity of the phase K. The transport equation for the gas phase can be written by substituting K = G into Eq. (2.4) to obtain

$$\frac{\partial \alpha_G}{\partial t} + \nabla \cdot (\alpha_G \boldsymbol{V}_G) = \alpha_G \nabla \cdot \boldsymbol{V}_G \tag{2.6}$$

Taking the volume average over the computational cell for Eq. (2.6) and using the volume averaged value of α within the computational cell gives

$$\frac{\partial \alpha_G}{\partial t} + \frac{1}{\theta}\int_\theta \nabla \cdot (\alpha_G \boldsymbol{V}_G) d\theta = \frac{\alpha_G}{\theta}\int_\theta \nabla \cdot \boldsymbol{V}_G d\theta \tag{2.7}$$

Applying the divergence theorem

$$\int_\theta \nabla \cdot \boldsymbol{B} d\theta = \int_{\boldsymbol{S}} \boldsymbol{B} \cdot d\boldsymbol{S} \tag{2.8}$$

where $\boldsymbol{B}$ is a vector field and $\boldsymbol{S}$ the surface element vector of θ, to Eq. (2.7) yields

$$\frac{\partial \alpha_G}{\partial t} + \frac{1}{\theta}\int_{\boldsymbol{S}} (\alpha_G \boldsymbol{V}_G) \cdot d\boldsymbol{S} = \frac{\alpha_G}{\theta}\int_{\boldsymbol{S}} \boldsymbol{V}_G \cdot d\boldsymbol{S} \tag{2.9}$$

The gas-liquid interface is tracked by solving Eq. (2.9). A similar equation can be obtained for the liquid phase as well. Since both phases satisfy Eq. (2.3), only the transport equation for the dispersed phase is solved. For the sake of simplicity, α_G will be replaced with α. The discretization is carried out over a staggered grid arrangement, as shown in Fig. 2.1, with scalars, such as α, at the cell center and vectors, such as velocity and flux of α, at the cell faces. The subscripts i, j, and k are indexes for the x, y, and z coordinates, respectively. The cell sizes in the x, y, and z directions are Δx, Δy, and Δz, respectively. The six cell faces for the computational cell at (i, j, k) are located at (i+1/2, j, k), (i−1/2, j, k), (i, j+1/2, k), (i, j−1/2, k), (i, j, k+1/2), and (i, j, k−1/2).

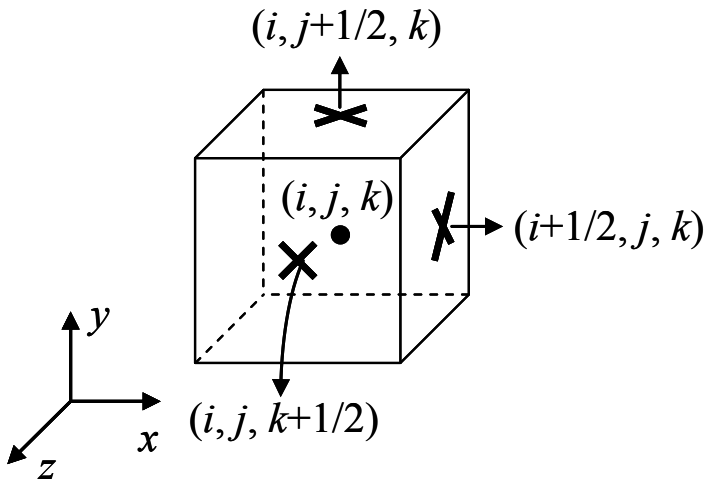

Fig. 2.1 Computational cell

The transport of α is carried out in one direction at a time to ensure that no undershooting or overshooting of α occurs. This is known as directional splitting and is carried out as

$$\alpha^{*} = \alpha^{n} - \left(\frac{J^{n}_{x,i+1/2,j,k} - J^{n}_{x,i-1/2,j,k}}{\theta} \right) + \alpha^{n} \left(\frac{\Omega^{n}_{x,i+1/2,j,k} - \Omega^{n}_{x,i-1/2,j,k}}{\theta} \right) \tag{2.10}$$

$$\alpha^{**} = \alpha^{*} - \left(\frac{J^{*}_{y,i,j+1/2,k} - J^{*}_{y,i,j-1/2,k}}{\theta} \right) + \alpha^{*} \left(\frac{\Omega^{*}_{y,i,j+1/2,k} - \Omega^{*}_{y,i,j-1/2,k}}{\theta} \right) \tag{2.11}$$

$$\alpha^{n+1} = \alpha^{**} - \left(\frac{J^{**}_{z,i,j,k+1/2} - J^{**}_{z,i,j,k-1/2}}{\theta} \right) + \alpha^{**} \left(\frac{\Omega^{**}_{z,i,j,k+1/2} - \Omega^{**}_{z,i,j,k-1/2}}{\theta} \right) \tag{2.12}$$

where the superscript n denotes the value at the current time step, n+1 the value at the new time step, * and ** the intermediate values; J_x, J_y, and J_z the fluxes of α through the cell faces; and Ω_x, Ω_y, and Ω_z the fluid volumes transported through the cell faces.

J_x is calculated as

$$J_{x,i+1/2,j,k} = \int_{x_{i+1/2,j,k} - u_{i+1/2,j,k}\Delta t}^{x_{i+1/2,j,k}} \alpha_{iD}(x) \Delta y \Delta z dx \tag{2.13}$$

where Δt is the time step, u the x-component of the velocity vector, and the subscript iD denotes the donor cell location:

$$iD = \begin{cases} i & , u_{i+1/2,j,k} > 0 \\ i+1 & , u_{i+1/2,j,k} < 0 \end{cases} \tag{2.14}$$

Ω_x is calculated as

$$\Omega_{x,i+1/2,j,k} = \int_{x_{i+1/2,j,k} - u_{i+1/2,j,k}\Delta t}^{x_{i+1/2,j,k}} \Delta y \Delta z dx \tag{2.15}$$

J_y, J_z, Ω_y, and Ω_z can be similarly computed. The distribution of α in the donor cell, $\alpha_{iD}(x)$, must be considered to accurately calculate the flux of α at a cell face, *i.e.* J in Eq. (2.13). The volume averaged value of α at the cell center is available and the reconstruction of the interface has to be carried out by using this information.

2.2.2 Interface reconstruction

One-dimensional distribution of α is obtained by using a tangent hyperbolic function as proposed by Xiao *et al.* (2005):

$$\alpha_{iD}(x) = \frac{1}{2}\left\{1 + \gamma \tanh \beta_x \left(\frac{x - x_{iD-1/2}}{\Delta x} - \widetilde{x}_{iD} \right)\right\} \tag{2.16}$$

where $\gamma, \widetilde{x}_{iD}$, and β_x are parameters required to define the distribution inside the cell. γ is given by

$$\gamma = \begin{cases} 1 & , \text{if } \alpha_{iD+1} \geq \alpha_{iD-1} \\ -1 & , \text{otherwise} \end{cases} \tag{2.17}$$

The average value of distribution of α within the computational cell is equated to the discrete value of α at the cell center as follows:

$$\begin{aligned} \alpha_{iD} &= \frac{\int_{x_{iD-1/2,j,k}}^{x_{iD+1/2,j,k}} \alpha_{iD}(x)dx}{\Delta x} \\ &= \frac{\int_{x_{iD-1/2,j,k}}^{x_{iD+1/2,j,k}} \frac{1}{2}\left\{1 + \gamma \tanh \beta_x \left(\frac{x - x_{iD-1/2}}{\Delta x} - \widetilde{x}_{iD} \right)\right\}dx}{\Delta x} \\ &= \frac{1}{2}\left\{1 + \frac{\gamma}{\beta_x} \ln\left(\frac{\cosh\left[\beta_x (1 - \widetilde{x}_{iD})\right]}{\cosh\left[\beta_x \widetilde{x}_{iD}\right]} \right)\right\} \end{aligned} \tag{2.18}$$

$\widetilde{x}_{iD}$ is computed by re-arranging the above equation:

$$\widetilde{x}_{iD} = \frac{1}{2\beta_x}\left[\ln\left(\frac{e^{2\beta_x} - a_1 e^{\beta_x}}{a_1 e^{\beta_x} - 1} \right)\right] \tag{2.19}$$

where

$$a_1 = \exp\left[\frac{\beta_x\left(2\alpha_{iD}-1\right)}{\gamma}\right] \tag{2.20}$$

The parameter, β_x, controls the slope of distribution of α within the cell as shown in Fig. 2.2.

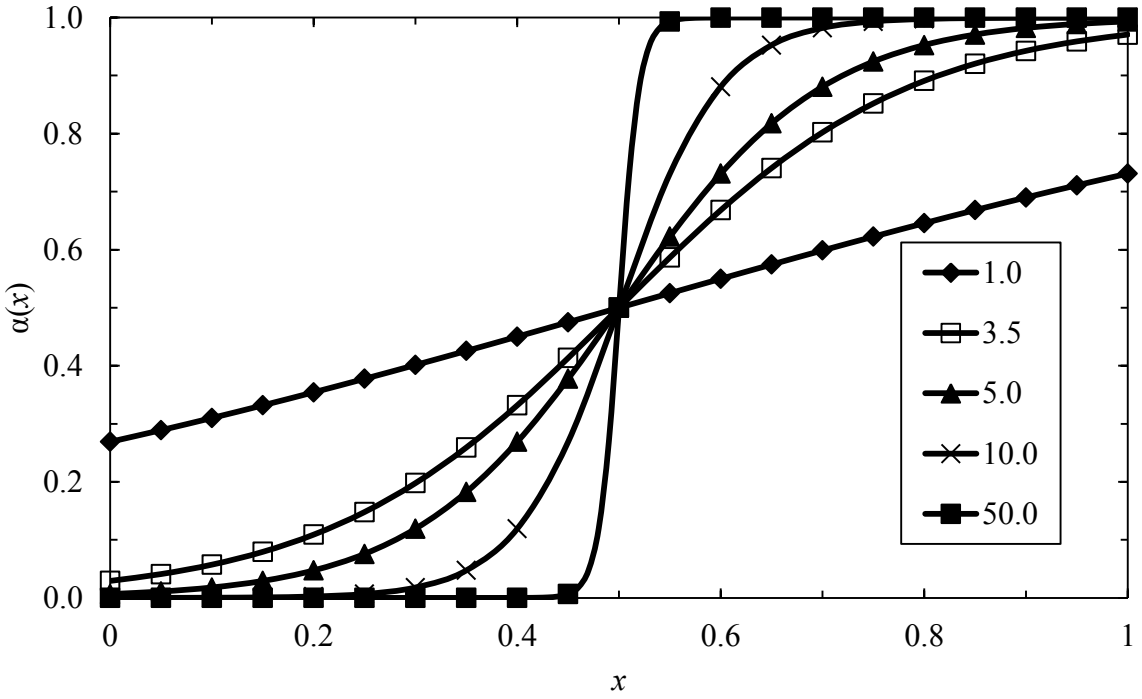

Fig. 2.2 Effect of β_x on the distribution of α

Xiao *et al.* (2005) used a constant value of β_x irrespective of orientations of the interface. It was fixed at an ad hoc value of 3.5 to ensure numerical stability, where as in this study β_x is made a function of the inclination of the interface. This would allow a more accurate reconstruction of the interface. The slope of the tangent hyperbolic function, defined by Eq. (2.16), at $\tilde{x}_{iD}$ can be computed by

$$\frac{\partial\alpha_{iD}\left(\tilde{x}_{iD}\right)}{\partial x} = \frac{1}{2}\left\{\beta_x \frac{1}{\cosh^2\left(\beta_x \cdot 0\right)}\right\} = \frac{\beta_x}{2} \tag{2.21}$$

Assuming the interface to be linear within a cell with the slope, which can be computed using the interface normal vector, and equating it to the above equation gives the following relation between β_x and the interface normal vector

$$\beta_x = \begin{cases} \dfrac{2|N_x|}{|N_y|} & ,2D \\ \dfrac{2|N_x|}{|N_y^2 + N_z^2|} & ,3D \end{cases} \tag{2.22}$$

where N_x, N_y, and N_z are the x, y, and z components of the vector normal to the interface, $\boldsymbol{N}$, respectively. $\boldsymbol{N}$ is computed by using the Arbitrary Lagrangian-Eulerian (ALE) like scheme as described by Brackbill *et al.* (1992). Equation (2.22) is for interface reconstruction in the x-direction. A more general function for β is given by

$$\beta_l = \min\left[\beta_{\max}, \max\left(\frac{2|N_l|}{\sqrt{\sum_{j\neq l} N_j^2}}, \beta_{\min}\right)\right] \qquad (l = x, y, z) \tag{2.23}$$

where the subscript l is the direction in which the interface is being reconstructed *i.e.* the direction of advection and N_l the l component of the normal to the interface. The range of β is fixed between $\beta_{\min}$ and $\beta_{\max}$. $\beta_{\min}$ is set at 0.001 and $\beta_{\max}$ at 10. These values are sufficient to represent a horizontal and a vertical interface w.r.t to the direction of advection.

Using the normalized coordinate

$$s = \frac{x - x_{i+1/2,j,k}}{\Delta x} \tag{2.24}$$

instead of x yields

$$\alpha_{iD}(s) = \frac{1}{2}\left\{1 + \gamma \tanh \beta_x \left(s + \Gamma - \tilde{x}_{iD}\right)\right\} \tag{2.25}$$

where Γ is defined by

$$\Gamma = \frac{x_{i+1/2,j,k} - x_{iD-1/2,j,k}}{\Delta x} \tag{2.26}$$

and takes the value zero or one:

$$\Gamma = \begin{cases} 1 & , u_{i+1/2,j,k} > 0 \\ 0 & , u_{i+1/2,j,k} < 0 \end{cases} \tag{2.27}$$

Substituting Eqs. (2.24) and (2.25) into Eq. (2.13) yields

$$\begin{aligned} J_{x,i+1/2,j,k} &= \int_{-C_x}^{0} \alpha_{iD}(s)\Delta x \Delta y \Delta z ds \\ &= \theta \int_{-C_x}^{0} \alpha_{iD}(s) ds \\ &= \theta \int_{-C_x}^{0} \frac{1}{2}\left\{1 + \gamma \tanh \beta_x \left(s + \Gamma - \tilde{x}_{iD}\right)\right\} ds \\ &= \frac{\theta}{2}\left\{ s + \frac{\gamma}{\beta_x} \ln\left[\cosh \beta_x \left(s + \Gamma - \tilde{x}_{iD}\right)\right]\right\}_{-c_x}^{0} \\ &= \frac{\theta}{2}\left\{ C_x - \frac{\gamma}{\beta_x} \ln\left[\frac{\cosh \beta_x \left(-C_x + \Gamma - \tilde{x}_{iD}\right)}{\cosh \beta_x \left(\Gamma - \tilde{x}_{iD}\right)}\right]\right\} \end{aligned} \tag{2.28}$$

where C_x is the Courant number in the x-direction defined by

$$C_x = \frac{u_{i+1/2,j,k}\Delta t}{\Delta x} \tag{2.29}$$

Applying the variable transformation to Eq. (2.15) yields

$$\Omega_{x,i+1/2,j,k} = \int_{-C_x}^{0} \Delta x \Delta y \Delta z ds$$

$$= \theta C_x \tag{2.30}$$

The numerical method is named THAINC and summarized in Fig. 2.3 and can be similarly applied to the y and z directions.

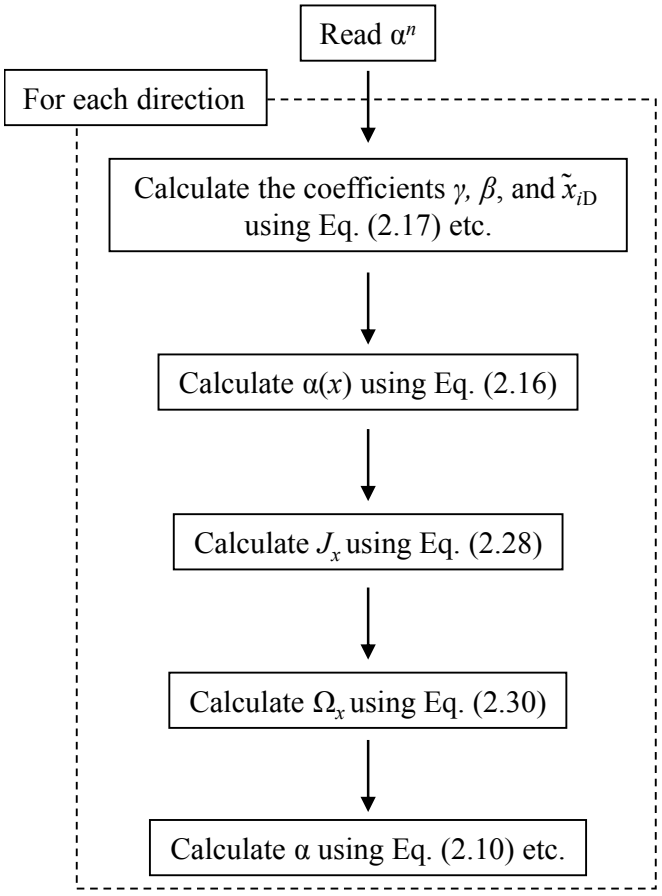

Fig. 2.3 Calculation procedure

2.2.3 Implementation of interface tracking method to two–phase flow

In this section, the method for solving the flow field is described.

2.2.3.1 Governing equation for two-phase flow

The fluid phases are assumed to be incompressible and one-fluid formulation is applied to them. Hence, the velocities of the gas and liquid phases are given by the one-fluid velocity $\boldsymbol{V} = \boldsymbol{V}_G = \boldsymbol{V}_L$. The governing equations for the motion of incompressible fluids, the continuity and momentum equations, are therefore given by

$$\nabla \cdot \boldsymbol{V} = 0 \tag{2.31}$$

$$\rho \frac{D\boldsymbol{V}}{Dt} = -\nabla P + \mu \nabla^2 \boldsymbol{V} + \rho \boldsymbol{g} + \boldsymbol{F}_{ST} \tag{2.32}$$

where ρ is the density, P the pressure, μ the viscosity, $\boldsymbol{g}$ the acceleration due to gravity, and $\boldsymbol{F}_{ST}$ the surface tension force acting on the gas-liquid interface. The surface tension force is calculated based on the continuum surface force (CSF) model proposed by Brackbill *et al*. (1992):

$$\boldsymbol{F}_{ST} = \sigma \kappa \boldsymbol{n} \delta \tag{2.33}$$

where σ is the surface tension between the gas and liquid phases, κ the mean curvature of the interface, $\boldsymbol{n}$ the unit normal to the interface, and δ the delta function. Equation (2.33) can be written as

$$\boldsymbol{F}_{ST} = \sigma \kappa \boldsymbol{N} \tag{2.34}$$

where

$$\boldsymbol{N} = \nabla \alpha \tag{2.35}$$

The curvature is given by

$$\kappa = -\nabla \cdot \boldsymbol{n} \tag{2.36}$$

The density and viscosity are given by

$$\rho = \alpha_L \rho_L + \alpha_G \rho_G \tag{2.37}$$

$$\mu = \alpha_L \mu_L + \alpha_G \mu_G \tag{2.38}$$

The velocity and pressure fields are obtained by solving Eqs. (2.31) and (2.32) using the SMAC (simplified marker and cell) method (Amsden and Harlow, 1965).

2.3 Advection tests

Several advection tests as will be discussed in the following sections were carried out to check the accuracy of the proposed method. Its performance was compared to some of the existing numerical schemes for estimating the distribution of α.

2.3.1 Advection in one-dimension

The effect of an adaptive β, THAINC, as compared to a constant one, THINC, on the accuracy of advection was investigated. The first test was a one-dimensional wave being advected at a velocity of 1 m/s. The mesh size was 1 mm. As shown in Fig. 2.4, the wave was initialized as

$$\alpha = \begin{cases} 1 & , \text{for } (10 \le i \le 19) \\ 0 & , \text{otherwise} \end{cases} \tag{2.39}$$

The Courant number was set at 0.5. The wave was advected for 100 time steps and the results obtained with THINC and THAINC are shown in Fig. 2.4.

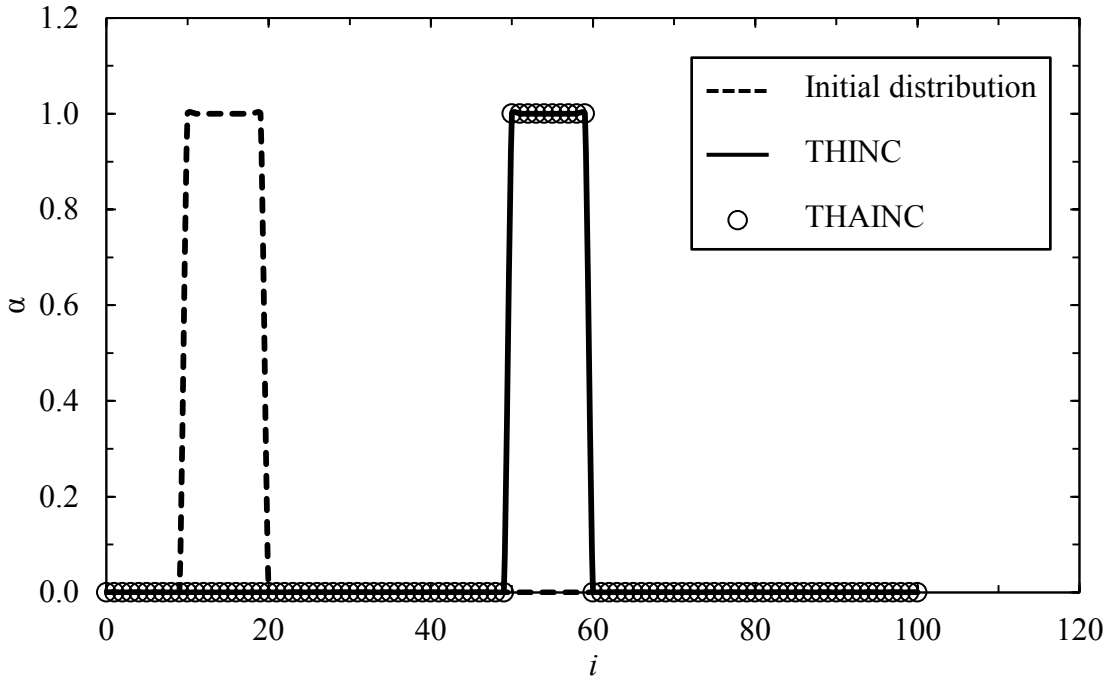

Fig. 2.4 α distribution of one-dimensional wave after advection over 100 time steps

The results for THINC and THAINC were found to be exactly the same with no undershooting (α<1) or overshooting (α>1) since a one-dimensional wave can be accurately represented by a constant value of β.

Next, the advection of a fluid square in the x-direction with a velocity of 1 m/s was carried out. A 200×200 mesh was used with the mesh size set at 1 mm. The fluid square was initialized as

$$\alpha = \begin{cases} 1 & \text{, for } (5 \le i \le 24) \text{ and } (6 \le i \le 24) \\ 0.5 & \text{, for } (5 \le i \le 24) \text{ and } (j = 5,25) \\ 0 & \text{, otherwise} \end{cases} \tag{2.40}$$

as shown in Fig. 2.5(a). The fluid square is shown using contours for α with values between 0 and 1 at an interval of 0.05. The Courant number was set at 0.1 and the fluid square was transported over a distance of 5 times its length. THINC was found to have artificial wrinkling at horizontal sides, *i.e.* the top and the bottom edges, as compared to vertical sides, *i.e.* the left and the right edges as shown in Fig. 2.5(b). The reason for this is the use of a constant value of β. β with a value of 3.5 is able to represent an interface which is perpendicular to the direction of the advection. But an interface which is more horizontally aligned in the direction of advection needs to have a more horizontal one dimensional reconstruction, *i.e.* lower value of β (Fig. 2.5). This could be the cause of artificial wrinkling of the interface only at the horizontal sides which were being reconstructed inappropriately. This problem was reasonably eliminated as shown in Fig. 2.5(c) by adjusting the value of β, according to Eq. (2.23), to ensure a more horizontal interface for the top and bottom edges.

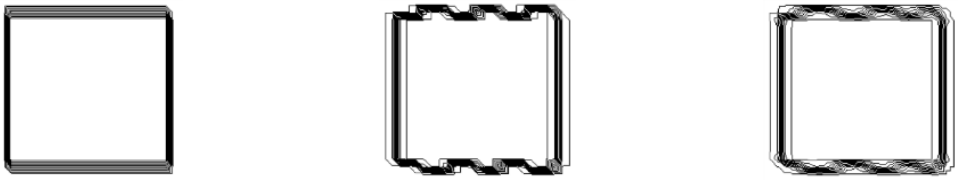

(a) Initial (b) THINC (c) THAINC

Fig. 2.5 Shape of the fluid square after transport in *x*-direction

2.3.2 Advection in multi-dimensions

Finally, advection tests in multi-dimensions were carried out and the results obtained from THAINC were compared with some of the existing numerical schemes. The first test, Test A, was that of a fluid circle rotating about the centre of the grid as shown in Fig. 2.6. The diameter of the circle was set at $20\Delta x$ with $\Delta x = 1$ mm. The circle was advected for 5 revolutions with an angular velocity of 1 rad/s. The Courant number for two-dimensional flow, C_O, is defined by

$$C_O = \frac{u_{i+1/2,j}\Delta t}{\Delta x} + \frac{v_{i,j+1/2}\Delta t}{\Delta y} \tag{2.41}$$

where u and v are the x and y components of the velocity, respectively.

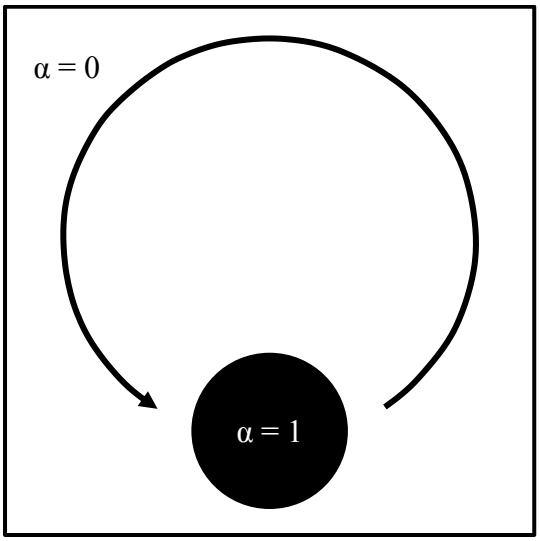

Fig. 2.6 Advection test of rotating fluid circle, Test A

The schemes selected for comparison were the 1st order upwind; donor-acceptor (DA) (Hirt & Nichols, 1981); tangent of hyperbola for interface reconstruction/weighted linear interface calculation (THINC/WLIC) (Yokoi, 2007) and THINC. The difference in the schemes is in the reconstruction of the interface and is explained for advection in the x-direction with the help of Fig. 2.7. $\alpha_{iD}(x)$ in calculation of J using Eq. (2.13) is fixed at a constant value equal to the cell centre value of the donor cell in the 1st order upwind. This effectively results in a horizontal interface reconstruction advection w.r.t the direction of transport, as can be seen in Fig. 2.7(b), irrespective of the actual inclination of the interface and causes numerical diffusion of the initially sharp interface as shown in Fig. 2.8(b). DA calculates J by assuming either a vertical or a horizontal interface w.r.t the direction of advection depending on the orientation of the interface. The interface reconstruction in THINC is close to vertical w.r.t the direction of advection as can be seen in Fig. 2.2. Fig. 2.8(c) and (d) show that both DA and THINC cause large shape distortion and this is due to

inaccurate interface reconstruction. J in THINC/WLIC is calculated by taking a weighted average of the flux calculated with THINC, *i.e.* based on vertical interface, and 1st order upwind, *i.e.* based on horizontal interface, by

$$J_{\text{THINC/WLIC}} = \omega J_{\text{THINC}} + (1-\omega) J_{\text{1st order upwind}} \tag{2.42}$$

where ω is the weight calculated using the components of the normal vector by

$$\omega = \frac{|N_x|}{|N_x| + |N_y|} \tag{2.43}$$

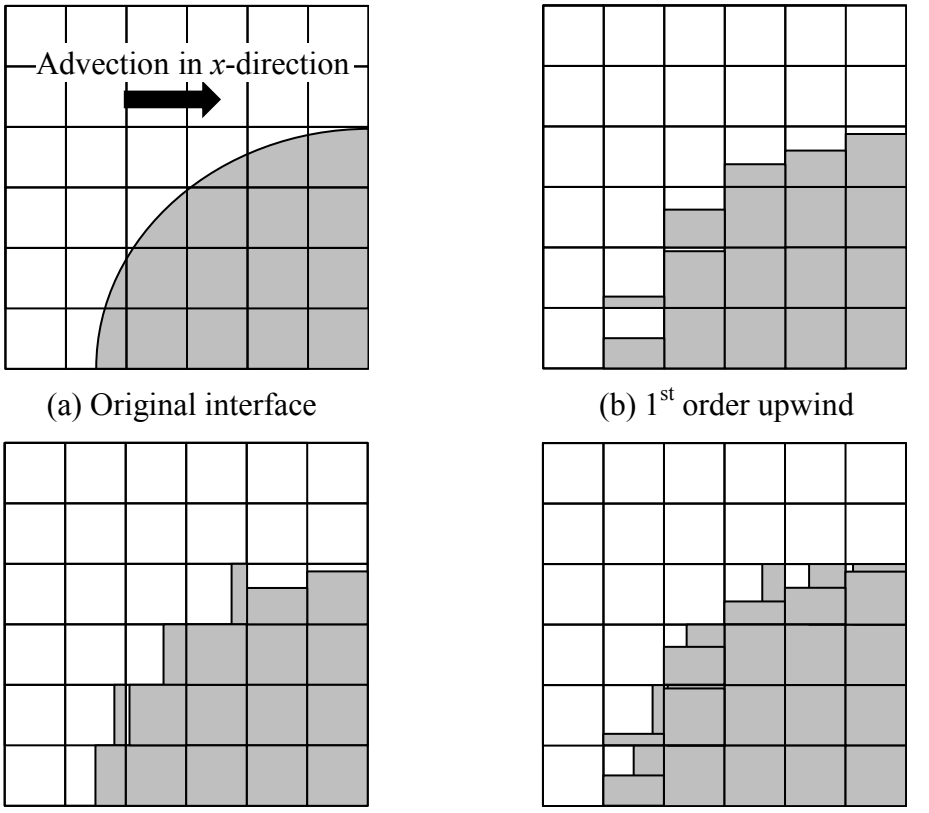

(a) Original interface (b) 1st order upwind

(c) DA (Hirt and Nichols, 1981) (d) THINC/WLIC (Yokoi, 2007)

Fig. 2.7 Illustration of interface reconstruction in different schemes

Hence, even though THINC/WLIC does not attempt to reconstruct the interface directly, the calculation of J incorporates the inclination of the interface which leads to a much

improved shape preservation as compared with THINC as can be seen in Fig. 2.8(e). The interface reconstruction based on the interface inclination as is done in THAINC gives a more accurate calculation of J, leading to the best shape preservation as shown in Fig. 2.8(f).

A quantitative comparison was carried out by comparing the error in the predicted shape evaluated over the whole domain at the end of the simulation by

$$E_{\mathrm{S}} = \frac{\sum_{i,j,k} \left| \alpha_{i,j,k} - \alpha_{i,j,k,C} \right|}{\sum_{i,j,k} \alpha_{i,j,k,C}} \tag{2.44}$$

and the error in total volume conservation in the computational domain evaluated by

$$E_{\mathrm{V}} = \frac{\left| \sum_{i,j,k} \alpha_{i,j,k} - \sum_{i,j,k} \alpha_{i,j,k,C} \right|}{\sum_{i,j,k} \alpha_{i,j,k,C}} \tag{2.45}$$

where the subscript C denotes the correct value. The results of E_{S} and E_{V} for $C_O = 0.125$ are shown in Table 2.1. The comparison shows that THAINC yields the best results in terms of conservation of shape and volume.

Table 2.1 Comparison of E_{V} and E_{S} for different schemes (Test A)

Numerical scheme	E_{V} [%]	E_{S} [%]
1st order upwind	3.4×10^{-2}	69.1
DA (Hirt & Nichols, 1981)	1.7×10^{-2}	25.3
THINC (Xiao *et. al*, 2005)	1.0×10^{-11}	14.9
THINC/WLIC (Yokoi, 2007)	4.5×10^{-11}	2.5
THAINC (Present)	2.1×10^{-11}	1.9

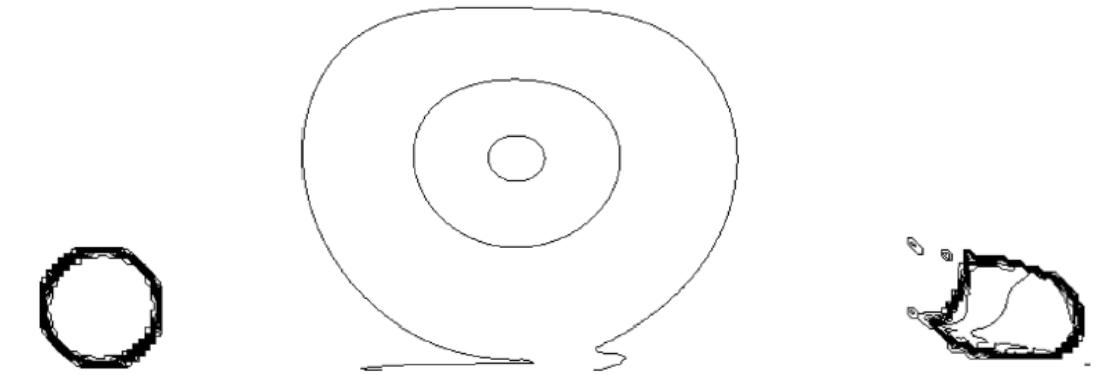

(a) Initial (b) 1st order upwind (c) DA

(d) THINC (e) THINC/WLIC (f) THAINC

Fig. 2.8 Comparison of shapes obtained after rotating the circle by five revolutions

Apart from THAINC, THINC/WLIC also gave reasonably good results and hence a more detailed comparison only with THINC/WLIC was carried out. Diagonal advection shown in Fig. 2.9 was carried out for a fluid square in two-dimensions (Test B) and a fluid cube in three-dimensions (Test C). The length of the square and cube was kept same at $20\Delta x$ with Δx = 1 mm. The components of the velocity were set at 1 m/s.

Since E_V in both THAINC and THINC/WLIC were negligibly small, only the effect of C_O on E_S, which represents the amount of shape distortion, was investigated for C_O = 0.125, 0.25, and 0.5. The results are shown in Fig. 2.10.

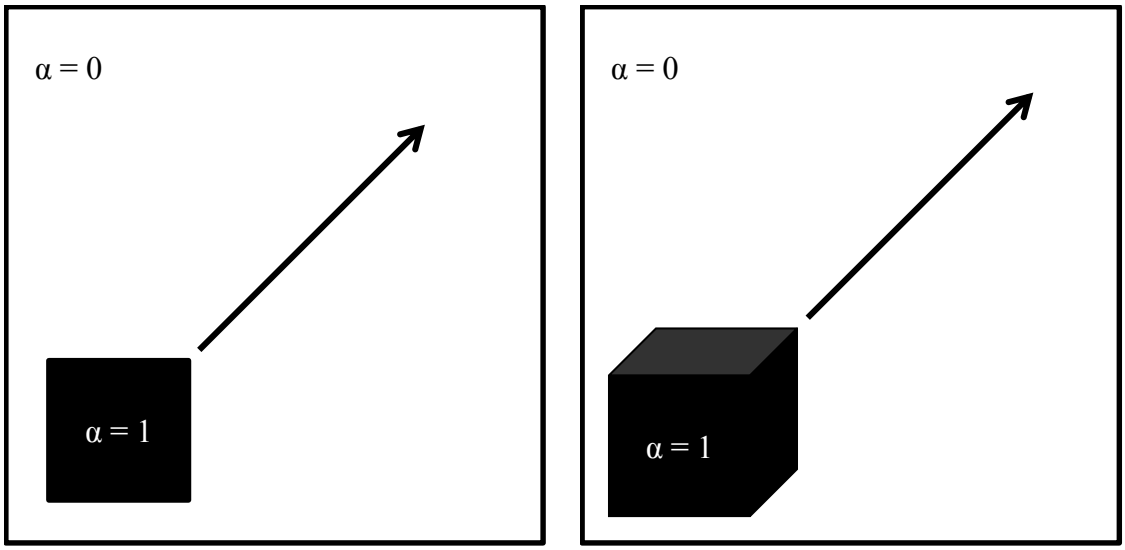

(a) Test B (b) Test C

Fig. 2.9 Diagonal advection tests

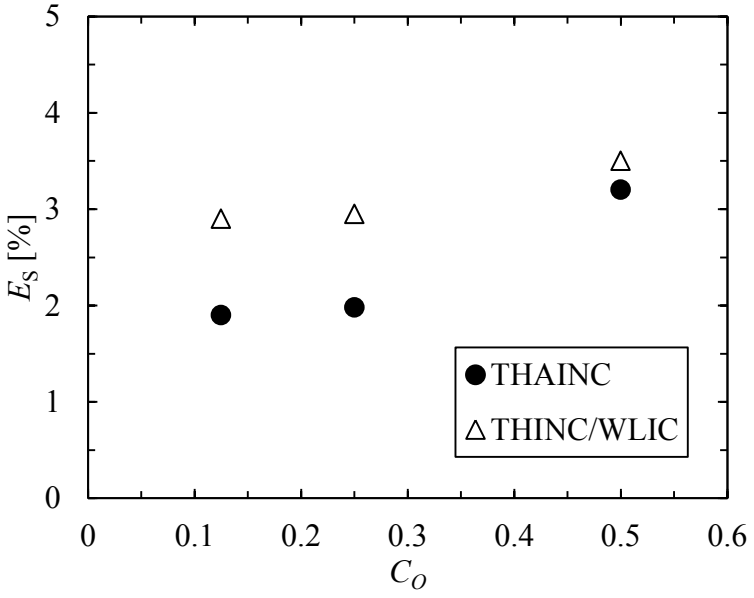

(a) Test A

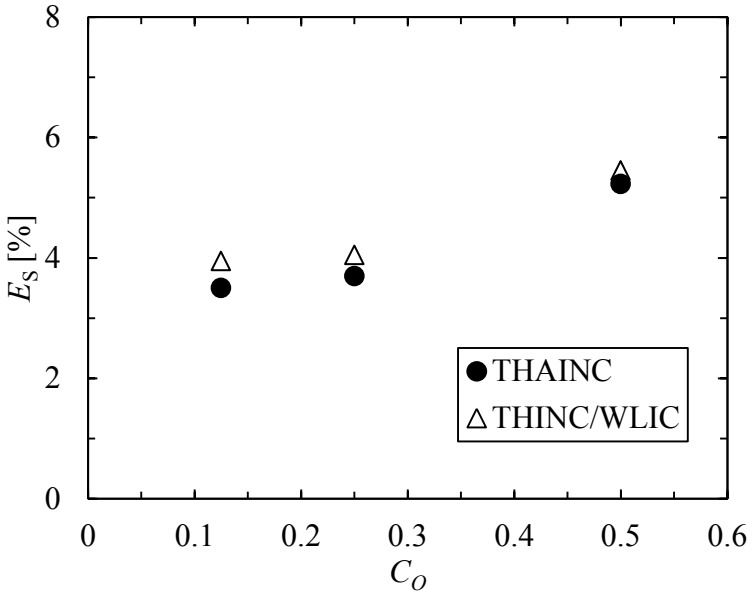

(b) Test B

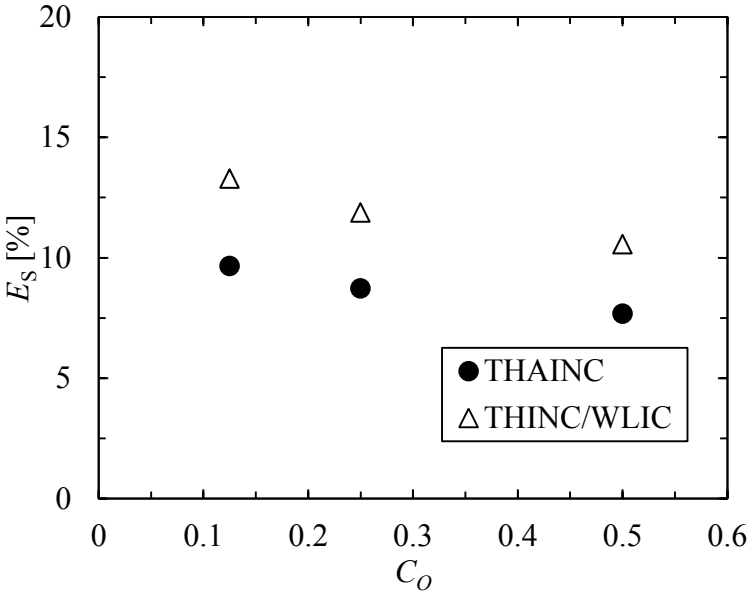

(c) Test C

Fig. 2.10 Comparison of E_S between THINC/WLIC and THAINC

The proposed method had lower errors as compared to THINC/WLIC for all the tests. The difference in the errors was found to be prominent in the case of three-dimensional advection test, Test C. THAINC was also able to preserve the interface sharpness better

than THINC/WLIC as can be seen from Fig. 2.11. The shapes are shown using contours of α with values between 0 and 1 at an interval of 0.05

(a) THINC/WLIC (b) THAINC

Fig. 2.11 Comparison of final shape in Test C (C_O = 0.25)

2.4 Simulation of a rising bubble

Two dimensional simulation of a rising air bubble of diameter 2 cm in stagnant water was carried out. A calculation domain of size 30 cm×10 cm was used as shown in Fig. 2.12. The physical properties of water and air at 25 °C and 1 atm were used, *i.e.* ρ_L = 1000 kg/m^3, ρ_G = 1.25 kg/m^3, $\mu_L = 1\times10^{-3}$ Pa·s, $\mu_G = 1.82\times10^{-5}$ Pa·s and σ = 0.072 N/m. The mesh size was set at $\Delta x = \Delta y$ = 1 mm and the time step was 10^{-4} s. Tracer was used to visualize the development of the wake under the bubble. The tracer was imitated by using a dimensionless scalar *C* which was set at 1 in the desired location of the tracer as shown in Fig. 2.13(a). The scalar *C* was transported by solving

$$\frac{\partial C}{\partial t} + \nabla\cdot(C\boldsymbol{V}) = 0 \tag{2.46}$$

The motion of the rising bubble was simulated. The results are shown in Fig. 2.13.

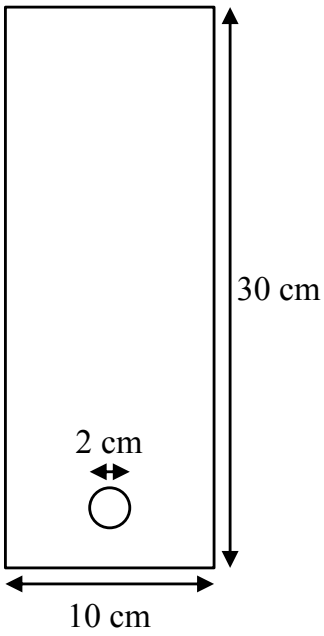

Fig. 2.12 Schematic of the computational domain

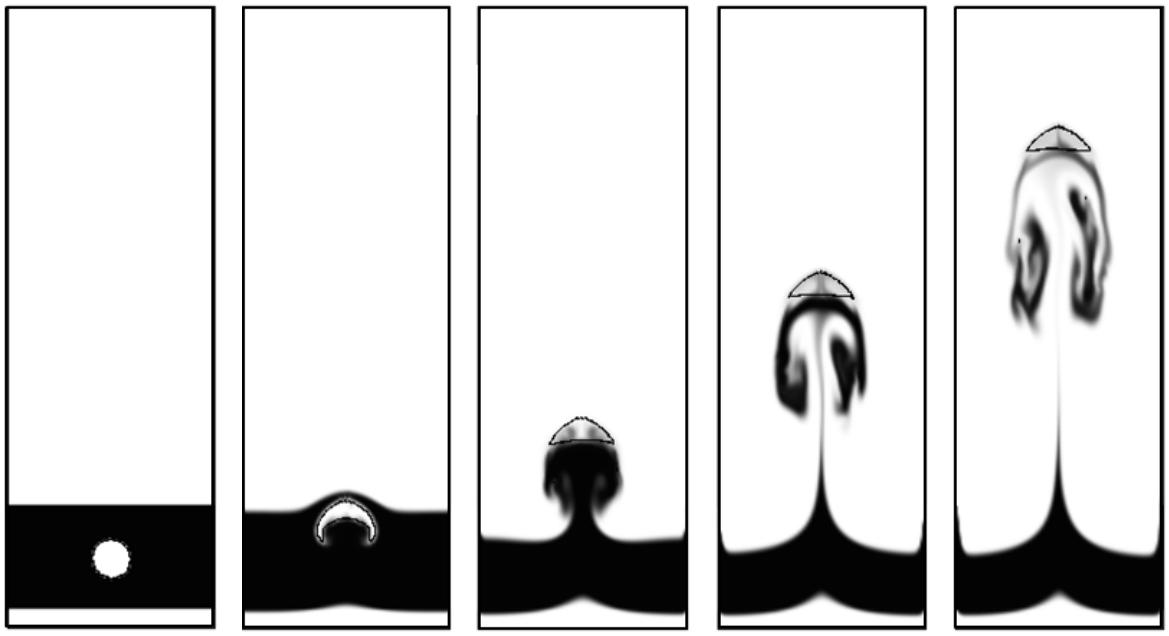

(a) 0 s (b) 0.10 s (c) 0.25 s (d) 0.50 s (e) 0.75 s

Fig. 2.13 Motion of single bubble in stagnant water

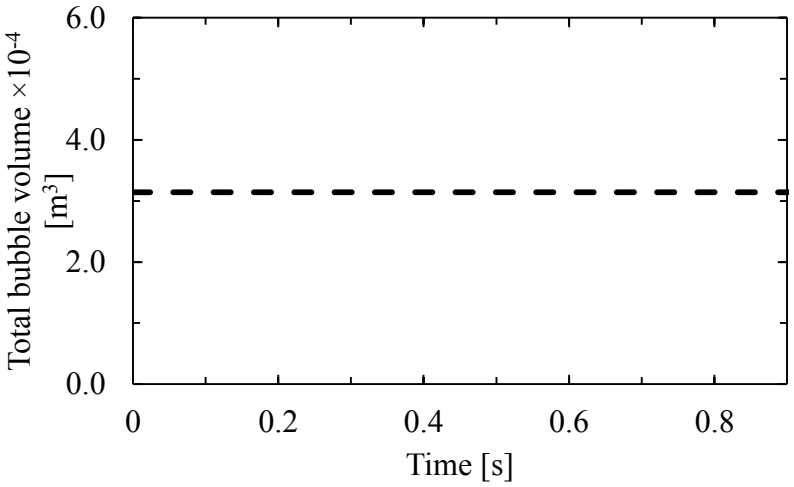

(a) Transient behaviour of the total bubble volume

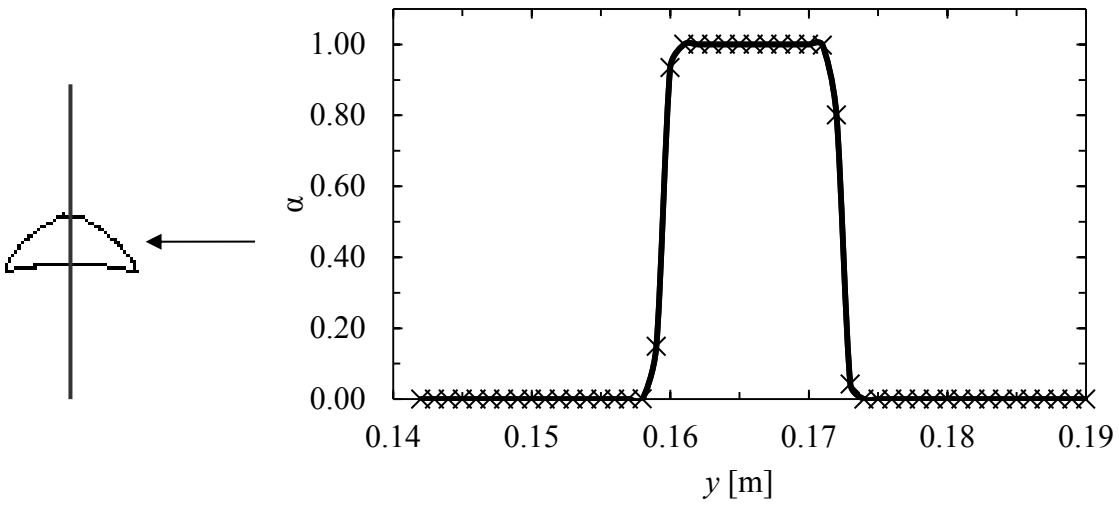

(b) Distribution of α at vertical section passing through the center of the bubble

Fig. 2.14 Simulation of rising single bubble

The terminal velocity, V_T, of a two-dimensional air bubble is given by

$$V_T = \lambda\sqrt{gd} \tag{2.47}$$

where g is the magnitude of $\boldsymbol{g}$ and d the diameter of the bubble. The value of λ has been investigated in various studies (Collins, 2005; Grace and Harrison, 1967; Maneri and

Mendelson, 1968) and is reported to be between 0.59 and 0.632. The value of V_T is calculated to be between 0.26−0.28 m/s by applying the reported values of λ to Eq. (2.45). The value of V_T calculated from the simulation was 0.275 m/s and is in the estimated range. The effect of implementation of two-phase flow algorithm on the volume conservation was also checked by the total volume of the bubble as shown in Fig. 2.14(a). E_V was 0.57% which is higher than the values reported in the advection tests but still significantly low for practical applications. The increase in E_V can be attributed to the error in the divergence of velocity. It was zero in the case of the advection tests but depends on the convergence criterion in the solution of the Poisson's equation used for the pressure. A stricter convergence criterion will lower the value E_V but will also cause an increase in the computational cost. The α distribution, 0.5 s after the bubble begins to rise, along a vertical cross-section passing through the center of gravity of the bubble is shown in Fig. 2.14(b). The ability of THAINC to capture the interface within two cells with no over or undershooting can also be confirmed. The same method can also be applied to simulate drops by making the liquid as the dispersed phase.

2.5 Wetting of a solid plate by a drop

Simulation of motion of a drop on a solid plate was carried out. This phenomenon is governed by the dynamic contact angle. Several empirical models for the dynamic contact angle (Tanner, 1973; Jiang *et al.*, 1979; Kistler, 1993) have been proposed. They are based on the equilibrium contact angle and the Capillary number, *Ca*,

$$Ca = \frac{\mu U_{CL}}{\sigma} \tag{2.48}$$

where U_{CL} is the velocity of contact line. The dynamic contact angle model employed in this study is the one proposed by Yokoi *et al*. (2009), which is a combination of Tanner's law (Tanner, 1973) and constant angles for wetting and dewetting phases, *i.e.*

$$\Phi_D = \begin{cases} \min\left[\Phi_E + \left(\frac{Ca}{l_a}\right)^{1/3}, \Phi_{mda}\right] & \text{, for wetting phase} \\ \max\left[\Phi_E + \left(\frac{Ca}{l_r}\right)^{1/3}, \Phi_{mdr}\right] & \text{, otherwise} \end{cases} \tag{2.49}$$

where Φ_D is the dynamic contact angle, Φ_E the equilibrium contact angle, and Φ_{mda}, Φ_{mdr}, l_a, and l_r are the model parameters.

A falling drop experiment conducted by Yokoi *et al*. (2009) was simulated for validation. A clean water drop of R = 1.14 mm was used with an impact velocity of 1 m/s. The physical properties of water and air at 25 °C and 1 atm were used. The two-dimensional axisymmetric coordinates were used and the mesh was 250×200. The cell size was uniform, $\Delta = 3.8\times10^{-5}$ m, and the time step was 5×10^{-7} s. Φ_E was set at 90° and the model parameters Φ_{mda}, Φ_{mdr}, l_a, and l_r, were 114°, 52°, 9×10^{-9}, and 9×10^{-8}, respectively (Yokoi *et al*., 2009). A comparison of the predicted drop shape with the experiment is shown in Fig. 2.15. Transient behaviour of the wetting length defined as the length, which is in contact with the surface, was plotted in Fig. 2.16. The predicted height of the drop as a function of time is also shown in Fig. 2.17. The present result is in good agreement with the experiment.

The volume conservation was also checked for the total volume of the drop as shown in Fig. 2.18(a). E_V remained of the same order as in the case of the simulation in Cartesian coordinates. The distribution at a vertical cross-section normal to the tip of the drop at 10 ms is shown in Fig. 2.18(b). Here also the ability of THAINC to capture the interface within two cells with no over or undershooting can be confirmed.

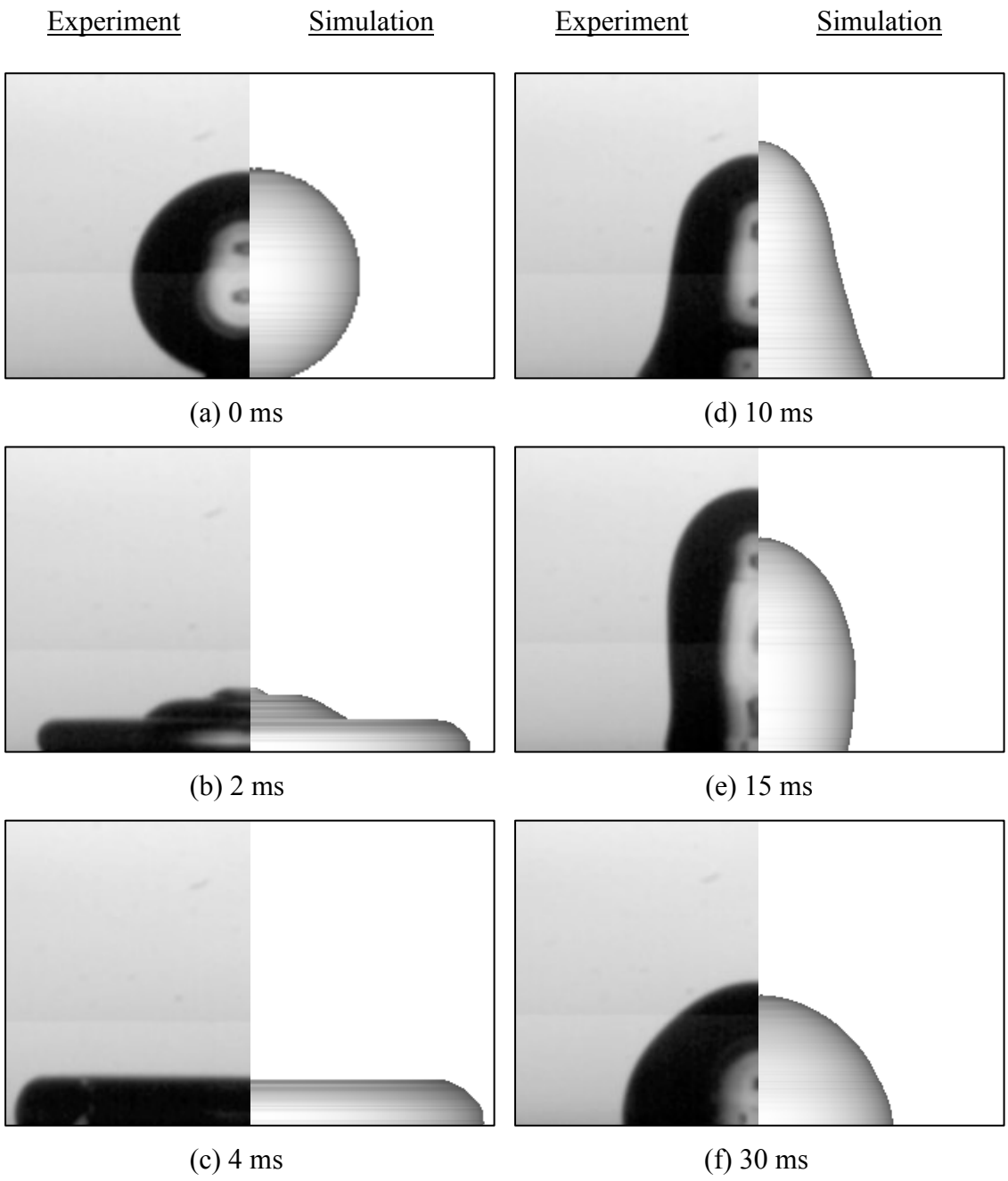

Fig. 2.15 Comparison between predicted and measured drop motion (Yokoi *et al.*, 2009)

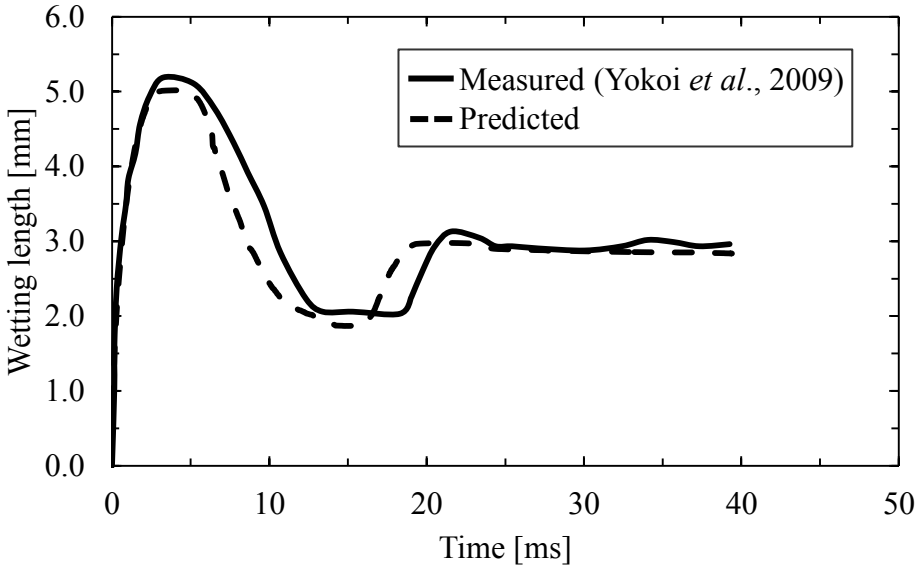

Fig. 2.16 Drop wetting length

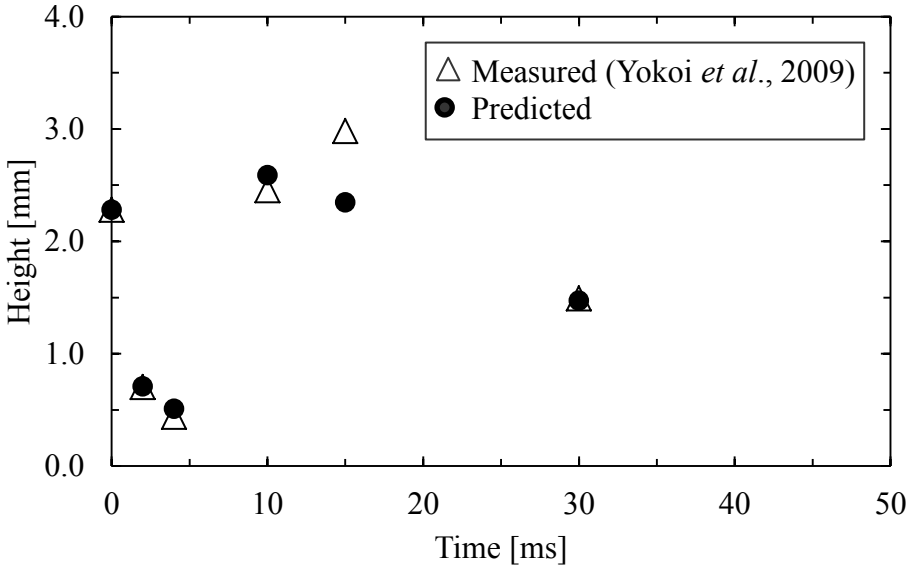

Fig. 2.17 Drop height

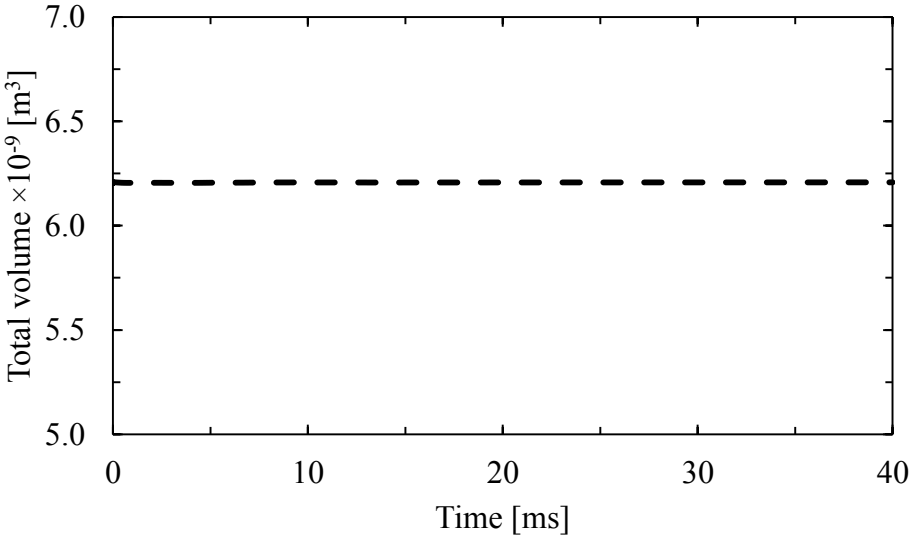

(a) Transient behaviour of the total volume

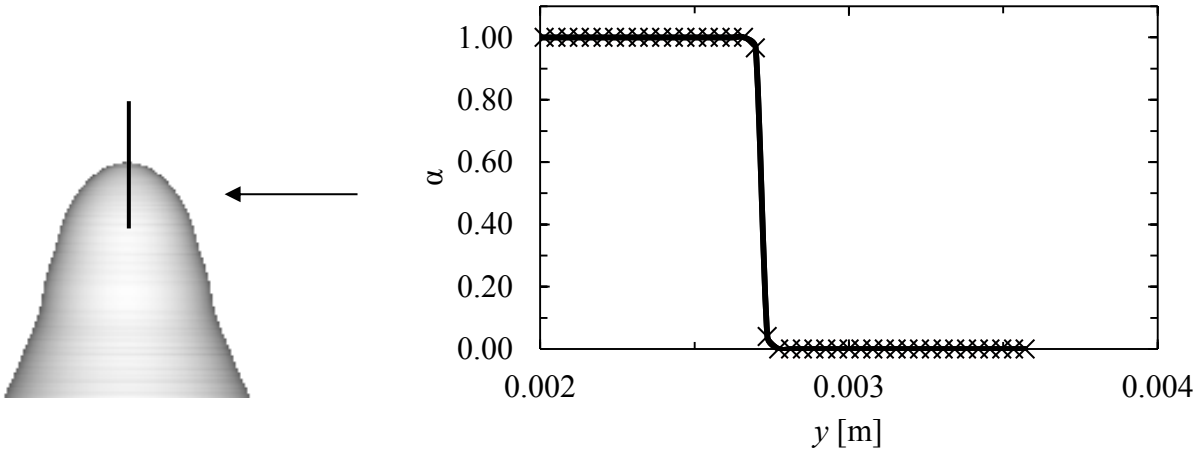

(b) Distribution of α at vertical section normal to the tip of the drop at 10 ms

Fig. 2.18 Simulation of drop motion on a solid plate

2.6 Conclusions

The ability of tangent hyperbolic function to effectively represent the interface was confirmed. The problem of artificial wrinkling of interface in multi-dimensional simulations caused by the use of constant β (Xiao *et al.*, 2005) was overcome with the proposed method by making β a function of the inclination of the interface without increasing the computational cost. The method is easy to program and extend to three dimensions. The accuracy of the proposed method was investigated by carrying out three types of advection tests and simulation of a rising bubble and wetting of a solid plate by a drop. The following results were obtained:

(1) The proposed method has lower errors, E_V and E_S, in the advection tests as compared to THINC, THINC/WLIC, Donor-Acceptor, and 1st order upwind schemes.

(2) The predicted motion of the gas-liquid interface in the case of rising bubble and drop on a solid plate was in good agreement with the reported behaviour.

(3) THAINC is able to capture the gas-liquid interface within two cells with good volume conservation. There is also no overshooting or undershooting of the phase indicator function.

References

Amsden, A. A., Harlow, F. H., The SMAC method: A numerical technique for calculating incompressible fluid flows, Technical Report LA-4370, Los Alamos Scientific Laboratory, Los Alamos, U.S.A., 1970.

Brackbill, J., Kothe, D., Zemach, C., A continuum method for modeling surface tension, *Journal of Computational Physics*, 1992, 100, pp. 335–354.

Collins, R., A simple model of the plane gas bubble in a finite liquid, *Journal of Fluid Mechanics*, 1965, 22, 4, pp. 763-771.

Grace, J. R., Harrison, D., The influence of bubble shape on the rising velocities of large bubbles, 1967, *Chemical Engineering Science*, 22, pp. 1337-1347.

Hirt, C. W., Nichols, B. D., Volume of fluid (VOF) method for the dynamics of free boundaries, *Journal of Computational Physics*, 1981, 39, pp. 201-225.

Jiang, T., Oh, S., Slattery , J. C., Correlation for dynamic contact angle, *Journal of Colloid and Interface Science*, 1979, 69, pp. 74-77.

Kistler, S. F., Hydrodynamics of wetting, *Wettability*, 1993, pp. 311-429.

Kunugi, T., Direct numerical algorithm for multiphase flow with free surfaces and interfaces, *Nihon Kiki Gakkai Ronbunshu*, 1997, 63, 609, pp. 1576 – 1584.

Maneri, C. C., Mendelson, H. D., The rise velocity of bubbles in tubes and rectangular channels as predicted by wave theory, *AIChE Journal*, 1968, 14, pp. 295-300.

Rider, W. J., Kothe, D. B., Reconstructing volume tracking, *Journal of Computational Physics*, 1998, 141, pp. 112–152.

Takewaki, H., T.,Yabe, The Cubic-Interpolated Pseudo Particle (CIP) Method: Application to Nonlinear and Multi-Dimensional Hyperbolic Equations, , *Journal of Computational Physics*, 1987, 70, pp. 355-372.

Tanner, L., The spreading of silicon oil drops on horizontal surfaces, *Journal of Physics*, 1973, 23, pp. 1473-1484.

Xiao, F., Honma, Y., Kono, T., A simple algebraic interface capturing scheme using hyperbolic tangent function, *International Journal for Numerical Methods in Fluids*, 2005, 48, pp. 1023–1040.

Yokoi, K., Efficient implementation of THINC scheme: A simple and practical smoothed VOF algorithm, *Journal of Computational Physics*, 2007, 226, pp. 1985–2002.

Yokoi, K, Vadillo , D., Hinch J., Hutchings, I., Numerical studies of the influence of the dynamic contact angle on a droplet impacting on a dry surface, *Physics of Fluids*, 2009, 21, 072102, pp.1-12.

Chapter 3

Extension of the interface tracking method to flows containing complex solid obstacles

3.1 Introduction

Coating processes often contain complex solid geometries such as the nozzle of the inkjet head which affect their overall behaviour. Hence, the numerical method must be equipped to handle the presence of complex solid geometries. This requires special treatment and several techniques (Peskin, 1977; Koshizuka *et al.*, 1990; Landsberg, 1997) have been proposed for this. Among them, the immersed boundary (IB) method has been identified as a suitable method. The immersed boundary method deals with the shape of a solid body in an orthogonal structured grid. The use of such a grid facilitates easy programming as well as good numerical stability. The program is also easy to parallelize. Fadlun *et al*. (2000) developed a second-order accurate and highly efficient method. The efficiency and easiness of their method has made it very popular in this field (e.g. Paravento *et al.*, 2008; Noor *et al*., 2009).

In this chapter, an immersed boundary method is implemented on THAINC to perform simulation of multiphase flows in complex geometries or flows including solid objects of arbitrary shapes. The proposed method is referred to as THAINC-IB. The fluid-volume and

momentum fluxes through computational cell faces are calculated by taking the effect of the solid into account. The potential of THAINC-IB will be demonstrated using three examples: (1) advection of a square, (2) flow about cylindrical tubes in a staggered arrangement, and (3) a dam break problem with an obstacle.

3.2 Numerical method for interface tracking in the presence of solid

3.2.1 Transport equation of gas-liquid interface

An equation for tracking gas-liquid interface in the presence of solid is derived in the following. Figure 3.1 shows a system consisting of a solid phase and two fluid phases. The solid phase is shown by the area shaded with hatched lines while the fluids are shown by the empty regions in the diagram. The fluids are separated from each other by an interface. The following assumptions are made in the present model: one solid phase and two fluid phases can be simultaneously present in a computational cell, the phases are immiscible, there is no phase change and the solid phase is stationary. The volume of a computational cell is therefore given by

$$\theta = \theta_G + \theta_L + \theta_S \tag{3.1}$$

where the subscript S denotes the solid phase. The volume fractions of the phases satisfy

$$\alpha_G + \alpha_L + \alpha_S = 1 \tag{3.2}$$

Since the solid phase is assumed to be stationary, α_S follows

$$\frac{\partial \alpha_S}{\partial t} = 0 \tag{3.3}$$

The gas and liquid volume fractions, η_K, in the fluid volumes are defined by

$$\eta_K = \frac{\alpha_K}{\alpha_F} \qquad (K = \mathrm{G, L}) \tag{3.4}$$

where

$$\alpha_F = \alpha_G + \alpha_L \tag{3.5}$$

The η_G and η_L satisfy

$$\eta_G + \eta_L = 1 \tag{3.6}$$

Substituting Eq. (3.4) into Eq. (2.4) yields

$$\frac{\partial \eta_K}{\partial t} + \nabla \cdot (\eta_K \boldsymbol{V}) = \eta_K \nabla \cdot \boldsymbol{V} \tag{3.7}$$

Taking the volume average over the fluid region for Eq. (3.7) and using the volume averaged value of η_K inside the computational cell gives

$$\frac{\partial \eta_K}{\partial t} + \frac{1}{\theta_F} \int_{\theta_F} \nabla \cdot (\eta_K \boldsymbol{V}) d\theta = \frac{\eta_K}{\theta_F} \int_{\theta_F} \nabla \cdot \boldsymbol{V} d\theta \tag{3.8}$$

where $\theta_F = \theta_G + \theta_L$. Applying the divergence theorem, Eq. (2.8), to Eq. (3.8) yields

$$\frac{\partial \eta_K}{\partial t} + \frac{1}{\theta_F} \int_{\boldsymbol{S}_F} (\eta_K \boldsymbol{V}) \cdot d\boldsymbol{S} = \frac{\eta_K}{\theta_F} \int_{\boldsymbol{S}_F} \boldsymbol{V} \cdot d\boldsymbol{S} \tag{3.9}$$

The gas–liquid interface in the presence of solid phase is tracked by solving Eq. (3.9). For the sake of simplicity, η_K will be referred to as η from hereon.

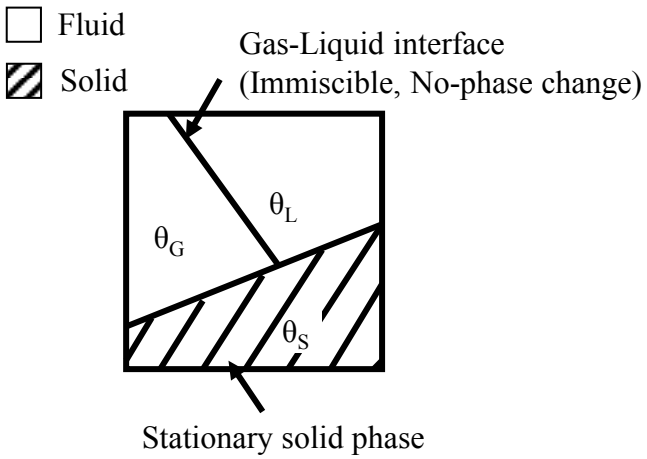

Fig. 3.1 Phase field in the present model

The following direction split is used to transport η:

$$\eta^{*} = \eta^{n} - \left(\frac{J^{n}_{x,i+1/2,j,k} - J^{n}_{x,i-1/2,j,k}}{\theta_F} \right) + \eta^{n} \left(\frac{\Omega^{n}_{x,i+1/2,j,k} - \Omega^{n}_{x,i-1/2,j,k}}{\theta_F} \right) \tag{3.10}$$

$$\eta^{**} = \eta^{*} - \left(\frac{J^{*}_{y,i,j+1/2,k} - J^{*}_{y,i,j-1/2,k}}{\theta_F} \right) + \eta^{*} \left(\frac{\Omega^{*}_{y,i,j+1/2,k} - \Omega^{*}_{y,i,j-1/2,k}}{\theta_F} \right) \tag{3.11}$$

$$\eta^{n+1} = \eta^{**} - \left(\frac{J^{**}_{z,i,j,k+1/2} - J^{**}_{z,i,j,k-1/2}}{\theta_F} \right) + \eta^{**} \left(\frac{\Omega^{**}_{z,i,j,k+1/2} - \Omega^{**}_{z,i,j,k-1/2}}{\theta_F} \right) \tag{3.12}$$

The calculation of J and Ω in THAINC-IB is given in detail in the following section.

3.2.2 Solution algorithm based on THAINC-IB

The calculation of J_x is modified to incorporate the presence of solid inside the cell by using the new phase indicator, η, and introducing area fraction of the fluid phase, $A_F(x)$, in Eq. (2.13) as

$$J_{x,i+1/2,j,k} = \int_{x_{i+1/2,j,k}-u_{i+1/2,j,k}\Delta t}^{x_{i+1/2,j,k}} \eta_{iD}(x) A_{\mathrm{F},iD}(x) \Delta y \Delta z dx \tag{3.13}$$

The distribution of η in the *x*-direction is obtained by using the same tangent hyperbolic function as in THAINC; *i.e.* η is approximated by the following function:

$$\eta_{iD}(x) = \frac{1}{2}\left\{1 + \gamma \tanh \beta_x \left(\frac{x - x_{iD-1/2}}{\Delta x} - \tilde{x}_{iD} \right)\right\} \tag{3.14}$$

The equations for calculating γ, $\tilde{x}_{iD}$ and β_x are the same but η is used instead of α. $A_{\mathrm{F},iD}(x)$ is approximated as

$$A_{\mathrm{F},iD}(x) = A_{\mathrm{F},i+1/2,j,k} + a\left(\frac{x - x_{i+1/2,j,k}}{\Delta x} \right) \tag{3.15}$$

where

$$a = A_{\mathrm{F},iD+1/2,j,k} - A_{\mathrm{F},iD-1/2,j,k} \tag{3.16}$$

Details of the procedure to calculate A_{F} at a cell face are given in Section 3.2.4. Using the normalized coordinate, *s*, defined by Eq. (2.24) instead of *x* yields

$$\eta_{iD}(s) = \frac{1}{2}\left\{1 + \gamma \tanh \beta_x \left(s + \Gamma - \tilde{x}_{iD} \right)\right\} \tag{3.17}$$

Equation (3.15) then reduces to

$$A_{\mathrm{F},iD}(s) = A_{\mathrm{F},i+1/2,j,k} + as \tag{3.18}$$

Equation (3.13) can be written as a function of *s* as

$$J_{x,i+1/2,j,k} = \int_{-C_x}^{0} \eta_{iD}(s) A_{\mathrm{F},iD}(s) \Delta x \Delta y \Delta z ds$$

$$= \theta \left(A_{\mathrm{F},i+1/2,j,k} \int_{-C_x}^{0} \eta_{iD}(s) ds + a \int_{-C_x}^{0} s \eta_{iD}(s) ds \right) \tag{3.19}$$

The first integral in Eq. (3.19) is also present in the original THAINC without IB and can be calculated using Eq. (2.28). The second integral in Eq. (3.19) is calculated as follows:

$$\int_{-C_x}^{0} s \eta_{iD}(s) ds = \int_{-C_x}^{0} \frac{1}{2} \{ s + s\gamma \tanh \beta_x (s + \Gamma - \tilde{x}_{iD}) \} ds$$

$$= \left[\frac{s^2}{4} + \frac{\gamma}{2} (L_1 + L_2 + L_3) \right]_{-C_x}^{0} \tag{3.20}$$

where L_1, L_2, and L_3 are

$$L_1 = \frac{s^2 \tanh \beta_x (s + \Gamma - \tilde{x}_{iD})}{2} \tag{3.21}$$

$$L_2 = \frac{2s\beta_x \ln[m(s)+1] + \mathrm{Li}_2(-m(s))}{2\beta_x^2} \tag{3.22}$$

$$L_3 = \frac{s^2}{m(s)+1} - s^2 \tag{3.23}$$

where m and Li_2 are functions given by

$$m(s) = \exp[2\beta_x (s + \Gamma - \tilde{x}_{iD})] \tag{3.24}$$

$$\mathrm{Li}_2(\delta) = \sum_{l=1}^{\infty} \frac{\delta^l}{l^2} \exp[2\beta_x (s + \Gamma - \tilde{x}_{iD})] \tag{3.25}$$

Equation (3.20) can be rewritten as

$$\int_{-C_x}^{0} s\eta_{iD}(s)ds = -\frac{C_x^2}{4} - \frac{\gamma}{2}\left[M_1 + M_2 + M_3\right] \tag{3.26}$$

where M_1, M_2, and M_3 are given by

$$M_1 = \frac{C_x^2 \tanh\beta_x\left(-C_x + \Gamma - \tilde{x}_{iD}\right)}{2} \tag{3.27}$$

$$M_2 = \frac{-2C_x\beta_x \ln\left[m\left(-C_x\right)+1\right] + \mathrm{Li}_2\left(-m\left(-C_x\right)\right) - \mathrm{Li}_2\left(-m(0)\right)}{2\beta_x^2} \tag{3.28}$$

$$M_3 = \frac{C_x^2}{m\left(-C_x\right)+1} - C_x^2 \tag{3.29}$$

Ω_x at (i+1/2, j, k) also has to be modified to incorporate the presence of the solid:

$$\Omega_{x,i+1/2,j,k} = \int_{x_{i+1/2,j,k}-u_{i+1/2,j,k}\Delta t}^{x_{i+1/2,j,k}} A_{\mathrm{F},iD}(x)\Delta y\Delta z dx \tag{3.30}$$

Applying the variable transformation to the above equation yields

$$\begin{aligned}\Omega_{x,i+1/2,j,k} &= \int_{-C_x}^{0} A_{\mathrm{F},iD}(s)\Delta x\Delta y\Delta z ds \\ &= \theta\int_{-C_x}^{0}\left(A_{\mathrm{F},i+1/2,j,k} + as\right)ds \\ &= \theta\left(A_{\mathrm{F},i+1/2,j,k}C_x - \frac{aC_x^2}{2}\right)\end{aligned} \tag{3.31}$$

The second term in both J_x and Ω_x is an additional term that appears due to the presence of the solid phase. $A_{\mathrm{F},i+1/2,j,k}$ and a will take the values, 1 and 0, respectively in the absence of solid in the computational cell, giving us the same equations as THAINC.

The above procedure is summarized in Fig. 3.2 and is similarly applied to the y and z directions.

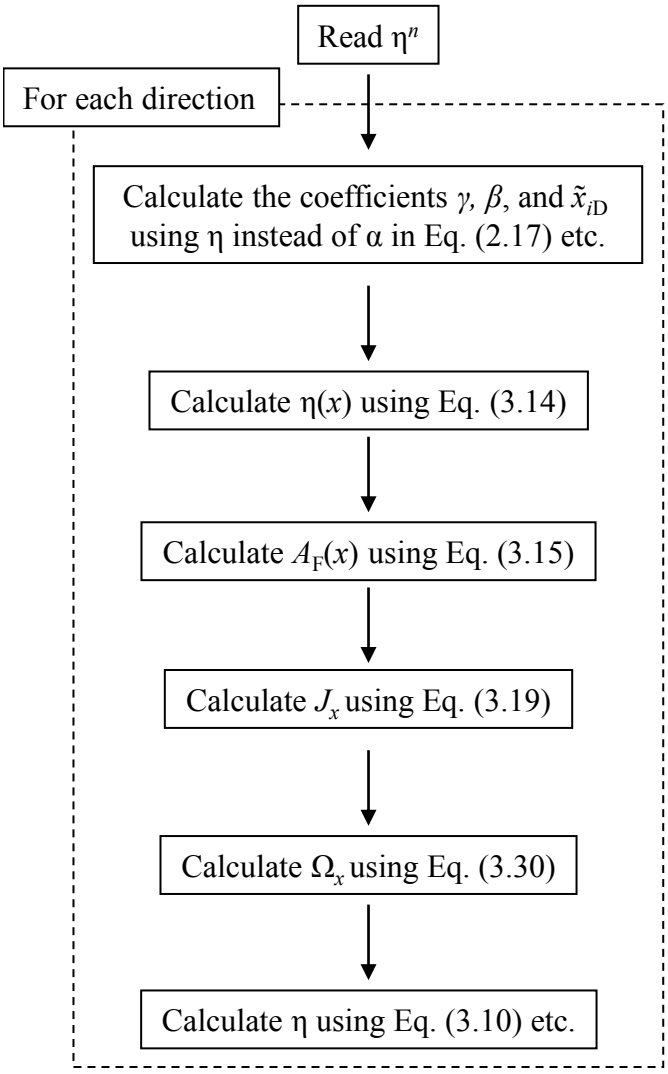

Fig. 3.2 Calculation procedure

3.2.3 Implementation of immersed boundary method

The direct forcing method proposed by Fadlun *et al.* (2000) was used to predict the fluid flow in the presence of solid phase. The solution of flow field requires information of velocity in the cells neighbouring the cell whose velocity is being computed. The velocities of the boundary cells must be set appropriately to ensure proper implementation of the boundary condition. An example of no-slip wall boundary condition is explained with the help of Fig. 3.3. Figure 3.3(a) shows a case when the cell is completely filled with solid or fluid, as in the case of THAINC in the previous chapter. Here the bottom cell is the boundary and the *x*-component of the velocity vector at the wall is set to zero by

$$u_{i+1/2,j-1,k} = -u_{i+1/2,j,k} \tag{3.32}$$

The presence of complex solid geometries may cause a cell face to be partially occupied by solid as shown in Fig. 3.3(b). In such a case, the boundary condition is implemented by

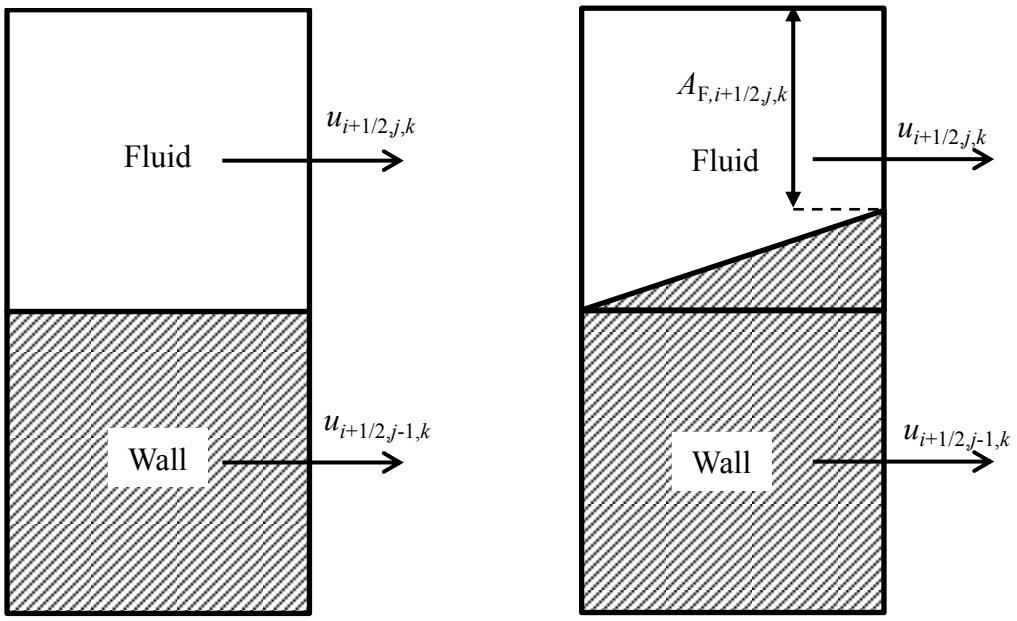

(a) No immersed boundary (b) Immersed boundary

Fig. 3.3 Implementation of wall boundary condition

$$u_{i+1/2,j-1,k} = -\left(\frac{1.5 - A_{\mathrm{F},i+1/2,j,k}}{A_{\mathrm{F},i+1/2,j,k} - 0.5}\right) u_{i+1/2,j,k} \tag{3.33}$$

The equation of continuity is discretized using the area fraction of the fluid phase:

$$\sum_{p=1}^{N_{\mathrm{face}}} \boldsymbol{V}_p \cdot \left(A_{\mathrm{F}} \boldsymbol{S}\right)_p = 0 \tag{3.34}$$

where N_{face} is the number of faces enclosing a computational cell. η is transported using the updated velocity.

3.2.4 Calculation of the A_{F} at a cell face

The procedure to compute A_{F} at a face is explained. The line fraction of the fluid at an edge, denoted as ζ, is introduced. In two-dimensional calculations, since a face is defined by an edge, A_{F} at a face can be calculated as

$$A_{\mathrm{F,Face}} = \zeta_{\mathrm{Edge}} \tag{3.35}$$

As for the three-dimensional problem, a face is defined by four edges, and its A_{F} is computed from the ζ of the four edges. Figure 3.4 shows a cell containing solid phase and its right face, located at (*i*+1/2,*j*,*k*). The face is defined by the right edge, left edge, top edge, and bottom edge located at (*i*+1/2,*j*+1/2,*k*), (*i*+1/2,*j*–1/2,*k*), (*i*+1/2,*j*,*k*+1/2), and (*i*+1/2,*j*,*k*–1/2) respectively. Using the four ζ values, the A_{F} is computed according to

$$A_{\mathrm{F,Face}} = \frac{1}{2}\left(\zeta_{\mathrm{R}} + \zeta_{\mathrm{L}}\right)\left(\zeta_{\mathrm{T}} + \zeta_{\mathrm{B}}\right) - \zeta_{\mathrm{R}}\zeta_{\mathrm{L}}\zeta_{\mathrm{T}}\zeta_{\mathrm{B}} \tag{3.36}$$

An edge is defined by a lower vertex and an upper vertex denoted by superscripts l and u, respectively. The ζ at an edge is defined as the sum of two components as shown in Fig. 3.5 according to

$$\zeta_{\text{Edge}} = \zeta^{\text{u}} + \zeta^{\text{l}} \tag{3.37}$$

For the edge that is aligned with the *y*-direction in two dimensions, ζ^{u} and ζ^{l} can be calculated as

$$\zeta^{\text{u}} = \max\left[\min\left(\frac{y^{\text{u}}_{\text{Edge}} - Y^{\text{u}}_{\text{f}}}{\Delta y}, 1\right), 0\right] \tag{3.38}$$

$$\zeta^{\text{l}} = \max\left[\min\left(\frac{Y^{\text{l}}_{\text{f}} - y^{\text{l}}_{\text{Edge}}}{\Delta y}, 1\right), 0\right] \tag{3.39}$$

where y_{Edge} is the location of the cell vertex in the *y*-direction and Y_{f} the location on the solid surface computed from the function f supplied by the user, defining the solid surface such that it satisfies

$$\text{f}\left(x^{K}_{\text{Edge}}, Y^{K}_{\text{f}}\right) = 0 \qquad (K = \text{u, l}) \tag{3.40}$$

where x_{Edge} is the location of the cell vertex in the *x*-direction. The above procedure can be similarly applied to edges aligned with the *x*-direction to compute their ζ values. Figure 3.6 shows the possible combinations of an edge and solid. Table 3.1 shows the value of ζ for each case.

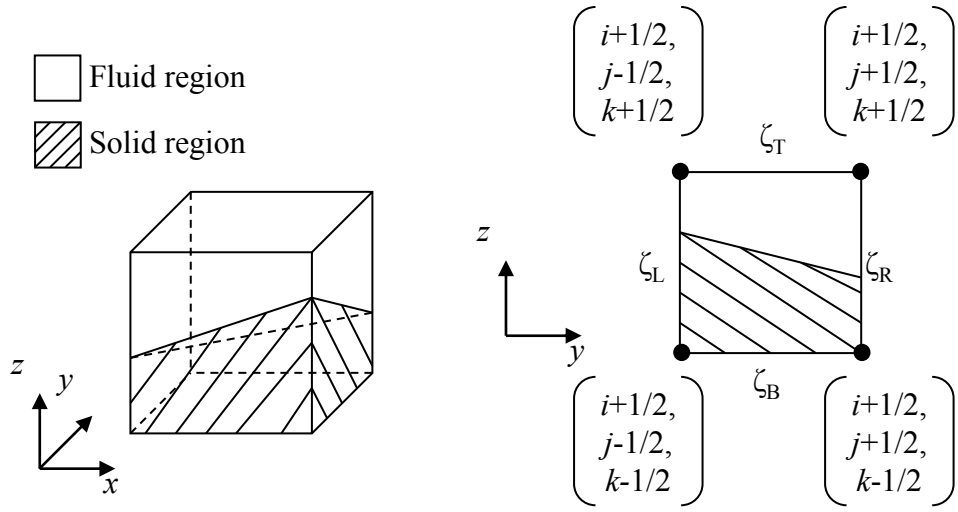

(a) Computational cell (i,j,k) (b) Right cell face of (i,j,k)

Fig. 3.4 Computational cell containing a fixed solid-fluid interface

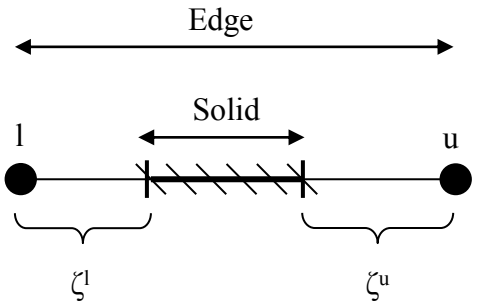

Fig. 3.5 Edge containing solid

Table 3.1 ζ value for an edge for different combinations

Combination	(a)	(b)	(c)	(d)	(e)
ζ^u	0	0	0	ε	1
ζ^l	1	ε	0	0	0
ζ_{Edge}	1	ε	0	ε	1

Note: $0<\varepsilon<1$

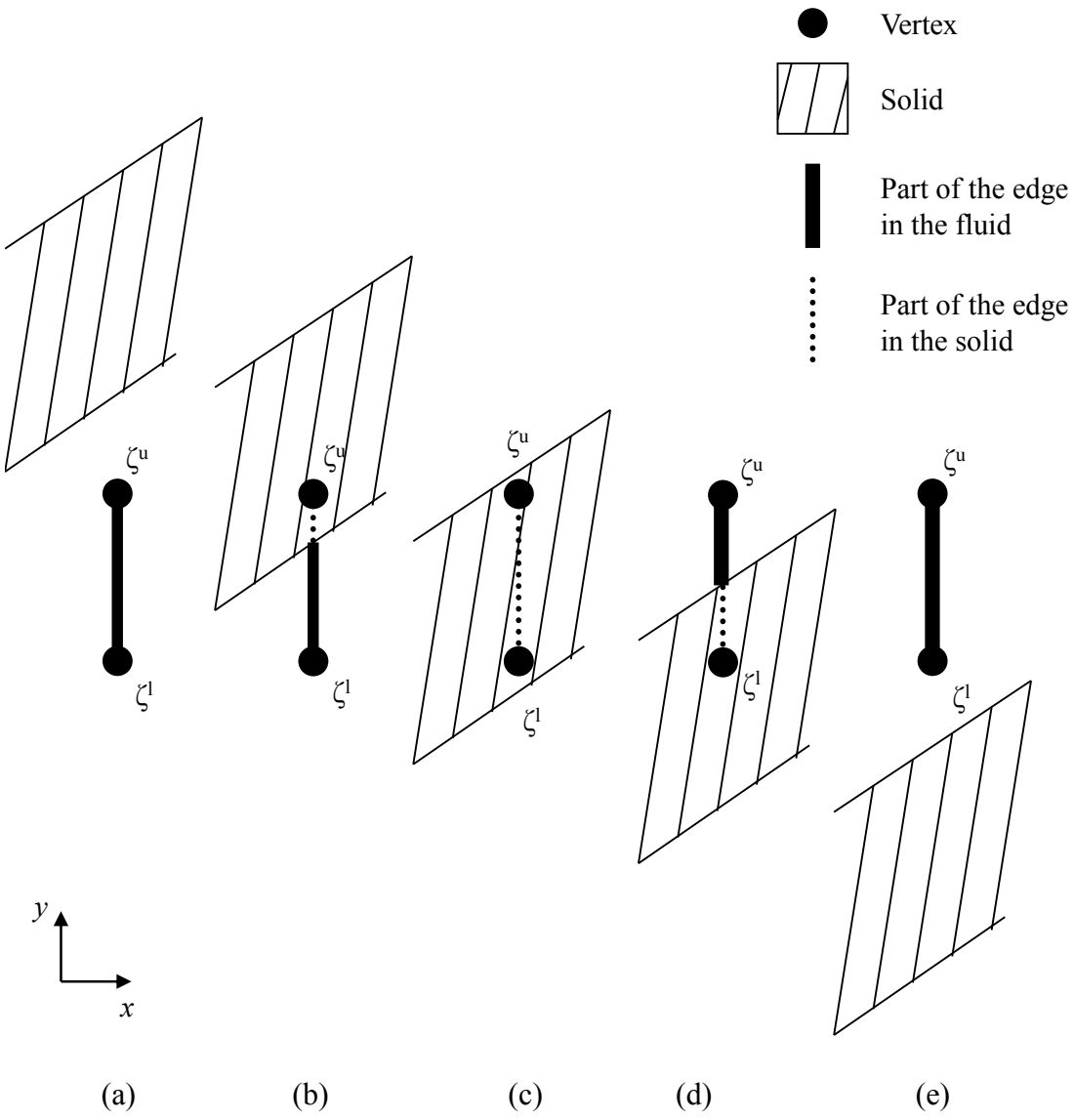

Fig. 3.6 Possible combinations of an edge and solid

For the three-dimensional case, ζ^{u} and ζ^{l} are calculated depending on the alignment of the edge with an axis according to

$$\zeta^{\mathrm{u}} = \begin{cases} \max\left[\min\left(\dfrac{x^{\mathrm{u}}_{\mathrm{Edge}} - X^{\mathrm{u}}_{\mathrm{f}}}{\Delta x},1\right),0\right], & \text{for Edges aligned with } x \text{ axis} \\ \max\left[\min\left(\dfrac{y^{\mathrm{u}}_{\mathrm{Edge}} - Y^{\mathrm{u}}_{\mathrm{f}}}{\Delta y},1\right),0\right], & \text{for Edges aligned with } y \text{ axis} \\ \max\left[\min\left(\dfrac{z^{\mathrm{u}}_{\mathrm{Edge}} - Z^{\mathrm{u}}_{\mathrm{f}}}{\Delta z},1\right),0\right], & \text{for Edges aligned with } z \text{ axis} \end{cases} \tag{3.41}$$

$$\zeta^{\mathrm{l}} = \begin{cases} \max\left[\min\left(\dfrac{X^{\mathrm{l}}_{\mathrm{f}} - x^{\mathrm{l}}_{\mathrm{Edge}}}{\Delta x},1\right),0\right], & \text{for Edges aligned with } x \text{ axis} \\ \max\left[\min\left(\dfrac{Y^{\mathrm{l}}_{\mathrm{f}} - y^{\mathrm{l}}_{\mathrm{Edge}}}{\Delta y},1\right),0\right], & \text{for Edges aligned with } y \text{ axis} \\ \max\left[\min\left(\dfrac{Z^{\mathrm{l}}_{\mathrm{f}} - z^{\mathrm{l}}_{\mathrm{Edge}}}{\Delta z},1\right),0\right], & \text{for Edges aligned with } z \text{ axis} \end{cases} \tag{3.42}$$

where X_{f}, Y_{f}, and Z_{f} are computed such that they satisfy

$$\begin{aligned} &\mathrm{f}\left(X^{K}_{\mathrm{f}}, y^{K}_{\mathrm{Edge}}, z^{K}_{\mathrm{Edge}},\right) = 0, && \text{for Edges aligned with } x \text{ axis} \\ &\mathrm{f}\left(x^{K}_{\mathrm{Edge}}, Y^{K}_{\mathrm{f}}, z^{K}_{\mathrm{Edge}},\right) = 0, && \text{for Edges aligned with } y \text{ axis} \qquad (K = \mathrm{u}, \mathrm{l}) \\ &\mathrm{f}\left(x^{K}_{\mathrm{Edge}}, y^{K}_{\mathrm{Edge}}, Z^{K}_{\mathrm{f}}\right) = 0, && \text{for Edges aligned with } z \text{ axis} \end{aligned} \tag{3.43}$$

3.3 Advection tests using THAINC-IB

3.3.1 Advection in one-dimension

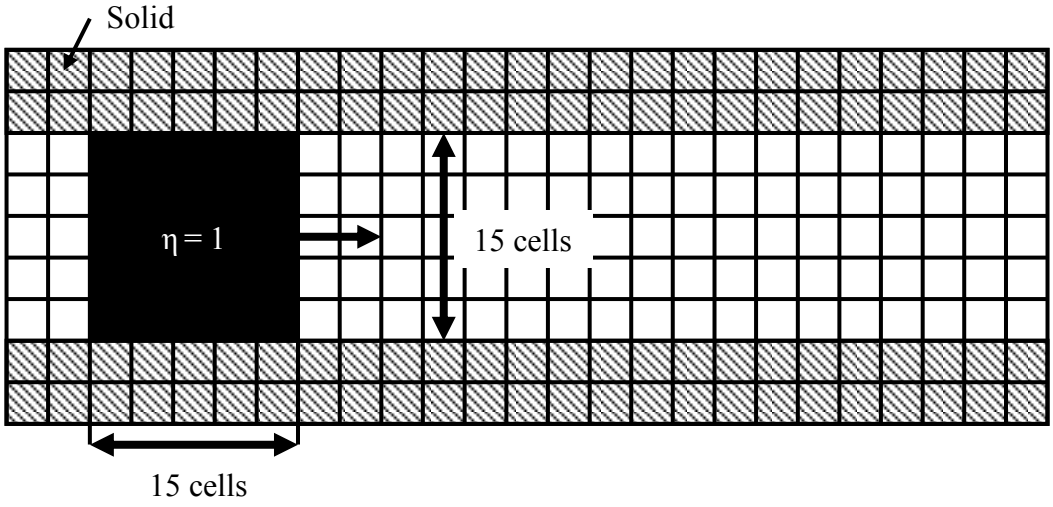

(a) Schematic of the calculation domain

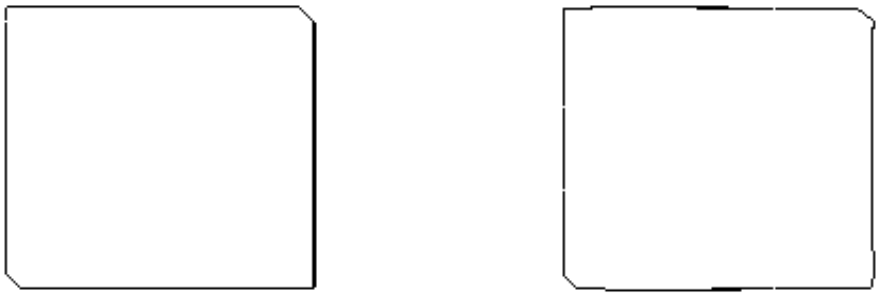

(b) Initial shape (c) Final shape

Fig. 3.7 Advection of a square in one-dimension by THAINC

The ability of THAINC-IB to accurately transport the phase in the presence of a solid was verified by transporting a square between two parallel walls. First the errors, E_S and E_V, were evaluated for one-dimensional transportation of a square between parallel walls such that the cells either contained only solid material or fluid as shown in Fig. 3.7(a). This resulted in calculation of the fluxes only by THAINC. The size of the square was 15×15 cells, and η was set at 1. The square was transported in the *x*-direction over a length of 5

times the width of the square. C_x was set at 0.25. The distortion in shape shown in Fig. 3.7(c) and the volume error after transportation were small, *i.e.*, $E_S = 2.8\%$, and $E_V = 10^{-8}\%$.

Next, the same advection test was carried out, but the square was positioned such that some of the cells contained both solid and fluids. The initial phase distributions were set by dividing the computational domain into three regions as shown in Fig. 3.8: (a) cells containing only solid phase, *i.e.*, $\alpha_S = 1$, (b) cells containing both fluid and solid phases, *i.e.*, $\alpha_F = 0.5$ and $\alpha_S = 0.5$, and (c) cells containing only fluid phases, *i.e.*, $\alpha_F = 1$. The errors, E_S and E_V, were found to be exactly the same as in the former case.

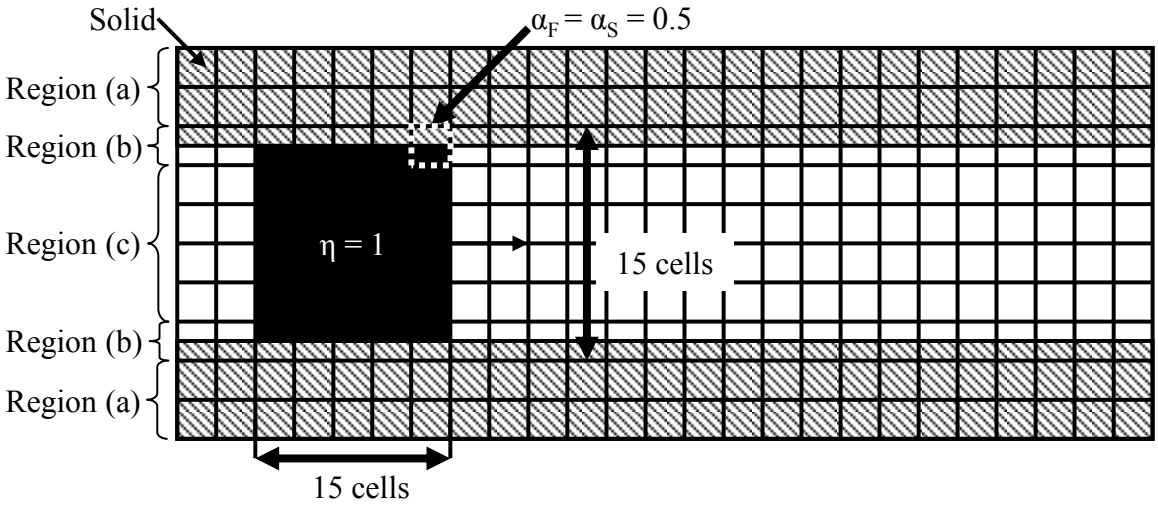

(a) Schematic of the calculation domain

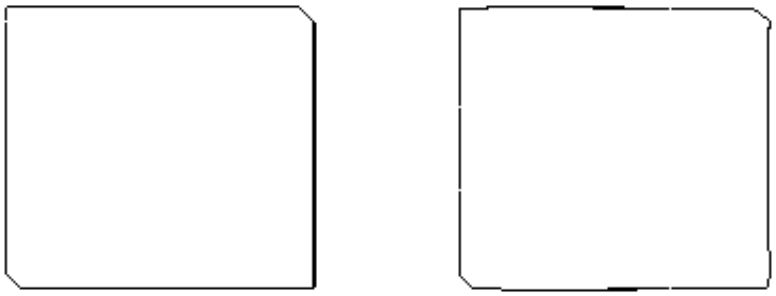

(b) Initial shape (c) Final shape

Fig. 3.8 Advection of a square in one-dimension by THAINC-IB

3.3.2 Advection in two-dimensions

A two-dimensional advection test was also carried out by transporting a square diagonally over a length equal to 5 times the width of the square. The square of size 15×15 cells with η = 1 was positioned as shown in Fig. 3.9. The following condition was used for numerical stability:

$$C_O \leq 0.25 \tag{3.44}$$

where the definition of C_O is

$$C_O = \frac{u_{i+1/2,j}\Delta t}{\alpha_F^{1/2}\Delta x} + \frac{v_{i,j+1/2}\Delta t}{\alpha_F^{1/2}\Delta y} \tag{3.45}$$

The reason for the use of Eq. (3.45) instead of Eq. (2.41) is as follows. In the presence of solid phase in the cell, the amount of fluid in the cell is no longer $\Delta x\Delta y$; rather it is $\alpha_F\Delta x\Delta y$. Enforcing the condition, Eq. (3.44), with Eq. (3.45) ensures that the amount of fluid to be advected from a cell is not more than the amount present in it and hence ensures numerical stability by preventing the value of η from going below 0. The following definition should be used for three-dimensional simulations:

$$C_O = \frac{u_{i+1/2,j,k}\Delta t}{\alpha_F^{1/3}\Delta x} + \frac{v_{i,j+1/2,k}\Delta t}{\alpha_F^{1/3}\Delta y} + \frac{w_{i,j,k+1/2}\Delta t}{\alpha_F^{1/3}\Delta z} \tag{3.46}$$

where w is the z component of the velocity. The shape of the square after advection with C_O = 0.25 is shown in Fig. 3.9(c). The E_S was 6.8%, and E_V was of the order of 10^{-2}%. This reduction in the volume was caused due to the loss of η formed in the direction of the wall because of numerical diffusion. In the previous example, this problem was not encountered since there was no advection in the y direction and due to the absence of any solid matter in the x-direction. This slight reduction in volume would be still acceptable for practical purposes.

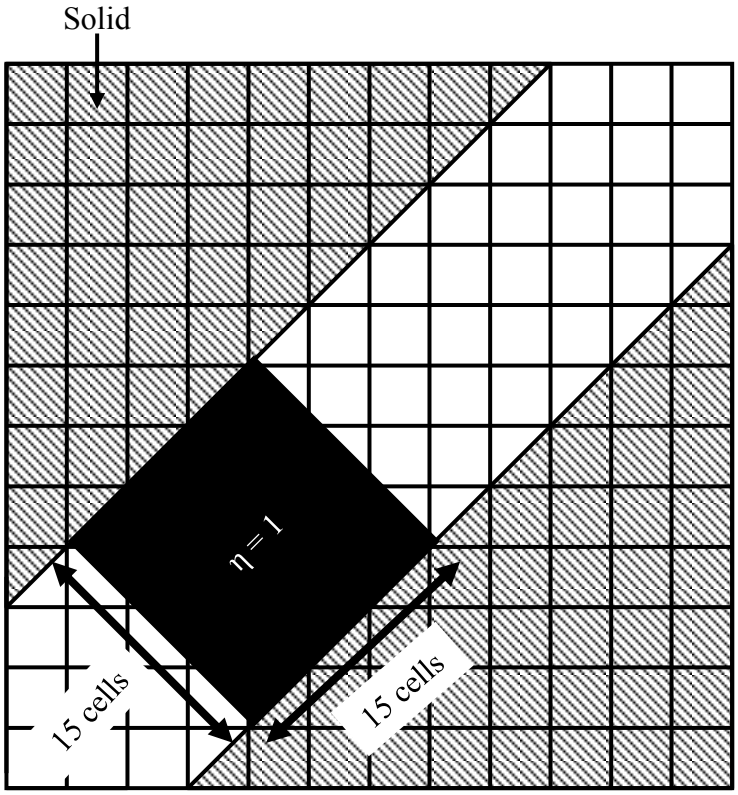

a) Schematic of the calculation domain

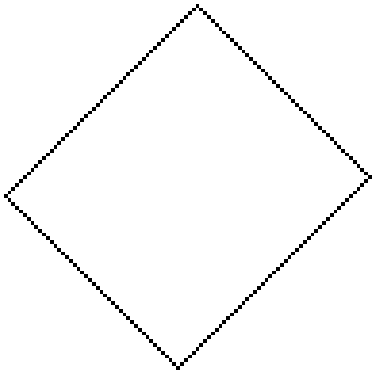

(b) Initial shape

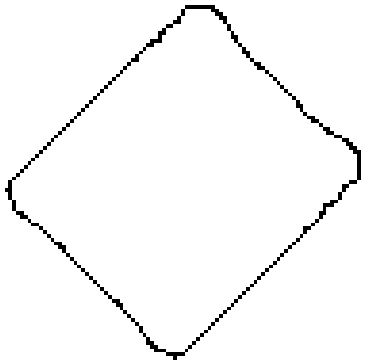

(c) Final shape

Fig. 3.9 Two-dimensional advection of a square in the presence of solid

3.4 Flow about cylindrical tubes in a staggered arrangement

To demonstrate the ability of the immersed boundary method, single phase flow around a bundle of cylindrical tubes in a two-dimensional channel shown in Fig. 3.10 was calculated. The boundaries of the channel were slip walls. The tubes were arranged in a staggered manner, and the flow was let in uniformly. The inlet velocity was altered, and its effect on the pressure drop between the inlet and outlet was calculated. The number of computational cells in the flow and orthogonal directions were 250 and 50, respectively. The number, N_T, of tubes in the flow direction was 10 and the diameter of the tubes, d_T, were 80 mm. The pitch, b, between two adjacent tubes was $1.5d_T$. The cell size was uniform, and its width was $0.125d_T$.

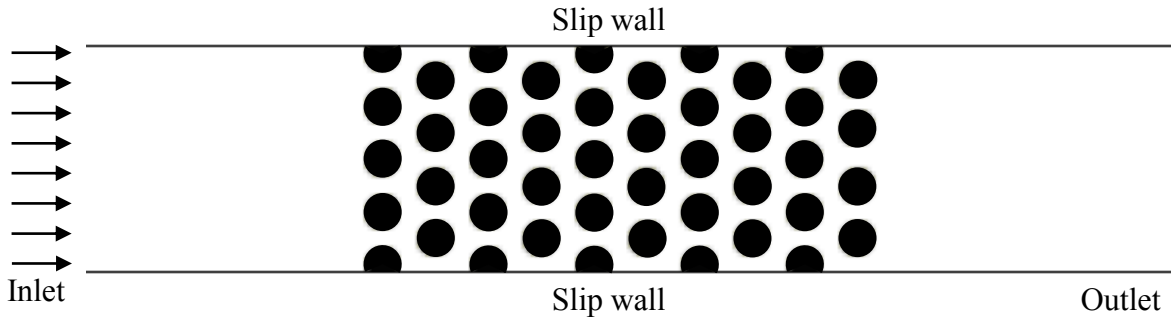

Fig. 3.10 Schematic of the flow channel

The friction factor, f_{tube}, was evaluated by substituting the predicted pressure drop ΔP across the tube bundle into

$$f_{tube} = \frac{1}{4}\frac{\Delta P}{\left(\rho U_{max}^2 / 2\right)}\frac{1}{N_T} \tag{3.47}$$

where U_{max} is the maximum velocity between the tubes defined by

$$U_{\max} = U_{\text{in}}\left(\frac{D}{D - n_{\text{c}} d_{\text{T}}}\right) \tag{3.48}$$

where U_{in} is the inlet velocity, D is the channel width, and n_{c} is the effective number of tubes per unit length of the cross-section, which is calculated as

$$n_{\text{c}} = \frac{D}{b} \tag{3.49}$$

The predicted f_{tube} was compared with the following empirical correlation proposed by Bergelin *et al.* (1952):

$$f_{\text{tube}} = \frac{70}{Re_{\text{v}}}\left(\frac{d_{\text{T}}}{b}\right)^{1.6} \tag{3.50}$$

where Re_{v} is the Reynolds number defined by

$$Re_{\text{v}} = \frac{d_{\text{v}} \rho U_{\max}}{\mu} \tag{3.51}$$

where d_{v} is the hydraulic diameter and the maximum velocity between the tubes defined by

$$d_{\text{v}} = 4\frac{b^2 - \pi\frac{d_{\text{T}}^2}{4}}{\pi d_{\text{T}}} \tag{3.52}$$

Figure 3.11 shows the relation between f_{tube} and Re_{v}. Good agreement between the prediction and correlation is obtained. Figure 3.12 shows a velocity profile for $Re_{\text{v}} = 32$. A reasonable prediction of the velocity field is obtained.

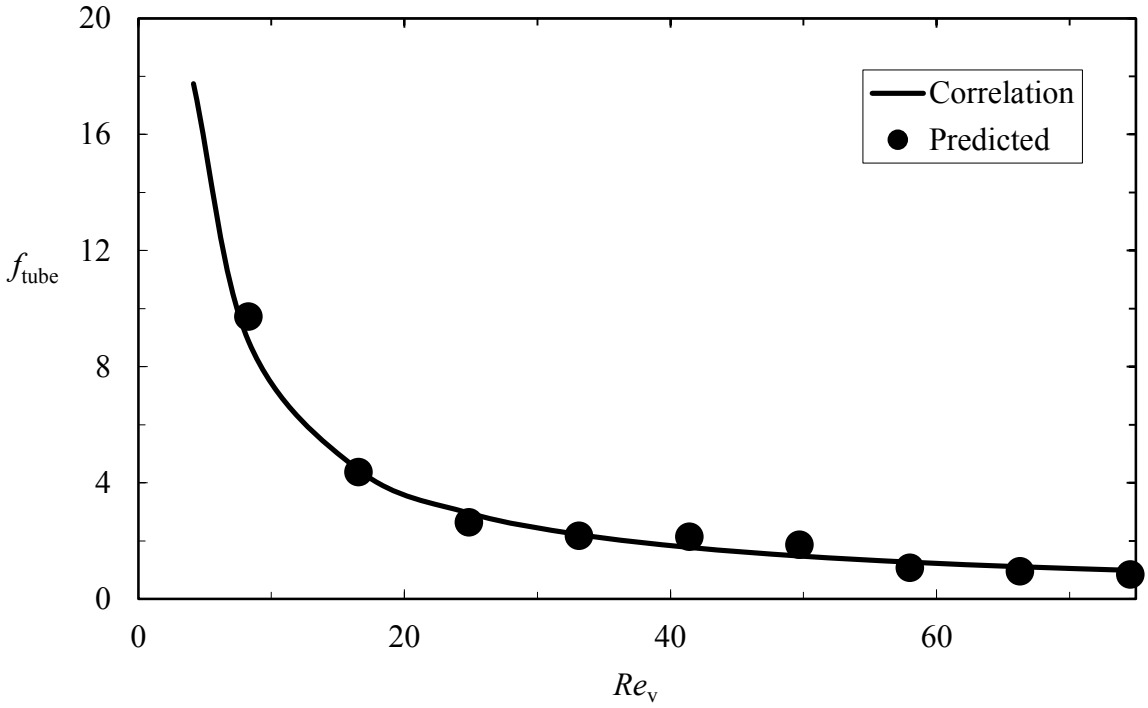

Fig. 3.11 Comparison of different friction factor values versus Reynolds number

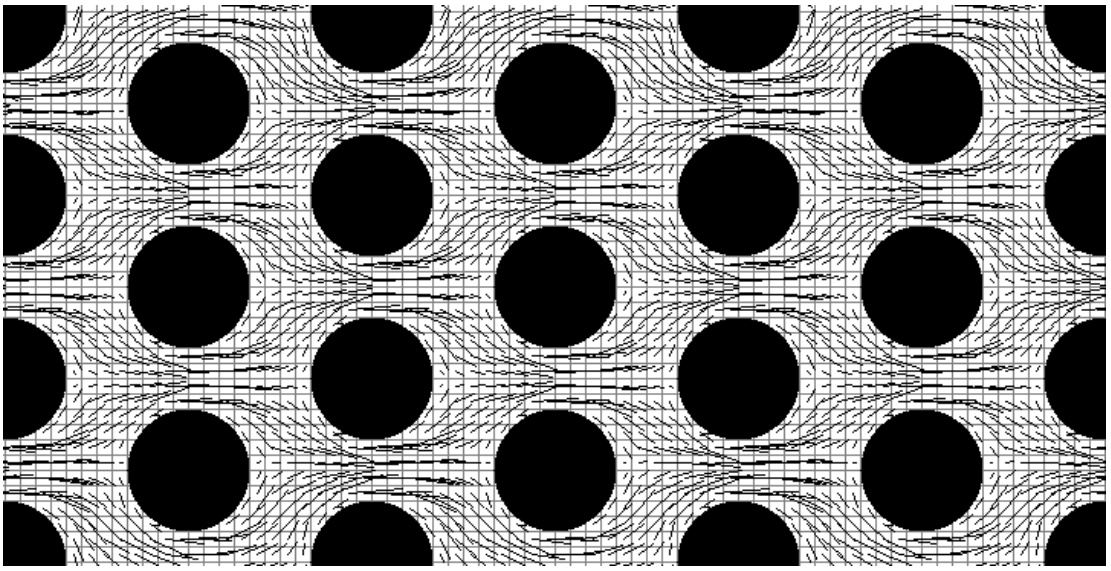

Fig. 3.12 Velocity distribution, $Re_v = 32$

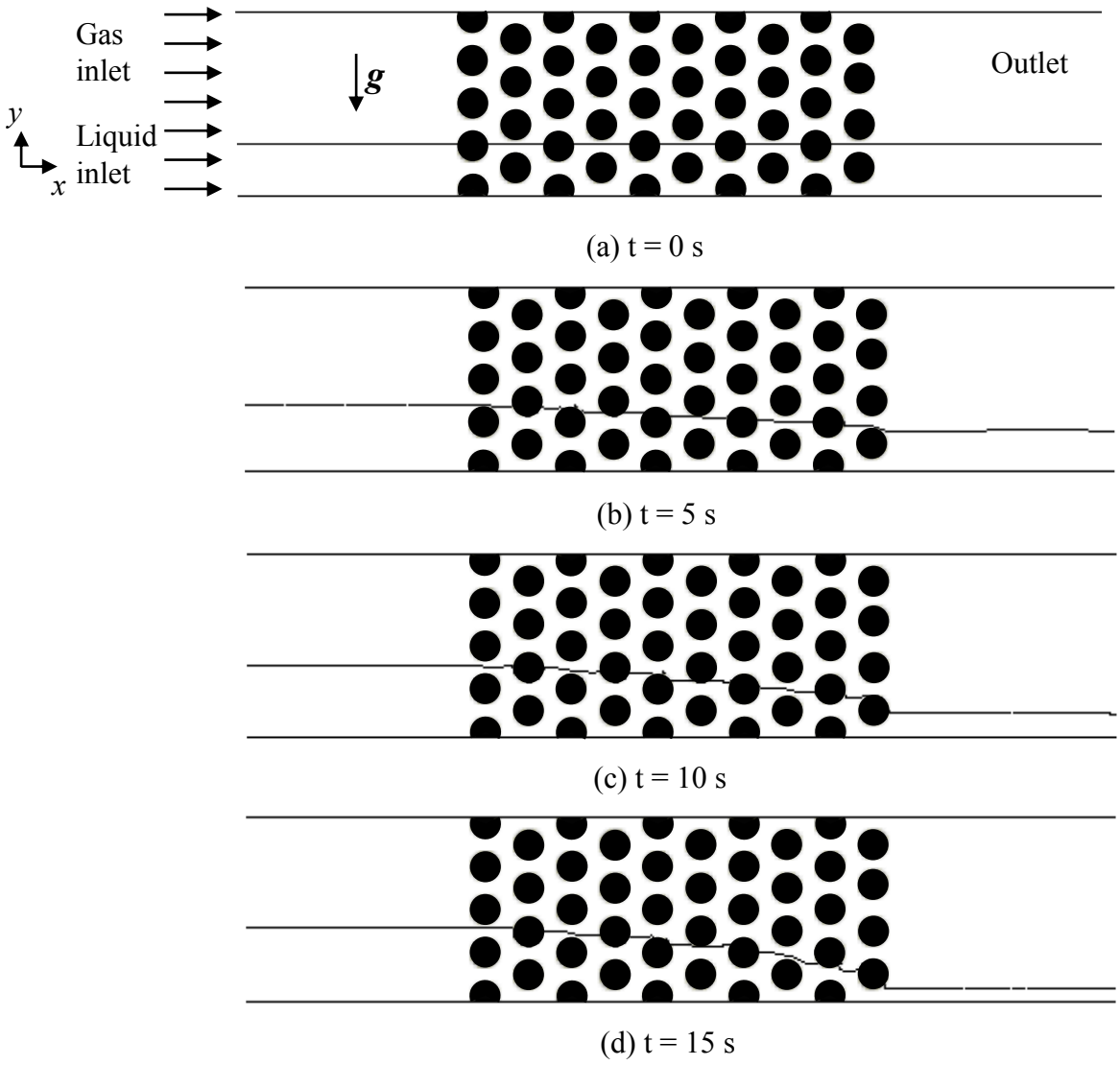

Fig. 3.13 Liquid layer flowing into a staggered arrangement of cylinders

A simulation of a gas–liquid two-phase flow in this geometry was also carried out to demonstrate the applicability of the proposed method to two-phase flows in complex geometries. The initial condition is shown in Fig. 3.13(a). Initially, a liquid layer with a height of 15 cells was assumed. The liquid and gas uniformly flowed into the domain from the left boundary at a constant velocity of 0.1 m/s. The following Neumann boundary condition for η was imposed on both the inlet and outlet:

$$\frac{\partial \eta_K}{\partial x} = 0 \qquad (K = \text{G, L}) \tag{3.53}$$

The liquid height in the upstream of the tubes increases with time as shown in Fig. 3.13(b), (c), and (d). This can be attributed to the large pressure drop due to the presence of the tubes, and this behaviour is physically reasonable. This example has demonstrated the capability of THAINC-IB to handle a two-phase flow in a complex geometry.

3.5 Flow over an obstacle

A two-dimensional water column under the influence of gravity as shown in Fig. 3.14 (a) was calculated. This problem is known as the "broken dam problem." The number of computational cells was 80×100 with the cell size of 0.0073 m. The height, T, and width, W, of the computational domain were 0.73 m and 0.584 m, respectively. The height, H, and width, L, of the water column were 0.292 m and 0.146 m, respectively. The predicted position, Z, of the water front is compared with the experimental data (Koshizuka *et al.*, 1997) in Fig. 3.14(b), in which Z^* is the dimensionless front position and T^* is the dimensionless time defined by

$$Z^* = \frac{Z}{L} \tag{3.54}$$

$$T^* = t\sqrt{\frac{Ng}{L}} \tag{3.55}$$

where N is the aspect ratio of the water column defined as

$$N = \frac{H}{L} \tag{3.56}$$

The prediction agrees well with the experimental data.

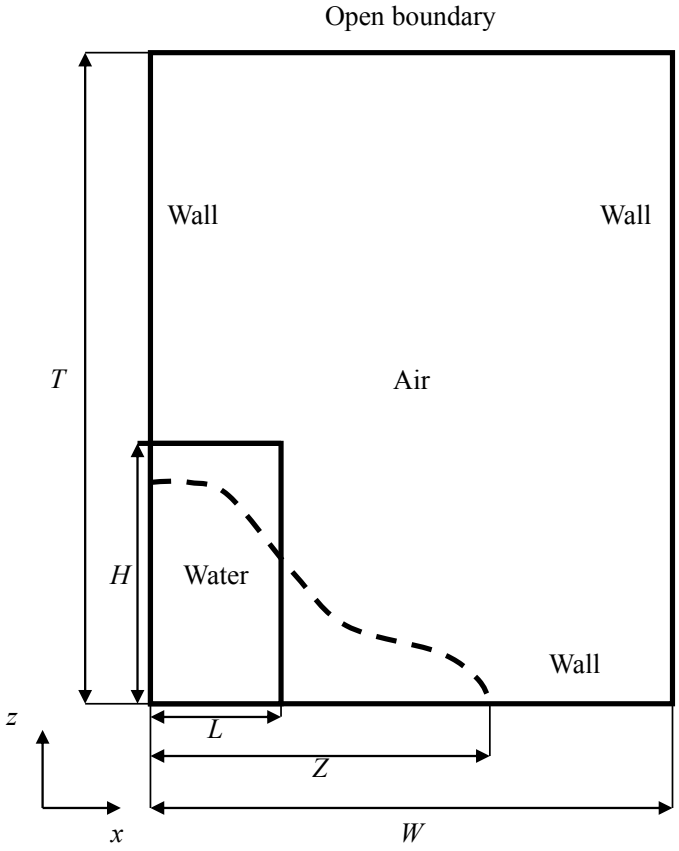

(a) Schematic of the computational domain

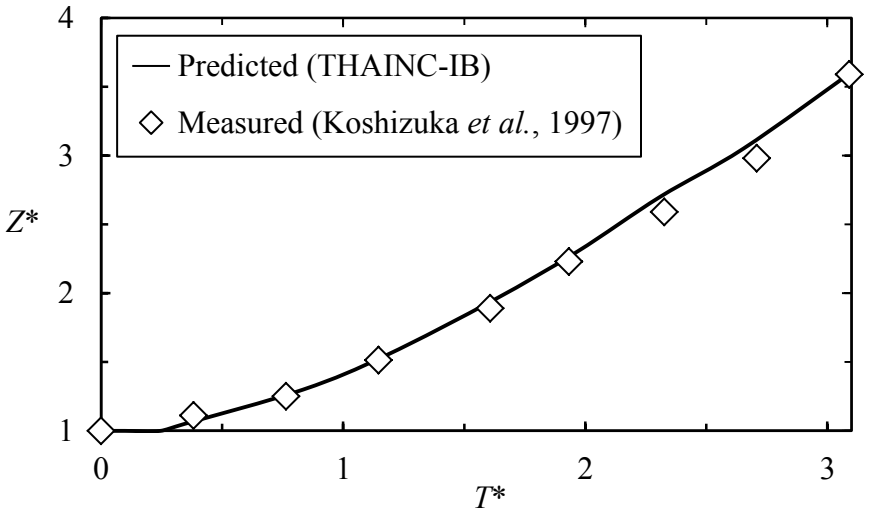

(b) Water front tip position as a function of time

Fig. 3.14 Broken dam in the absence of a containment dyke

Then water flowing over an obstacle (Greenspan and Young, 1978) was simulated. A schematic of the calculation domain is shown in Fig. 3.15. The numbers of computational cells in the *x* and *y* directions were 300 and 200, respectively, and the cell size was 0.00254 m in each direction. The initial height of the water column was 0.2032 m while the width was 0.2286 m. A right-angled triangular dyke of angle 60° was placed at a distance, *R*, of 0.2286 m from the water front. The height of the dyke, *A*, was 0.1016 m.

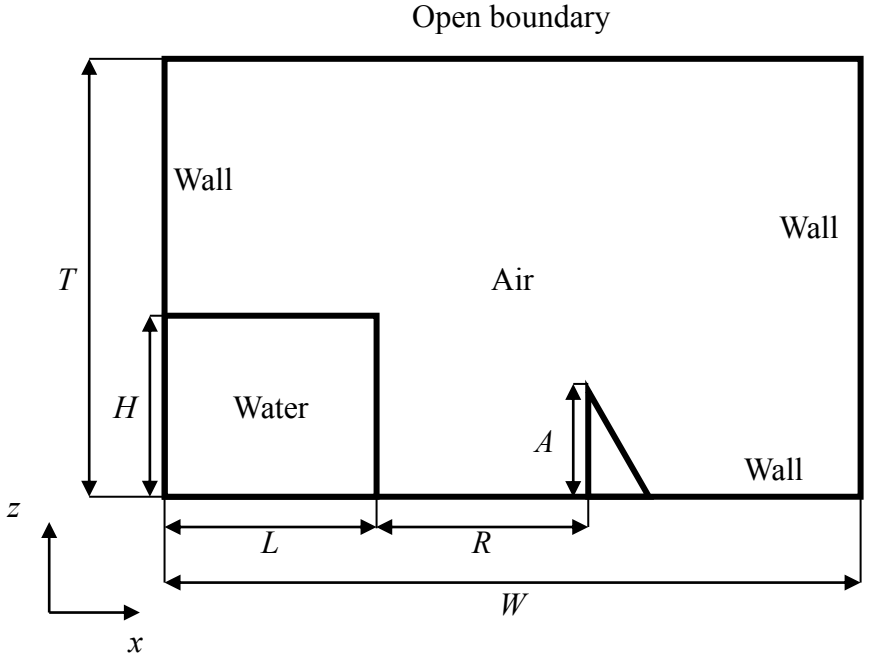

Fig. 3.15 Schematic of flow over a containment dyke

A comparison between the experiment (Greenspan and Young, 1978) and simulation is shown in Fig. 3.16. The prediction was in good agreement with the experiment. The amount of spillage, which is the water that spills over and is collected on the right hand side of the dyke, was computed in the simulation and compared with the experimental data for a quantitative comparison. The spillage in the experiment was reported as 21% of the initial volume of the water, and in the simulation it was 20.5%. Hence, the simulation was able to accurately predict the spillage within a relative error of 2.4%. To demonstrate THAINC-IB's ability to maintain the sharpness of the interface, the distribution of η along the dotted

line in Fig. 3.16(b) is shown in Fig. 3.17. The sharpness of the interface was maintained even after large interface deformation.

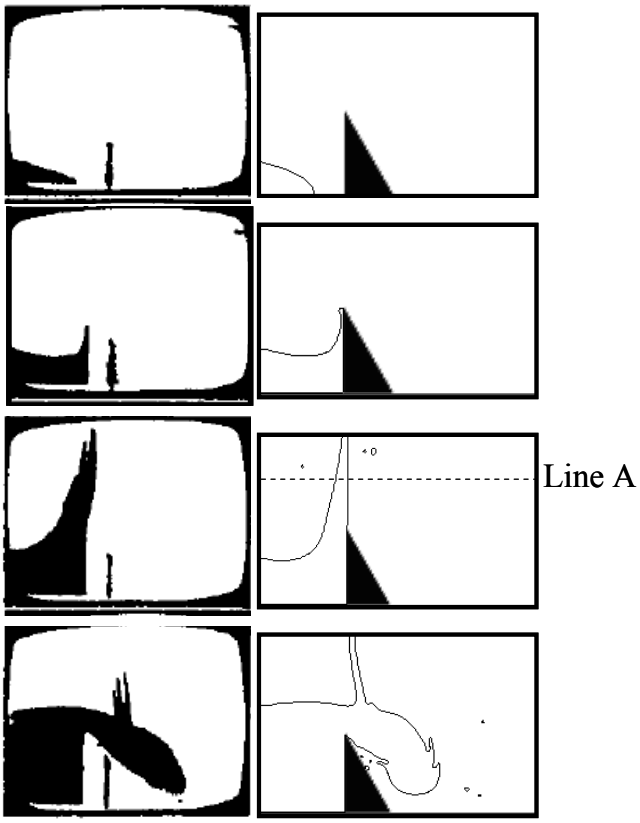

(a) Experiment (b) Simulation

Fig. 3.16 Comparison of the flow over a containment dyke

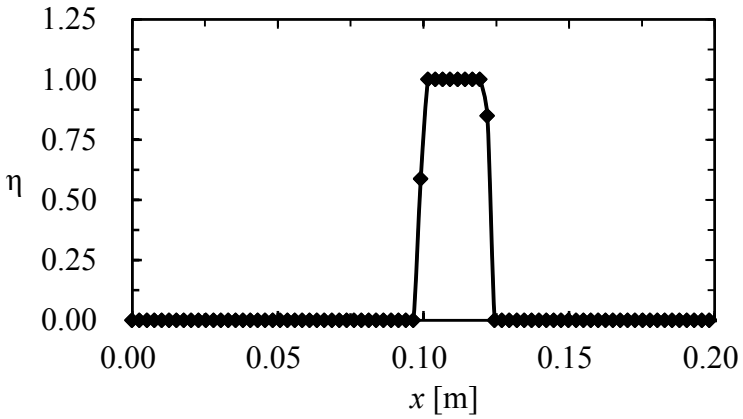

Fig. 3.17 η distribution along the cross-section at Line A

3.6 Conclusions

A numerical method, THAINC-IB, for predicting the motion of gas–liquid interface in the presence of complex solid geometry in the flow domain was developed. First the transport equations of the fluid volume fractions in the presence of a stationary solid were derived. The method for solving the transport equation of the gas volume fraction is based on the THAINC developed in the previous chapter, whereas the immersed boundary method proposed by Fadlun *et al*. (2000) is implemented so as to deal with complicated solid geometries. The proposed method does not need to reconstruct the interface configuration in a computational cell as in PLIC-type methods. Owing to this feature, implementation of this method to three-dimensions is easier compared to the methods implementing geometric reconstruction. The applicability of THAINC-IB was examined through several tests: linear transportations of a square, flows about cylindrical tubes in a staggered arrangement, and dam break problems. As a result, the following conclusions were obtained:

(1) THAINC-IB conserves the fluid volumes well.

(2) The errors in the transported interface shape predicted using THAINC-IB are small.

(3) Pressure drops due to the presence of many cylinders in a staggered arrangement are well predicted.

(4) The motion of a water column in the presence of a triangular dyke is accurately predicted using THAINC-IB.

(5) The interface sharpness is well preserved even after large interface deformation.

References

Bergelin, O. P., Brown, G. A., Doberstein, S. C., Heat transfer and fluid friction during flow across banks of tubes-IV, *Transactions ASME*, 1952, 74, pp. 953-960.

Fadlun, E. A., Verzicco, R., Orlandi, P., Mohd-Yusof, J., Combined immersed-boundary finite-difference methods for three-dimensional complex flow simulations, *Journal of Computational Physics*, 2000, 161, pp. 35-60.

Greenspan, H. P., Young, R. E., Flow over a containment dyke, *Journal of Fluid Mechanics*, 1978, 87, pp. 179-192.

Hayashi, K., Sou, A., Tomiyama, A., A volume tracking method based on non-uniform subcells and continuum surface force model using a local level set function, *Computational Fluid Dynamics Journal*, 2006, 15, pp. 225-232.

Koshizuka, S., Oka, Y., Kondo, S., A staggered differencing technique on boundary-fitted curvilinear grids for incompressible flows along curvilinear or slant walls, *Computational Mechanics*, 1990, 7, pp. 123-136.

Landsberg, A. M., The virtual cell embedding method: A simple approach for gridding complex geometries, *AIAA*, 1997, 97-1982.

Noor, D. Z., Chern, M. J., Horng, T. L., An immersed boundary method to solve fluid–solid interaction problems, *Computational Mechanics*, 2009, 44, 4, pp. 447-453.

Peskin. C. S., Numerical analysis of blood flow in the heart, *Journal of Computational Physics*, 1977, 25, pp. 220-252.

Paravento, F., Pourquie, M. J., Boersma, B. J., An immersed boundary method for complex flow and heat transfer, *Flow, Turbulence and Combustion*, 2008, 80, pp. 187-206.

Rider, W. J., Kothe, D. B., Reconstructing volume tracking, *Journal of Computational*

Physics, 1998, 141, pp. 112-152.

Sussman, M., Smereka, P., Osher, S., A level set approach for computing solutions to incompressible two-phase flow, *Journal of Computational Physics*, 1994, 114, pp. 146-159.

Takada, N., Tomiyama, A., A numerical method for two-phase flow based on a phase-field model, *Transactions JSME Series B*, 2005, 71, pp. 117-124.

Takewaki, K., Yabe, T., The cubic-interpolated pseudo particle (CIP) method: Application to nonlinear and multi-dimensional hyperbolic equations, *Journal of Computational Physics*, 1987, 70, pp. 355-372.

Chapter 4

Assessment of numerical treatments for evaluation of surface tension force in interface capturing simulations

4.1 Introduction

Droplet sizes varying from sub-micron to a few hundred micron meters are often encountered in coating processes. The accurate prediction of wetting behaviour of droplets of such scales is important since it plays an important role in the quality of coating. Interface tracking methods based on the volume-of-fluid method enable us to deal with the interface motion of a droplet with accurate mass conservation. Due to the presence of gas-liquid interface of micron and sub-micron meter length scale, the surface tension force is the dominant force affecting the behaviour of gas-liquid interface motion. Hence, the accurate evaluation of the surface tension force is of primal importance when simulating the surface-tension-driven interface motion.

In Chapters 2 and 3, a numerical method for accurate transport of the gas-liquid interface was proposed and equipped to handle the presence of complex solid geometries. However, its accurate transport also depends on the accurate estimation of the surface tension force which directly affects the flow field on which the transport of the gas-liquid interface is based. The surface tension force estimation in the previous chapters was based on CSF model (Brackbill *et al.*, 1992). This model however cannot accurately evaluate the interface

curvature when using the volume fraction as a scalar function. The numerical errors in surface tension force are known to cause the so-called spurious current. One of the remedies for the inaccurate evaluation is to use a level set function reconstructed from the volume fraction for the curvature evaluation instead of the volume fraction. This method is referred to as the coupled level set and volume-of-fluid (CLSVOF) method (Sussman *et al.*, 1994; Hayashi *et al.*, 2014). Although CLSVOF is more accurate than the original CSF, its computational cost is higher due to the re-initialization of level set function. In addition, Cummins *et al.* (2005) pointed out that the error in curvature evaluated using the reconstructed level set function does not decrease with increasing spatial resolution. They also showed that the height function is the best from the point of view of accuracy and computational cost, provided that the interface is resolved with a sufficient spatial resolution. Popinet (2009) improved the height function method, in which the computational stencil is adjusted for capturing the interface configuration.

Francois *et al.* (2006) pointed out that the cause of spurious current is not only the error in curvature but also the inappropriate discretization for the normal to the interface in CSF. They proposed a modified discretization, which is called the balanced-force algorithm (BFA), to assure the force balance between the pressure and surface tension force in an equilibrium state. The combination of the height function and balanced-force algorithm gives the most accurate evaluation of the surface tension force.

The contact angle affects the behaviour of gas-liquid interface on a solid surface and hence its proper modelling is also necessary. The static contact angle between a solid surface and the gas–liquid interface has been taken into account in interface tracking methods (Brackbill *et al.*, 1992; Yokoi *et al.*, 2009; Afkhami *et al*., 2004; 2007). In CSF, the unit normal to the gas–liquid interface at a solid surface in curvature evaluation is given so as to satisfy the specified static contact angle (Brackbill *et al.*, 1992). Afkhami *et al*. (2004, 2007) extended the height function method to deal with the static contact angle and implemented the balanced-force algorithm for accurate predictions. They compared CSF with their method for static drops on a solid surface and confirmed that their method gives

much smaller spurious currents. However the comparisons were made only for mili/sub-mili meter drops and accuracy tests for smaller droplets such as sub-micron meter droplets appearing in coating process have not been carried out yet. With decreasing the drop size, the surface tension force becomes dominant so that spurious currents may strongly affect predictions of very small droplets. In addition, Afkhami *et al.* (2004; 2007) did not account for the dynamic contact angle, which is of great importance in wetting processes in reality.

In this chapter, the surface tension force calculation based on the height function method proposed by Popinet (2009) and balanced force algorithm is implemented into the proposed interface tracking method, THAINC (tangent of hyperbola with adaptive slope for interface capturing). Effects of droplet size on numerical errors in surface tension force are investigated by varying the sizes of static droplets from mili to sub-micron meters. In addition, a model of dynamic contact angle proposed by Yokoi *et al.* (2009) is implemented into the height function method. Dynamic wetting by a mili-meter sized clean water drop (Yokoi *et al.*, 2009) is simulated using the proposed method and the results are compared with those obtained from CSF and CLSVOF. A simulation of a sub-micron meter clean water droplet is carried out using the dynamic contact angle model to examine whether or not the proposed method can stably simulate the motion of a sub-micron meter droplet.

4.2 Evaluation of surface tension force

The evaluation of surface tension force, Eq. (2.33), requires calculation of $\boldsymbol{N}$ and κ. Since a staggered variable arrangement is used for each variable, it requires surface tension forces to be calculated at the cell faces. The effect of numerical techniques for computing $\boldsymbol{N}$ and κ to evaluate surface tension force on the prediction of a drop in two-dimensional Cartesian coordinates will be given in detail in the following sections.

4.2.1 Normal vector, $\boldsymbol{N}$

In this study, two schemes for computing $\boldsymbol{N}$ were examined. One of them is a scheme utilized in the original CSF, which is referred to as the ALE (Arbitrary Lagrangian-Eulerian) like scheme. The other scheme is the one used in the balanced-force algorithm (Francois *et al.*, 2006).

4.2.1.1 Arbitrary Lagrangian-Eulerian (ALE) like scheme

A brief description of the ALE like scheme is given below. The x and y components, N_x and N_y, of $\boldsymbol{N}$ at the cell vertex, (i+1/2, j+1/2), are calculated using the four neighbouring cell centre values of α shown in Fig. 4.1(a):

$$N_{x,i+1/2,j+1/2} = \frac{\alpha_{i+1,j} + \alpha_{i+1,j+1} - \alpha_{i,j} - \alpha_{i,j+1}}{2\Delta x} \tag{4.1}$$

$$N_{x,i+1/2,j+1/2} = \frac{\alpha_{i+1,j} + \alpha_{i+1,j+1} - \alpha_{i,j} - \alpha_{i,j+1}}{2\Delta x} \tag{4.2}$$

$\boldsymbol{N}$ at the cell centre is computed by taking the average of $\boldsymbol{N}$ at the four vertices of the cell:

$$\boldsymbol{N}_{i,j} = \frac{\boldsymbol{N}_{i+1/2,j+1/2} + \boldsymbol{N}_{i-1/2,j+1/2} + \boldsymbol{N}_{i+1/2,j-1/2} + \boldsymbol{N}_{i-1/2,j-1/2}}{4} \tag{4.3}$$

The components N_x and N_y required at (i+1/2, j) and (i, j+1/2), respectively, for the momentum equations are computed by taking the average of those at the cell centres:

$$N_{x,i+1/2,j} = \frac{N_{x,i,j} + N_{x,i+1,j}}{2} \tag{4.4}$$

$$N_{y,i,j+1/2} = \frac{N_{y,i,j} + N_{y,i,j+1}}{2} \tag{4.5}$$

4.2.1.2 Balanced-force algorithm

Francois *et al*. (2006) proposed the balanced-force algorithm for a collocated variable arrangement. Their method was implemented for the staggered variable arrangement in this study. Francois *et al*. (2006) showed that the pressure jump across the interface will be $\sigma\kappa$ if the discretization of α in Eq. (2.35) is carried out in the same manner as that of the pressure term in the momentum equations, *i.e.*

$$\left.\frac{\partial P}{\partial x}\right|_{i+1/2,j} = \frac{P_{i+1,j} - P_{i,j}}{\Delta x} \tag{4.6}$$

$$\left.\frac{\partial P}{\partial y}\right|_{i,j+1/2} = \frac{P_{i,j+1} - P_{i,j}}{\Delta y} \tag{4.7}$$

Hence, as shown in Fig. 4.1(b), $\boldsymbol{N}$ at the cell face is computed by

$$N_{x,i+1/2,j} = \frac{\alpha_{i+1,j} - \alpha_{i,j}}{\Delta x} \tag{4.8}$$

$$N_{y,i,j+1/2} = \frac{\alpha_{i,j+1} - \alpha_{i,j}}{\Delta y} \tag{4.9}$$

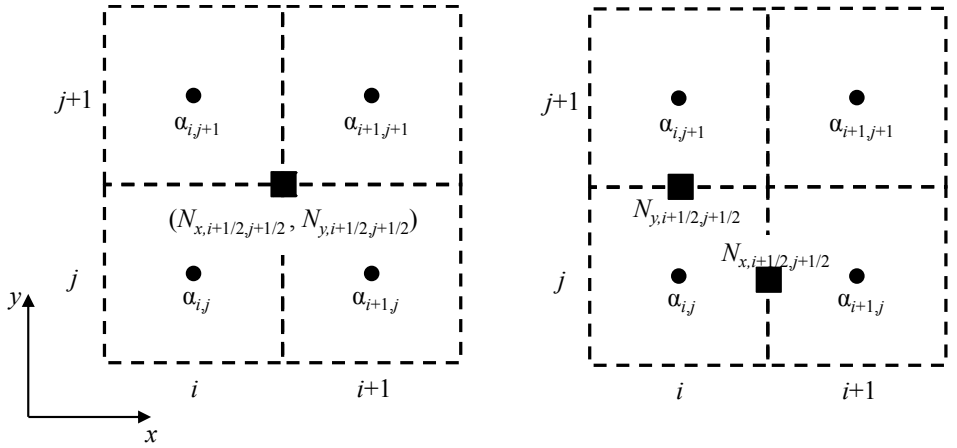

(a) ALE like scheme (b) BFA

Fig. 4.1 Variable arrangement in a grid

4.2.2 Interface curvature calculation

The interface curvature is calculated at the cell centre and then interpolated to the cell face by taking the weighted average of the neighbouring cell centre values (Renardy and Renardy, 2002) as follows:

$$\kappa_{i+1/2,j} = \frac{w_{i,j}\kappa_{i,j} + w_{i+1,j}\kappa_{i+1,j}}{w_{i,j} + w_{i+1,j}} \tag{4.10}$$

where w is the weight given by

$$w_{i,j} = \alpha_{i,j}\left(1-\alpha_{i,j}\right) \tag{4.11}$$

This ensures that the interpolated curvature value at the cell face is close to the curvature of the nearest interface.

4.2.2.1 Continuum surface force (CSF)

Equation (2.36) can be written as

$$\kappa_{\mathrm{CSF}} = -\nabla\cdot\left(\frac{\boldsymbol{N}}{|\boldsymbol{N}|}\right) \tag{4.12}$$

The above equation can also be transformed into the following form by applying the chain rule

$$\kappa_{\mathrm{CSF}} = \frac{1}{|\boldsymbol{N}|}\left[\left(\frac{\boldsymbol{N}}{|\boldsymbol{N}|}\cdot\nabla\right)|\boldsymbol{N}| - \nabla\cdot\boldsymbol{N}\right] \tag{4.13}$$

The calculation of curvature using Eq. (4.13) instead of Eq. (4.12) yields better results (Brackbill *et al.*, 1992). The interface normal used in this case is the ALE like scheme.

4.2.2.2 Height function (HF)

The height function based on a variable stencil proposed by Popinet (2009) is used. In this method, the stencil is adjusted to capture the interface completely. The basic idea is explained with the help of a vertical stencil shown in Fig. 4.2, and this can be easily extended to a horizontal stencil. The individual stencil for calculating a height for the cell containing an interface, (i, j), is selected such that the starting cell, (i, j_1), is completely filled with the dispersed phase while the last cell, (i, j_0), is completely empty. The height, h, is then defined by

$$h_{i,j} = \sum_{k=j_1}^{k=j_0} \alpha_{i,k} \Delta y \tag{4.14}$$

The choice of stencils is based on the orientation of the interface. A horizontal stencil is used if the interface is more vertical, *i.e.* $|N_x|>|N_y|$, else a vertical stencil is used. The interface normal computed using the method described in Section 4.2.1.1 is used to determine the orientation of the interface. The interface normal used to compute the curvature for the vertical stencil shown in Fig. 4.2 is defined by

$$\boldsymbol{N} = \left(\frac{\partial h}{\partial x}, -1 \right) \tag{4.15}$$

The first order derivative of h with respect to x is computed by the second-order centred difference scheme:

$$\frac{\partial h}{\partial x} = \frac{h_{i+1,j} - h_{i-1,j}}{2\Delta x} \tag{4.16}$$

Substituting Eq. (4.15) into Eq. (4.12) yields

$$\kappa_{HF} = \frac{-\dfrac{\partial^2 h}{\partial x^2}}{\left[1+\left(\dfrac{\partial h}{\partial x}\right)^2\right]^{3/2}} \tag{4.17}$$

The second order derivative of h with respect to x is computed by the second-order centred difference scheme:

$$\frac{\partial^2 h}{\partial x^2} = \frac{h_{i+1,j} - 2h_{i,j} + h_{i-1,j}}{\Delta x^2} \tag{4.18}$$

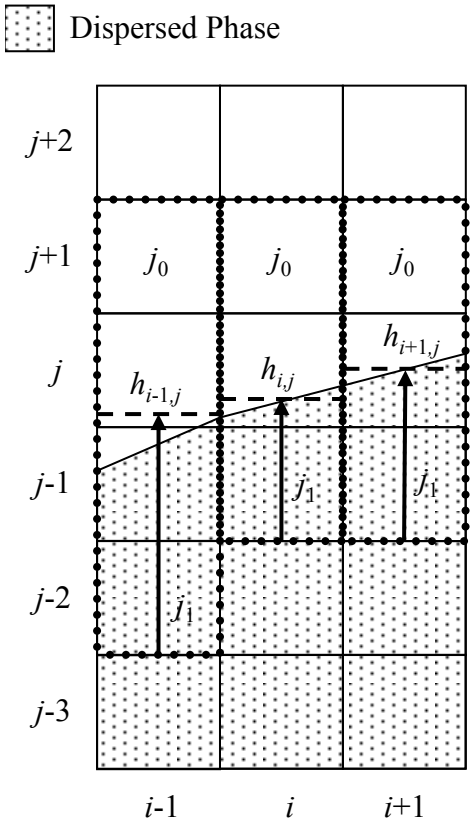

Fig. 4.2 Variable stencil for calculation of heights

The calculation of curvature at a cell containing interface requires its neighbouring heights. In the case of using the heights based on variable stencils as compared to fixed stencils, there is a large possibility that not all heights begin from the same baseline, as illustrated in

Fig. 4.2, and the heights have to be readjusted so that all the three heights, $h_{i\text{-}1,j}$, $h_{i,j}$, and $h_{i+1,j}$, have the same baseline. This is done by identifying the heights that need to be adjusted, $h_{i,j}$ and $h_{i+1,j}$ for the case shown in Fig. 4.2.

4.2.3 Wall treatment

An interface cell on the wall requires special treatment to implement the contact angle. In the case of CSF, this is carried out by modifying the unit normal vector used to calculate the curvature. Brackbill *et al*. (1992) proposed to compute the unit normal vector at points on the solid surface by

$$\boldsymbol{n} = \boldsymbol{n}_w \cos\Phi + \boldsymbol{n}_t \sin\Phi \tag{4.19}$$

where Φ is the contact angle, $\boldsymbol{n}_w$ the unit inward normal vector of the wall, and $\boldsymbol{n}_t$ the unit tangent vector of the wall pointing into the dispersed phase. An example of $\boldsymbol{n}_w$ and $\boldsymbol{n}_t$ is shown in Fig. 4.3.

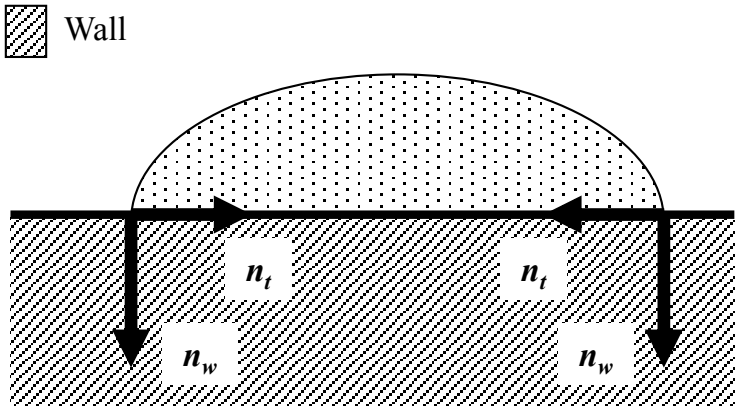

Fig. 4.3 Unit normal vector of the wall

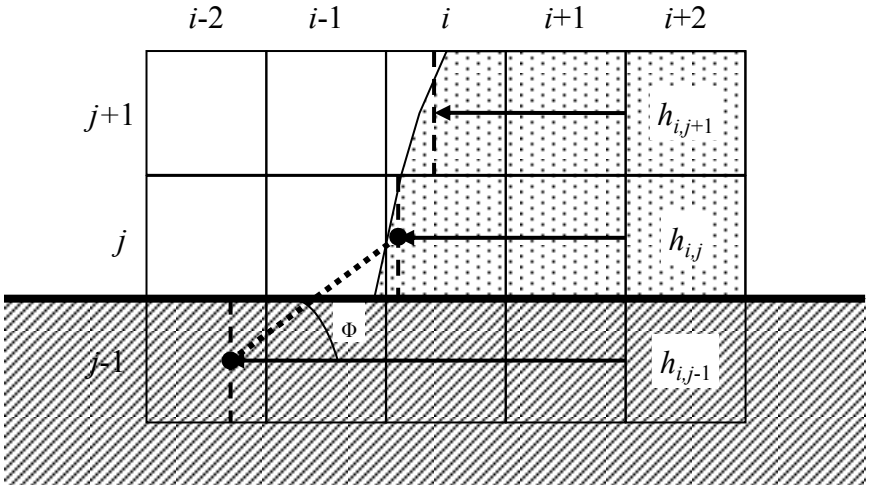

(a) Horizontal stencil

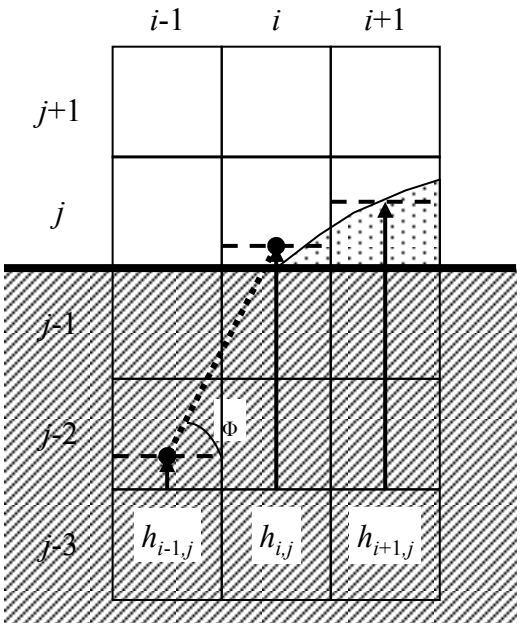

(b) Vertical stencil

Fig. 4.4 Contact angle implementation in HF

The contact angle implementation to the height function is carried out using the same procedure proposed by Afkhami *et al*., (2007). The contact angle is implemented by interpolating the height inside the wall in such a manner that the angle between the height

inside the wall and the central height is kept equal to the contact angle as shown in Fig. 4.4. When the stencil is horizontal (Fig. 4.4(a)), the height can be interpolated using

$$h_{i,j-1} = h_{i,j} + \frac{\Delta y}{\tan\Phi} \tag{4.20}$$

whereas, when the stencil is vertical (Fig. 4.4(b)),

$$h_{i,j-1} = h_{i,j} - \Delta x \tan\Phi \tag{4.21}$$

The volume fractions for cells inside the wall are required for computing the heights in the cells close to the walls. This is done by extending the interface inside the wall as shown in Fig. 4.5, and assigning values of α to these cells accordingly.

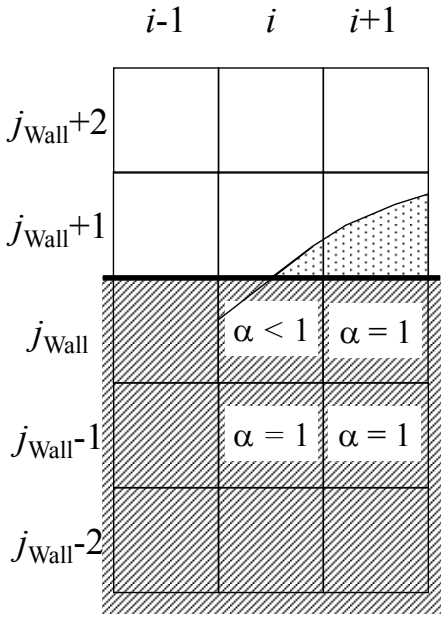

Fig. 4.5 Interpolation of α value for cells inside the wall

4.3 Validation of the code

The effects of the numerical treatments of $\boldsymbol{N}$ and κ on the accuracy of prediction have often been investigated in literature (Cummins *et al.*, 2005; Francois *et al.*, 2005) through simulations of neutrally buoyant circular drops. Hence the developed numerical code was validated by examining whether or not results of the benchmark test obtained with the code are similar to those in literature.

Due to the point symmetry of a neutrally buoyant circular drop, the surface tension forces at all the interface points should take the same value. Hence, the drop should not have any motion and the pressure jump across the interface, ΔP_{INT} shall follow Laplace's formula:

$$\Delta P_{\mathrm{INT}} = \sigma\kappa \tag{4.22}$$

The theoretical value of curvature for the circle is

$$\kappa_{\mathrm{TH}} = \frac{1}{R} \tag{4.23}$$

where R is the radius of the drop. Different combinations of curvatures, namely κ_{CSF}, κ_{HF}, and κ_{TH}, and normal vectors, $\boldsymbol{N}_{\mathrm{ALE}}$ and $\boldsymbol{N}_{\mathrm{BFA}}$, described in Section 4.2, were examined, where the subscripts ALE and BFA denote the ALE like scheme and the balanced-force algorithm, respectively.

The accuracy was evaluated by calculating the magnitude, $|\boldsymbol{V}_{\mathrm{MAX}}|$, of the maximum Samspurious current and the error in pressure, Err_P, defined by

$$Err_P = \frac{\left|\Delta P_{\mathrm{MAX}} - \Delta P_{\mathrm{INT}}\right|}{\Delta P_{\mathrm{INT}}} \tag{4.24}$$

where ΔP_{MAX} is the difference between the maximum and minimum pressures in the calculation domain.

The physical properties of water and air at 25 °C and 1 atm were used. The tests were carried out for a drop of radius R = 1 mm. The drop size used was of the same order as that in Francois *et al.* (2006). The effect of spatial resolution was checked by using mesh sizes of 50×50 and 100×100. A uniform cell size, $\Delta = \Delta x = \Delta y$, is used in the following for simplicity. The R/Δ, for 50×50 and 100×100 meshes were 10 and 20, respectively. The simulations were carried out until α distribution, *i.e.* the shape, and spurious currents did not change with time. The errors for the two spatial resolutions are summarized in Tables 4.1 and 4.2, respectively.

Table 4.1 Errors in velocity and pressure for 1 mm drop using 50×50 mesh

Normal vector	$\boldsymbol{N}_{ALE}$			$\boldsymbol{N}_{BFA}$		
Curvature	κ_{CSF}	κ_{HF}	κ_{TH}	κ_{CSF}	κ_{HF}	κ_{TH}
Err_P [%]	9.47	0.90	1.91	15.77	0.50	2.40×10^{-11}
$\lvert\boldsymbol{V}_{MAX}\rvert$ [m/s]	8.94×10^{-2}	6.85×10^{-2}	5.44×10^{-2}	4.76×10^{-2}	4.66×10^{-8}	1.47×10^{-13}

Table 4.2 Errors in velocity and pressure for 1 mm drop using 100×100 mesh

Normal vector	$\boldsymbol{N}_{ALE}$			$\boldsymbol{N}_{BFA}$		
Curvature	κ_{CSF}	κ_{HF}	κ_{TH}	κ_{CSF}	κ_{HF}	κ_{TH}
Err_P [%]	3.70	6.65	0.08	18.16	0.11	2.80×10^{-11}
$\lvert\boldsymbol{V}_{MAX}\rvert$ [m/s]	9.53×10^{-2}	1.17×10^{-1}	5.66×10^{-2}	4.04×10^{-2}	3.56×10^{-8}	1.11×10^{-13}

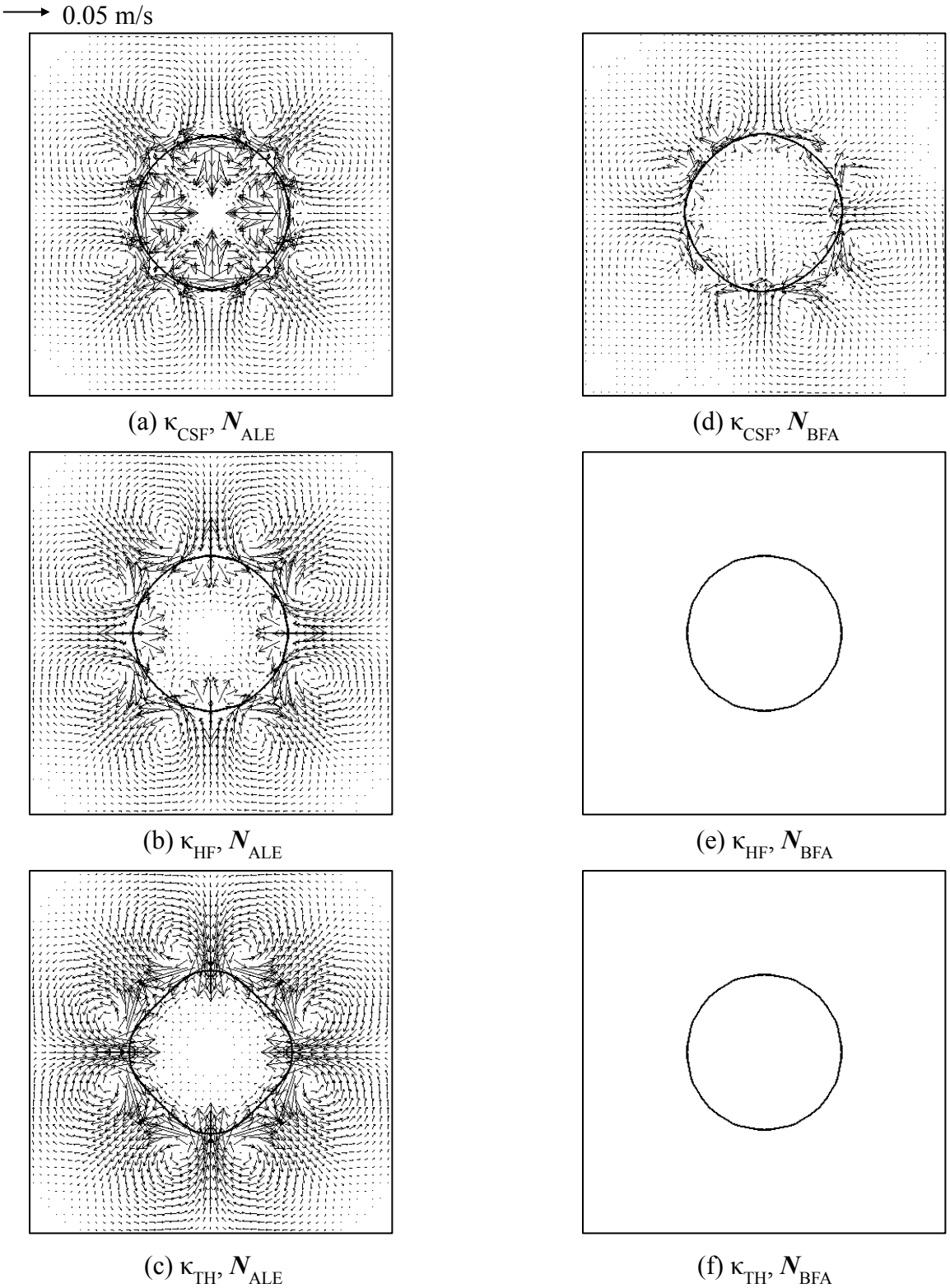

(a) κ_{CSF}, $\boldsymbol{N}_{ALE}$ (d) κ_{CSF}, $\boldsymbol{N}_{BFA}$

(b) κ_{HF}, $\boldsymbol{N}_{ALE}$ (e) κ_{HF}, $\boldsymbol{N}_{BFA}$

(c) κ_{TH}, $\boldsymbol{N}_{ALE}$ (f) κ_{TH}, $\boldsymbol{N}_{BFA}$

Fig. 4.6 Spurious currents for 1 mm droplet on 50×50 mesh

Figure 4.6 shows the spurious currents in the case of 50×50. The use of $\boldsymbol{N}_{\mathrm{ALE}}$ resulted in larger spurious currents compared with $\boldsymbol{N}_{\mathrm{BFA}}$ for the same method for κ. $\boldsymbol{N}_{\mathrm{ALE}}$ gave the same order of spurious currents for both methods of κ calculation and the spurious current did not attenuate even with the theoretical curvature. This result indicates that despite a very accurate evaluation of κ, spurious currents will be generated due to the numerical errors caused by $\boldsymbol{N}_{\mathrm{ALE}}$. On the other hand, $\boldsymbol{N}_{\mathrm{BFA}}$ gave very small errors in the case of theoretical curvature. The errors reduced with increasing the spatial resolution in the case of height function. Accurate evaluation of local mean curvature as well as appropriate discretization for $\boldsymbol{N}$ are therefore very important to reduce the spurious currents, and the combination of $\boldsymbol{N}_{\mathrm{BFA}}$ and κ_{HF} is the best among the available schemes for $\boldsymbol{N}$ and κ. These results are similar to those in literature (Francois *et al*., 2006); hence the validity of the present code has been confirmed.

4.4 Numerical tests for neutrally buoyant droplets

Simulations of R = 10 μm and 0.1 μm droplets were also carried out using $\boldsymbol{N}_{\mathrm{BFA}}$ and the two methods for curvature, CSF and HF, to examine the effects of the droplet size on the numerical errors. The mesh used was 100×100 and R/Δ was 20. The errors are shown in Table 4.3 and the spurious currents are shown in Fig. 4.7. No significant change was found in the order of errors for both CSF and HF with the change in droplet size, and the combination of $\boldsymbol{N}_{\mathrm{BFA}}$ and κ_{HF} is most accurate. This demonstrates the ability of the combination of $\boldsymbol{N}_{\mathrm{BFA}}$ and κ_{HF} to accurately simulate sub-micron meter droplets.

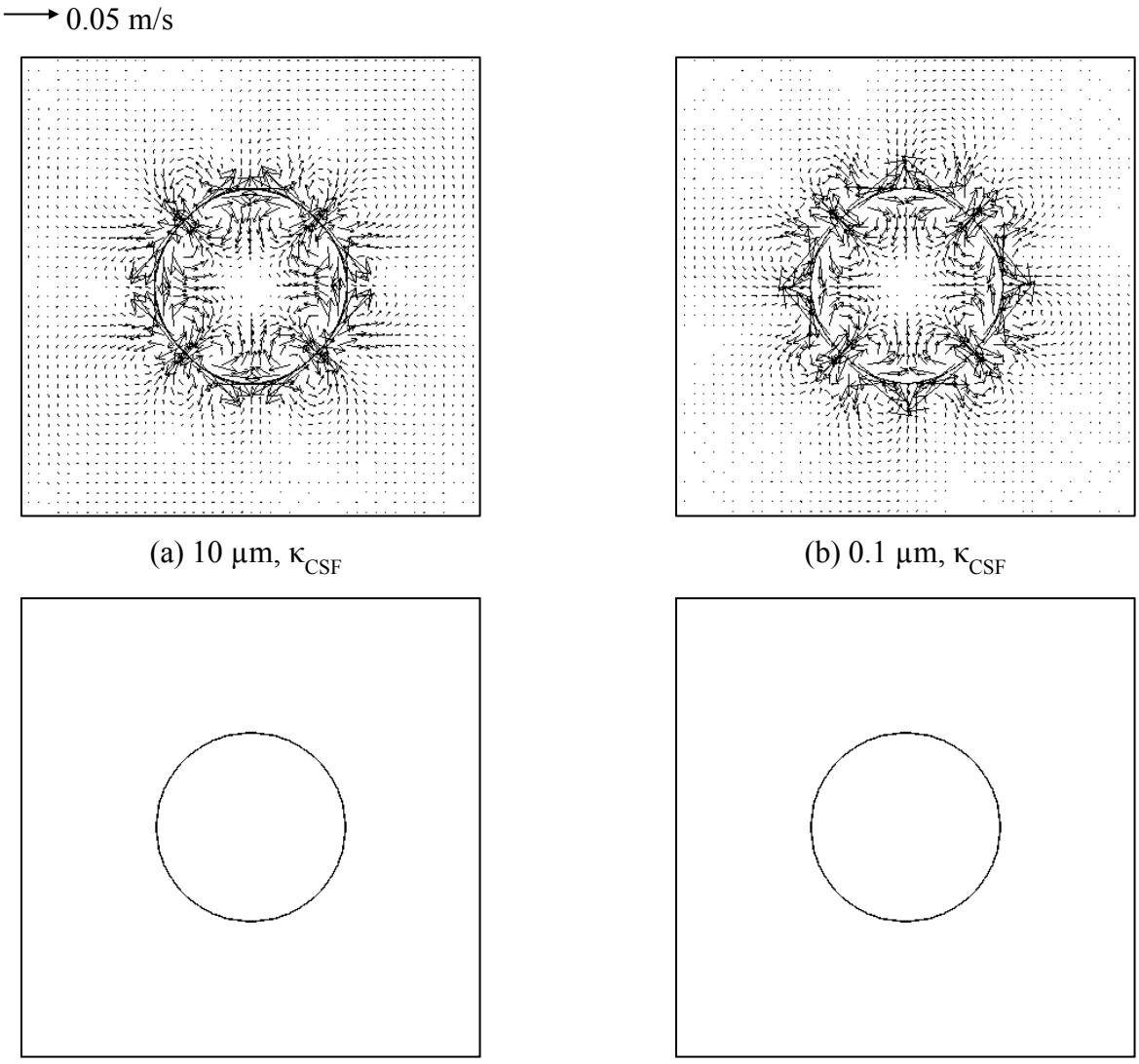

(a) 10 μm, κ_{CSF} (b) 0.1 μm, κ_{CSF}

(c) 10 μm, κ_{HF} (d) 0.1 μm, κ_{HF}

Fig. 4.7 Spurious currents for different droplet sizes

Table 4.3 Errors in velocity and pressure for 10 μm and 0.1 μm droplets

Droplet size	10 μm		0.1 μm	
Curvature	κ_{CSF}	κ_{HF}	κ_{CSF}	κ_{HF}
Err_P [%]	15.01	0.12	15.98	0.12
$\lvert \boldsymbol{V}_{MAX} \rvert$ [m/s]	8.40×10^{-2}	1.14×10^{-8}	1.72×10^{-1}	6.74×10^{-9}

4.5 Numerical tests for droplets adhering to walls

Droplets on solid surfaces were simulated to check the occurrence of spurious currents due to implementation of contact angle. Droplets were initialized on the solid surface in such a manner that the initial angle between the gas–liquid interface and the solid surface at the point of contact was the same as the given contact angle. Hence the droplet was initialized at its equilibrium position.

Table 4.4 Errors for the droplet initialized at its equilibrium position; R = 10 μm

Curvature	κ_{CSF}			κ_{HF}		
Contact angle	60°	90°	120°	60°	90°	120°
$\lvert \boldsymbol{V}_{MAX} \rvert$ [m/s]	6.56×10^{-2}	9.88×10^{-2}	4.59×10^{-2}	5.28×10^{-9}	5.72×10^{-9}	1.71×10^{-8}

Table 4.5 Errors for the droplet initialized at its equilibrium position; R = 0.1 μm

Curvature	κ_{CSF}			κ_{HF}		
Contact angle	60°	90°	120°	60°	90°	120°
$\lvert \boldsymbol{V}_{MAX} \rvert$ [m/s]	9.86×10^{-2}	1.09×10^{-1}	1.06×10^{-1}	9.17×10^{-9}	8.12×10^{-9}	6.60×10^{-9}

Simulations were carried out for droplets of R = 10 μm and 0.1 μm. Since $\boldsymbol{N}_{ALE}$ gave much larger errors than $\boldsymbol{N}_{BFA}$, only $\boldsymbol{N}_{BFA}$ was used. The resolution was fixed at R/Δ = 20 and 100×70 mesh was used. Three values of Φ, *i.e.* 60°, 90° and 120°, were tested. The spurious currents for Φ = 60° and 120° for droplets of R = 10 μm and 0.1 μm are shown in Figs. 4.8 and 4.9, respectively. Tables 4.4 and 4.5 show $\lvert \boldsymbol{V}_{MAX} \rvert$. The errors for CSF and HF were of the same order compared with their respective cases of static circular droplets in Section 4.4. Hence the implementation of the contact angle does not cause any extra errors. This result suggests that κ_{HF} should be used for accurate predictions.

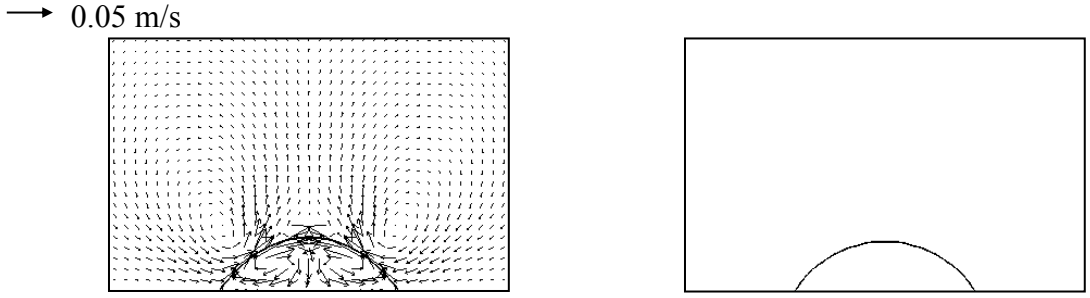

(a) κ_{CSF} , $\Phi = 60°$ (b) κ_{HF} , $\Phi = 60°$

(c) κ_{CSF} , $\Phi = 120°$ (d) κ_{HF} , $\Phi = 120°$

Fig. 4.8 Spurious currents for 10 μm droplet initialized at its equilibrium position

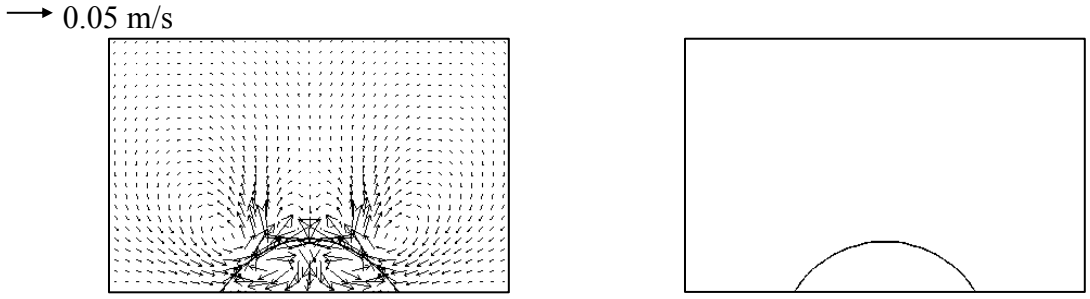

(a) κ_{CSF} , $\Phi = 60°$ (b) κ_{HF} , $\Phi = 60°$

(c) κ_{CSF} , $\Phi = 120°$ (d) κ_{HF} , $\Phi = 120°$

Fig. 4.9 Spurious currents for 0.1 μm droplet initialized at its equilibrium position

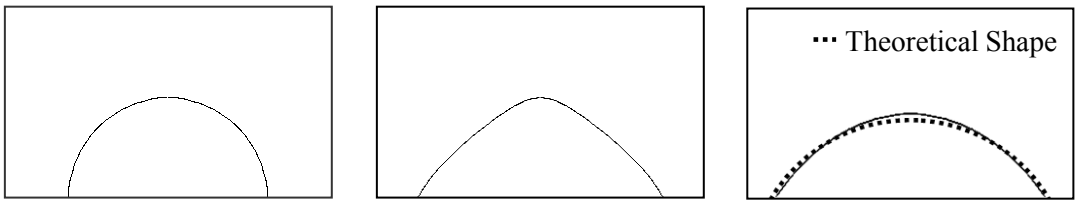

(a) κ_{CSF}, Time = 0 s (b) κ_{CSF}, Time = 0.02 ms (c) κ_{CSF}, Time = 0.2 ms

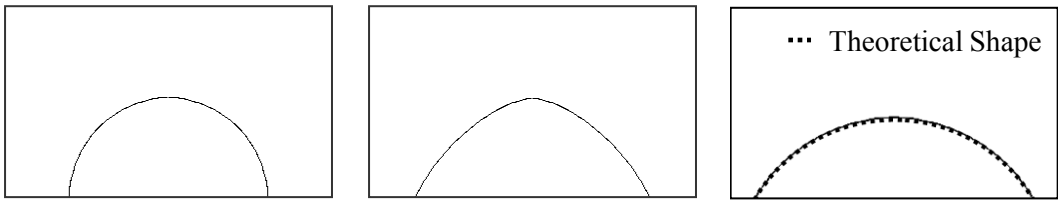

(d) κ_{HF}, Time = 0 s (e) κ_{HF}, Time = 0.02 ms (f) κ_{HF}, Time = 0.2 ms

Fig. 4.10 Droplet motion with contact angle of 60° (R = 10 μm)

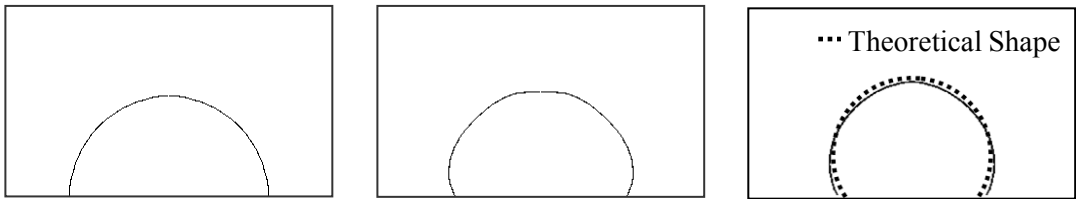

(a) κ_{CSF}, Time = 0 s (b) κ_{CSF}, Time = 0.02 ms (c) κ_{CSF}, Time = 0.2 ms

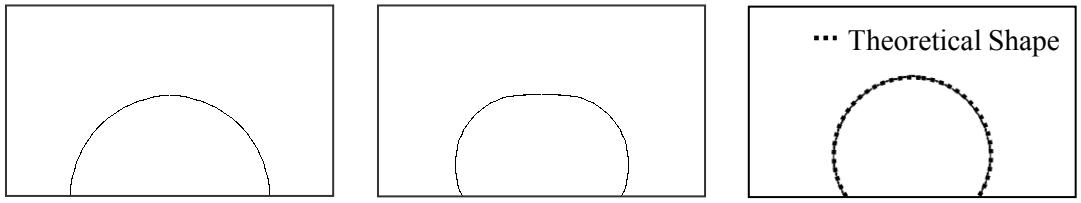

(d) κ_{HF}, Time = 0 s (e) κ_{HF}, Time = 0.02 ms (f) κ_{HF}, Time = 0.2 ms

Fig. 4.11 Droplet motion with contact angle of 120° (R = 10 μm)

Next, the motion of semi-circular droplets with radius 10 μm and 0.1 μm over a solid surface due to the contact line motion was computed to check the spurious currents after the droplets reached their equilibrium state. The results obtained using CSF and HF were compared. The motions of droplet of R = 10 μm at Φ = 60° and 120° is shown in Figs. 4.10 and 4.11, respectively. The droplet shapes in the equilibrium state for R = 0.1 μm are

shown in Figs. 4.12 and 4.13. The theoretical interface shape is represented by the dotted lines. The height function accurately predicts the equilibrium shape while there is some deviation in the case of CSF. The $|\boldsymbol{V}_{MAX}|$ are summarized in Tables 4.6 and 4.7. The velocities for both CSF and HF settle down to the same order of the spurious currents as compared to their respective cases of the static droplet in equilibrium over a solid surface.

Table 4.6 Errors for semi-circular droplet at different contact angles, R = 10 μm

Curvature	κ_{CSF}		K_{HF}	
Contact angle	60°	120°	60°	120°
$\|\boldsymbol{V}_{MAX}\|$ [m/s]	3.20×10^{-2}	6.68×10^{-2}	3.05×10^{-8}	8.39×10^{-8}

Table 4.7 Errors for semi-circular droplet at different contact angles, R = 0.1 μm

Curvature	κ_{CSF}		κ_{HF}	
Contact angle	60°	120°	60°	120°
$\|\boldsymbol{V}_{MAX}\|$ [m/s]	1.67×10^{-1}	5.58×10^{-2}	5.42×10^{-8}	6.09×10^{-8}

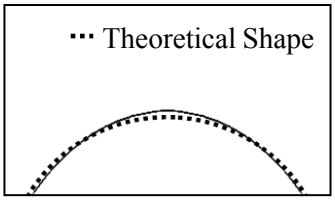

(a) κ_{CSF}, Time = 0.2 μs

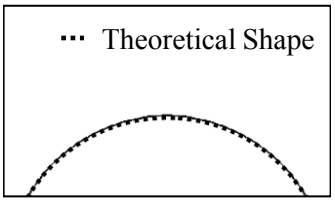

(b) κ_{HF}, Time = 0.2 μs

Fig. 4.12 Droplet motion with contact angle of 60° (R = 0.1 μm)

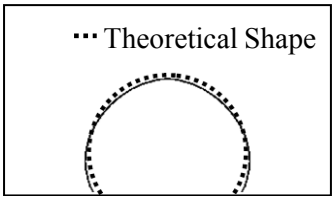

(a) κ_{CSF}, Time = 0.2 μs

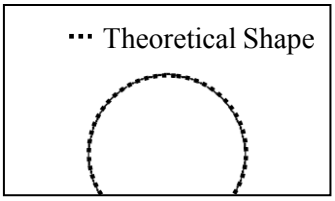

(b) κ_{HF}, Time = 0.2 μs

Fig. 4.13 Droplet motion with contact angle of 120° (R = 0.1 μm)

The above simulations have demonstrated that the combination of $\boldsymbol{N}_{BFA}$ and κ_{HF} is the most accurate not only for predicting buoyant droplets but also for predicting droplets on a solid surface.

4.6 Wetting of a solid plate by drops

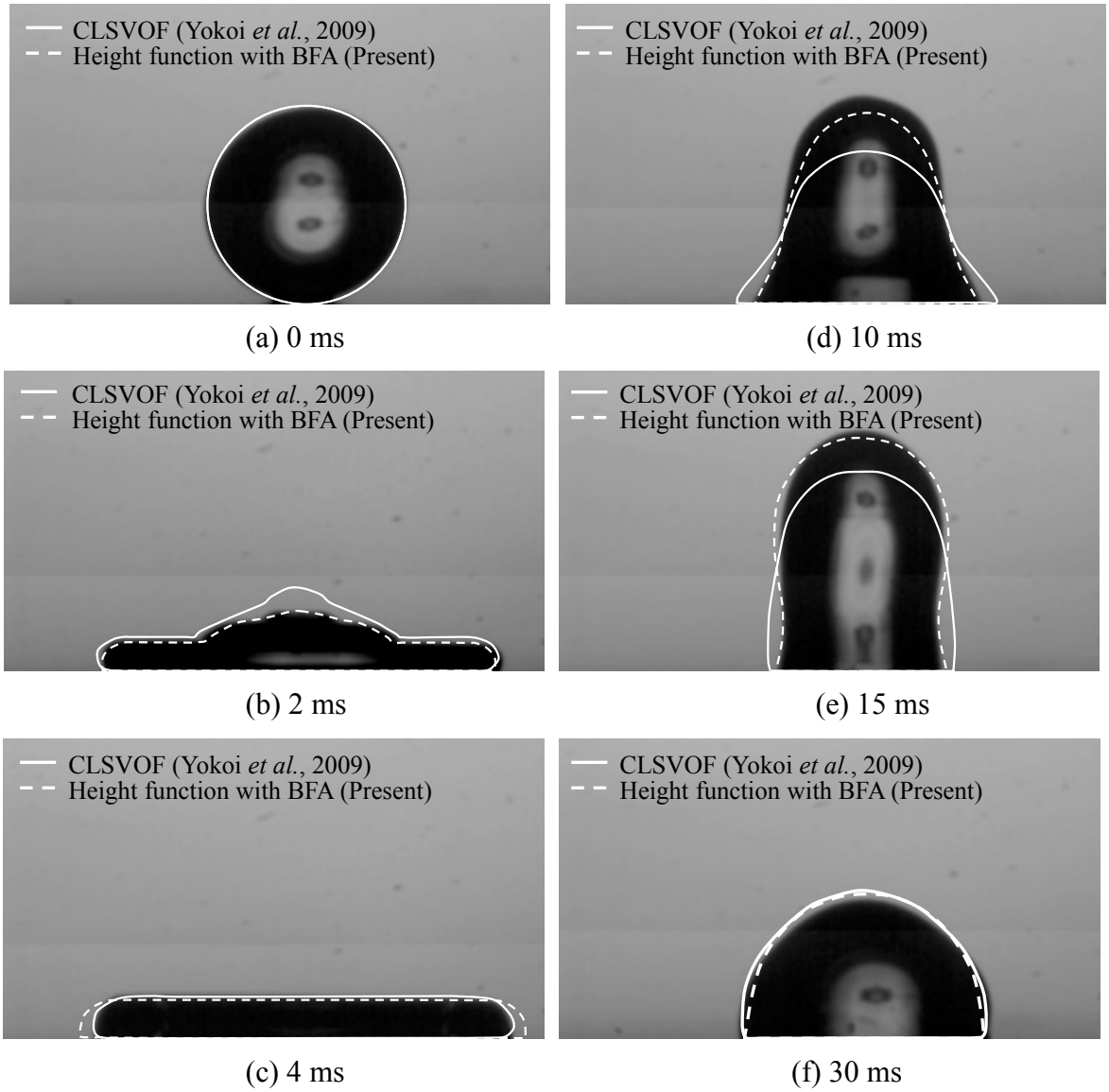

Fig. 4.14 Comparison between predicted and measured drop motion (Yokoi *et al.*, 2009)

First, the falling drop experiment for a clean water drop conducted by Yokoi *et al*. (2009) was simulated with the surface tension force calculated from the combinations of $\boldsymbol{N}_{BFA}$ with κ_{HF} and $\boldsymbol{N}_{ALE}$ with κ_{CSF}. The simulation conditions were kept the same as those described in Section 2.5. The implementation of height function in two-dimensional axisymmetric coordinates is carried out following the method proposed by Ferdowsi (2012). It is explained in Appendix A.

The predicted and measured drop motions are compared in Fig. 4.14. The drop shape predicted with the combination of HF and BFA in the wetting and dewetting phases is in better agreement with the experiment than CSF. The predicted wetting length and height of the drop as a function of time is shown in Figs. 4.15 and 4.16, respectively. The results are also compared with CLSVOF (Yokoi *et al.*, 2009). The prediction of drop height is slightly better than that obtained using CLSVOF. Hence, the combination of HF and BFA is able to predict the motion of the drop with the same degree of accuracy and less computational cost compared with CLSVOF.

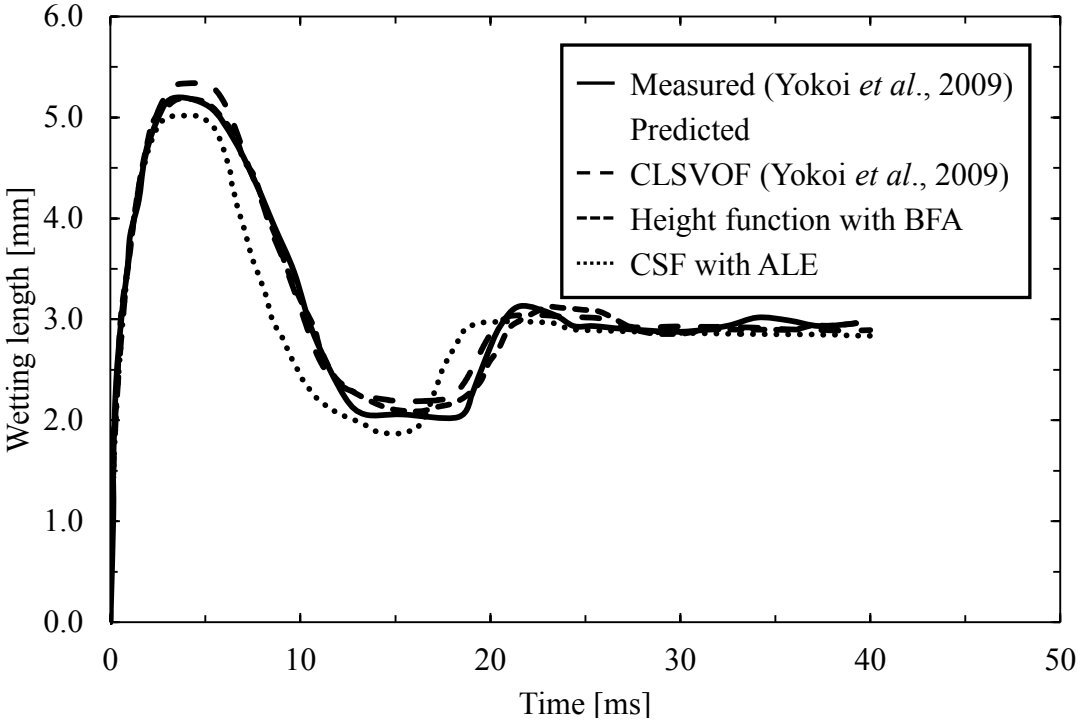

Fig. 4.15 Drop wetting length

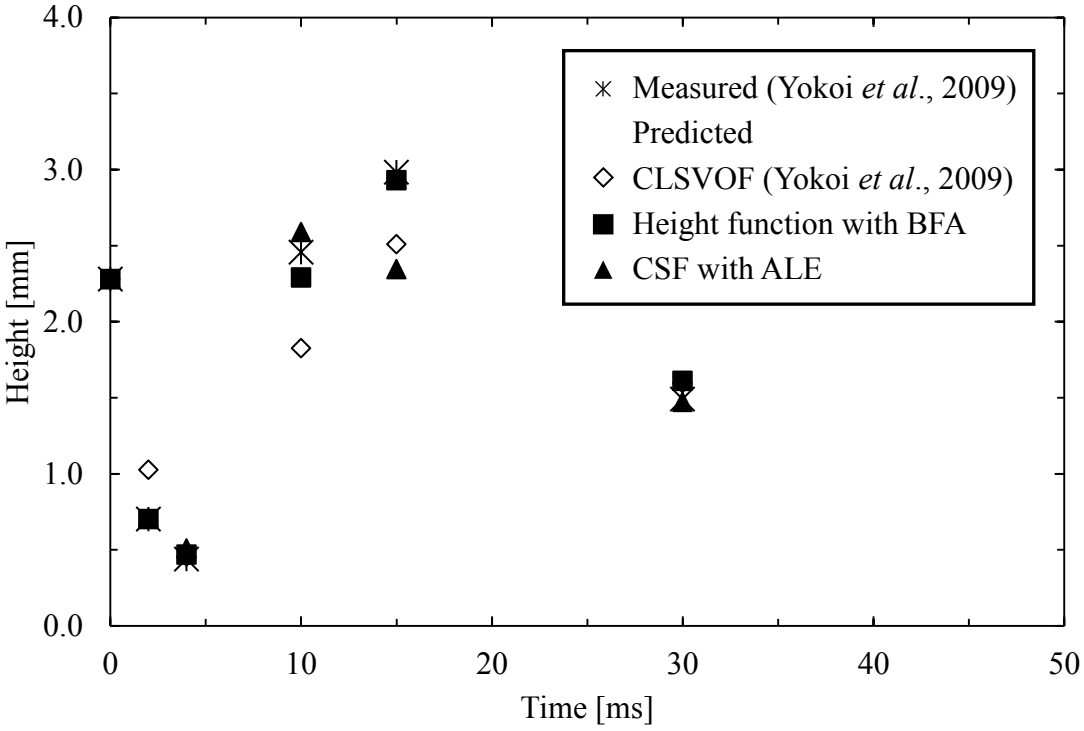

Fig. 4.16 Drop height

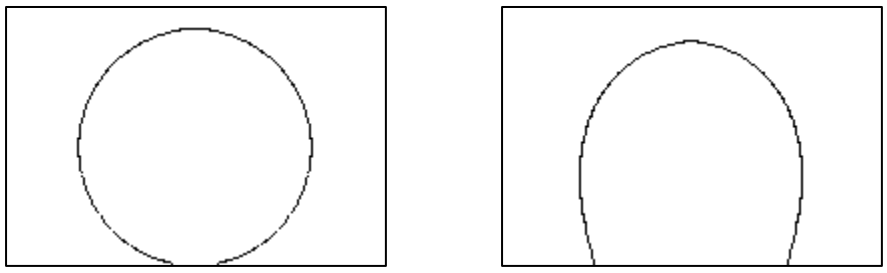

(a) Time = 0.0 μs

(b) Time = 0.005 μs

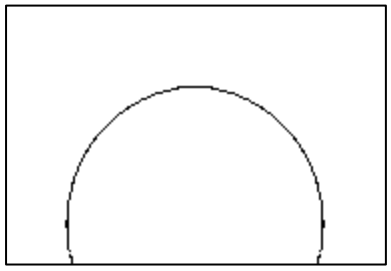

(c) Time = 0.01 μs

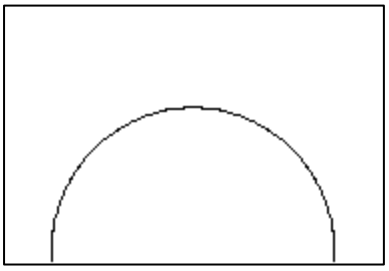

(d) Time = 1.0 μs

Fig. 4.17 Time evolution of droplet shape with HF

Finally, a droplet of R = 0.1 μm was simulated to examine the applicability of the selected method, $\boldsymbol{N}_{\mathrm{BFA}}$ and κ_{HF}, to the wetting of a solid plate by sub-micron meter droplets. A clean water droplet at 25 °C and 1 atm with an impact velocity of 1 m/s was used. A mesh of 100×100 was used with the resolution of R/Δ = 20. The time step was 2.5×10^{-13} s. The predicted droplet shape using HF with BFA is shown in Fig. 4.17. The droplet remains only in the wetting phase and shows no shape oscillations in contrast to the case of the larger drop. This can be attributed to the stronger surface tension force. That is to say, Weber number, *We*,

$$We = \frac{2\rho V_{\mathrm{IM}}^2 R}{\sigma} \tag{4.25}$$

where V_{IM} is the impact velocity, for the 1.14 mm drop (Yokoi *et al*., 2009) and 0.1 μm drop was 31.67 and 0.0028, respectively. The large reduction in *We* resulted in the weakening of the oscilattory behaviour of the drops. The surface tension force calculation using the combination CSF and ALE was also tested for comparison.

The final droplet shape and the velocity vector field obtained by using CSF and HF is compared in Fig. 4.18. The spurious currents in CSF after the droplet reached the equilibrium shape remained much stronger than HF. The simulation was stopped when reaching the steady state, *i.e.* no shape change was attained. The order of the spurious currents in CSF became constant while those in HF were still reducing. The equilibrium contact angle was specified at 90° and HF was able to predict the equilibrium shape better as shown in Fig. 4.18(b). The contact angle at the stationary state was computed using the method proposed by Iwata *et al*. (2012). HF and CSF gave contact angles of 90.07° and 92.68°, respectively. Hence the errors in contact angle predicted using HF and CSF are 0.08% and 2.98%, respectively.

The run environment was Xeon x5650 (6 cores, Dual CPUs, 2.66 Ghz). The simulations were run for 2,000,000 time iterations. The calculation time taken for HF and CSF was 70.1 hours and 83.7 hours respectively. The higher errors in CSF required more iterations for the

Poisson equation for pressure correction to converge as compared to HF and as a result HF took 16.25% less time as compared to CSF to complete the simulation.

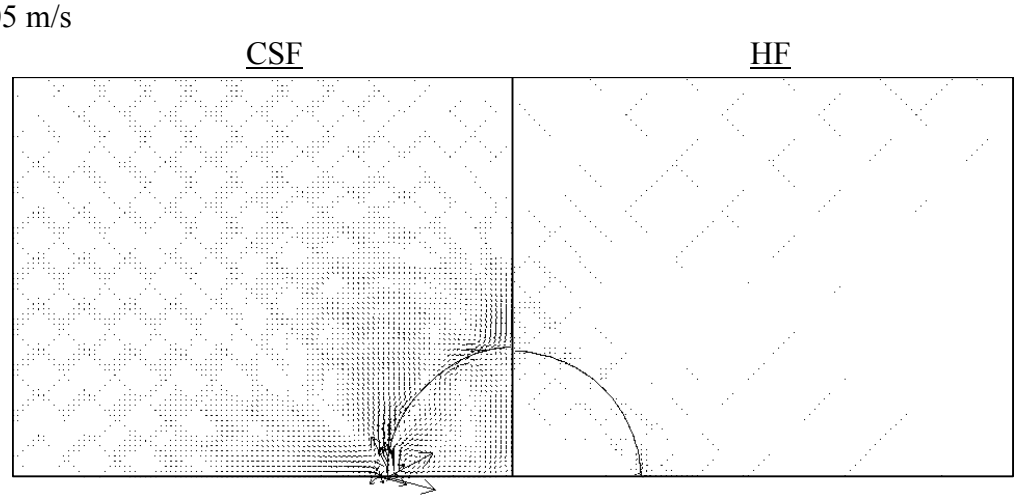

(a) Droplet shape and velocity vector field at Time = 1 μs

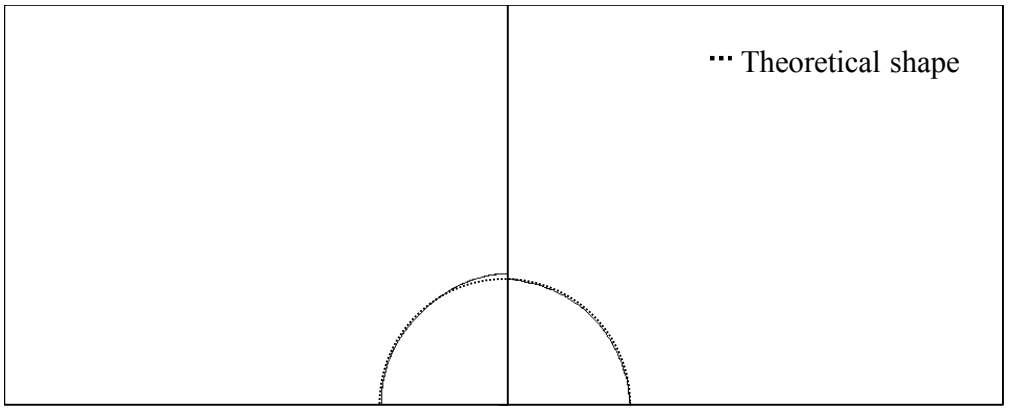

(b) Comparison of droplet shape with theoretical shape

Fig. 4.18 Comparison of the droplet shape and velocity vector field at Time = 1 μs (droplet at equilibrium)

4.7 Conclusions

Normal vector calculations based on the ALE like scheme and BFA and interface curvature calculations based on CSF and HF were compared to examine effects of the

numerical methods on the accuracy of the predicted motion of drops whose sizes range from mili to sub-micron meters. Simulations of a static circular drop of 1 mm in radius were carried out and the code was validated by confirming that the results were the same as to those in literature, *i.e.* the normal vector calculation based on BFA gave lower errors than the ALE like scheme, the interface curvature calculated using HF gave lower errors than CSF, and the errors were negligibly small when the theoretical value of curvature was used with BFA.

Simulations were carried out for smaller droplets ranging from a few micron to sub-micron meters to check the accuracy of the methods at such length scales. The applicability to coating processes was checked by carrying out simulation of wetting of a solid plate by droplets of mili-meter and sub-micron meter sizes. The following conclusions were obtained:

(1) Numerical errors in the pressure and velocity remained at the same order when the droplet size was reduced as well as when the contact angle was implemented. The combination of balanced-force algorithm with height function for surface tension force calculation was found to yield the lowest errors.

(2) The motion of a clean water drop of radius 1.14 mm on a solid plate was accurately predicted using the balanced-force algorithm with the height function and the model of dynamic contact angle proposed by Yokoi *et al*. (2009).

(3) The motion of a clean water droplet of radius 0.1 μm on a solid plate exhibited no oscillatory behaviour due to stronger surface tension forces, and HF predicted the contact angle in the equilibrium state better and caused smaller spurious currents than CSF.

References

Afkhami, S., Bussman, M., Height function-based contact angles for VOF simulations of contact line phenomenon, *International Journal Numerical Analysis and Modelling*, 2004, 1, pp. 1-18.

Afkhami, S., Bussman, M., Height functions for applying contact angles to 2D VOF simulations, *International Journal of Numerical Methods for Fluids*, 2007, 57, pp. 1023-1040.

Brackbill, J., Kothe, D., Zemach, C., A continuum method for modeling surface tension, *Journal of Computational Physics*, 1992, 100, pp. 335–354.

Cummins, S. J., Francois, M. M., Kothe, D. B., Estimating curvature from volume fractions, *Computers and Structures*, 2005, 83, pp. 425-434.

Ferdowsi, P. A., Combined numerical and thermodynamic analysis of drop imbibition into an axisymmetric open capillary, PhD thesis, Graduate Department of Mechanical & Industrial Engineering, University of Toronto.

Francois, M. M., Cummins, S. J., Dendy, E. D., Kothe, D. B., Sicilian, J. M., Williams, M. W., A balanced-force algorithm for continuous and sharp interfacial surface tension models within a volume tracking framework, *Journal of Computational Physics*, 2006, 213, pp. 141-173.

Hayashi, K., Tomiyama, A., Effects of numerical treatment of viscous and surface tension forces on predicted motion of interface, *Journal of Computational Multiphase Flows*, 2014, 6(2), pp. 111–126.

Hirt, C. W., Nichols, B. D., Volume of fluid (VOF) method for the dynamics of free boundaries, *Journal of Computational Physics*, 1981, 39, pp. 201-225.

Iwata, S., Suzuki, H., Mori, H., Measurement of surface tension and contact angle by analysis of force balance along a bubble/droplet surface, *Kagaku Kougaku Ronbunshu*, 2010, 36, 2, pp. 441-448.

Kunugi, T., Direct numerical algorithm for multiphase flow with free surfaces and interfaces, *Nihon Kikai Gakkai Ronbunshu*, 1997, 63, 609, pp. 1576 – 1584.

Maneri, C. C., Mendelson, H. D., The rise velocity of bubbles in tubes and rectangular channels as predicted by wave theory, *AIChE Journal*, 1968, 14, pp. 295-300.

Popinet, S., An accurate adaptive solver for surface-tension-driven interfacial flows, *Journal of Computational Physics*, 2009, 228, pp. 5838-5866.

Renardy, Y., Renardy, M., A parabolic reconstruction of surface tension for the volume-of-fluid method, *Journal of Computational Physics*, 2002, 183, pp. 400-421.

Rider, W. J., Kothe, D. B., Reconstructing volume tracking, *Journal of Computational Physics*, 1998, 141, pp. 112–152.

Sussman, M., Smerka, P., Osher, S., A level set approach for computing solutions to incompressible two-phase flow, *Journal of Computational Physics*, 1994, 114, pp. 146–159.

Takewaki, H., T.,Yabe, The Cubic-Interpolated Pseudo Particle (CIP) Method: Application to Nonlinear and Multi-Dimensional Hyperbolic Equations, , *Journal of Computational Physics*, 1987, 70, pp. 355-372.

Xiao, F., Honma, Y., Kono, T., A simple algebraic interface capturing scheme using hyperbolic tangent function, *International Journal for Numerical Methods in Fluids*, 2005, 48, pp. 1023–1040.

Yokoi, K, Vadillo , D., Hinch J., Hutchings, I., Numerical studies of the influence of the dynamic contact angle on a droplet impacting on a dry surface, *Physics of Fluids*, 2009, 21, 072102, pp.1-12.

Chapter 5

Effect of contamination on the dynamic behaviour of the gas-liquid interface

5.1 Background

The liquid used in the coating processes often consists of several components. For example, the ink used in inkjet printing is dissolved in a solvent to control the physical properties such as viscosity to ensure stable jetting from the nozzle. Also, the physical properties of the fluid such as surface tension are known to affect the formation of satellite droplets after injection from the nozzle (Wu *et al*., 2004(a) & (b); Jang *et al.*, 2009). These are undesirable since they affect the quality of printing by falling at locations other than the targeted ones and lead to formation of stains. The solute may act as a surface active agent to lower the surface tension and affect the quality of the process. Hence, the numerical method should be able to accurately predict the dynamic behaviour in the presence of a surfactant to be able to use it for design and optimization of coating processes. Most of the investigation of the dynamic wetting behaviour has been restricted to pure liquids (Sikalo *et al*., 2005, Yokoi *et al*., 2009).

In this chapter, the capability of the numerical method to predict the dynamic motion of gas-liquid interface in the presence of surfactant is investigated. Due to lack of data in the literature, falling contaminated droplet experiments were conducted for a wide range of

concentration. The contact angle was measured and fitted using the dynamic contact angle model proposed by Yokoi *et al.* (2009). Prediction of the wetting of a solid plate by a contaminated drop was carried out for several concentrations of the surfactant and compared with the experimental results. Finally, simulation of coating process was carried out to demonstrate the applicability of the proposed method to practical problems. The simulation of a typical coating process using an inkjet, beginning from injection of the droplet from a nozzle to its wetting behaviour on a solid surface, was carried out. The surfactant effect on the jetting from the nozzle was also investigated.

5.2 Experimental setup and method

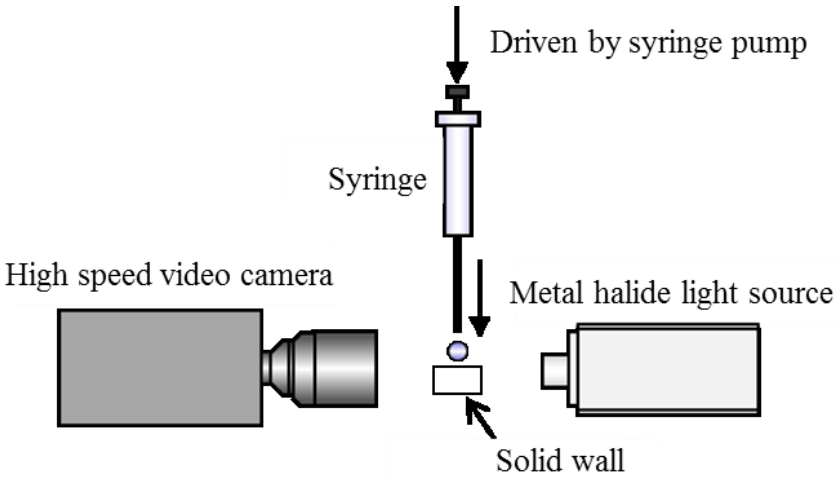

Fig. 5.1 Experimental setup

The experimental setup is shown in Fig. 5.1. The drop was created using a syringe pump (Isis Fusion touch 400) and made to fall on a solid plate made of methyl acrylate. A 50 ml syringe (Hamilton micro syringe 1000 series) was used along with a needle of inner and outer diameter of 0.15 mm and 0.52 mm, respectively. The drop behaviour from generation, motion in mid-air to the wetting of the solid surface was captured using a high speed video camera (Dantec Nanosense Mk-III, Micro-Nikon 60 mm, f/2.8D lens) with a metal halide light source as backlight. The exposure time and the focal length were set at 50 μs and 2.8

mm and the video was recorded at a frame rate of 2500 fps. The spatial resolution of the image captured at these conditions was 12.3 μm/pixel. Toritron X-100 was used as the surfactant and concentration was varied from 0 to 10 mmol/m^3. The temperature of the experimental environment and the liquid was maintained at 25±0.5 ºC. An image processing method, developed in-house, was used to extract the required data such as drop volume, contact angle etc. The drop injection was carried out very slowly as shown in Fig. 5.2 at the rate of 8.3×10^{-3} mm^3/s controlled by the syringe pump.

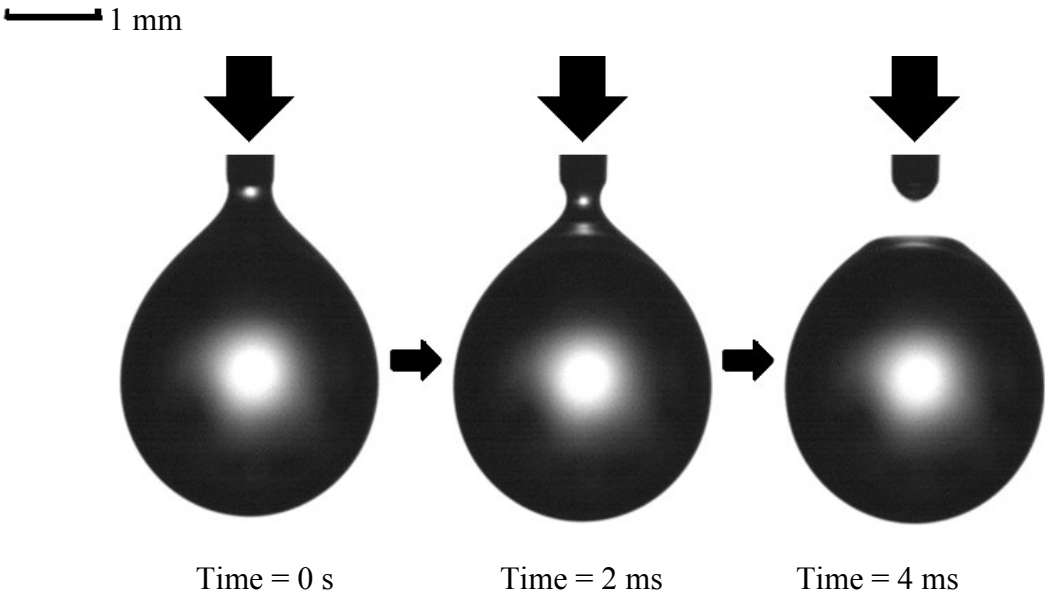

Fig. 5.2 Drop detachment from the needle

5.3 Image processing

The automatic extraction of data such as drop size, contact angle etc. from the image taken during the experiment using the image processing method was selected to reduce errors due to manual operation. The gas-liquid interface must be clearly captured to obtain the necessary data. The following processing of the image was carried out within the image processing method to detect the interface:

1. Generation of a background image from the cluster of images.
2. Removal of the background from the image.
3. Binarization of the image.

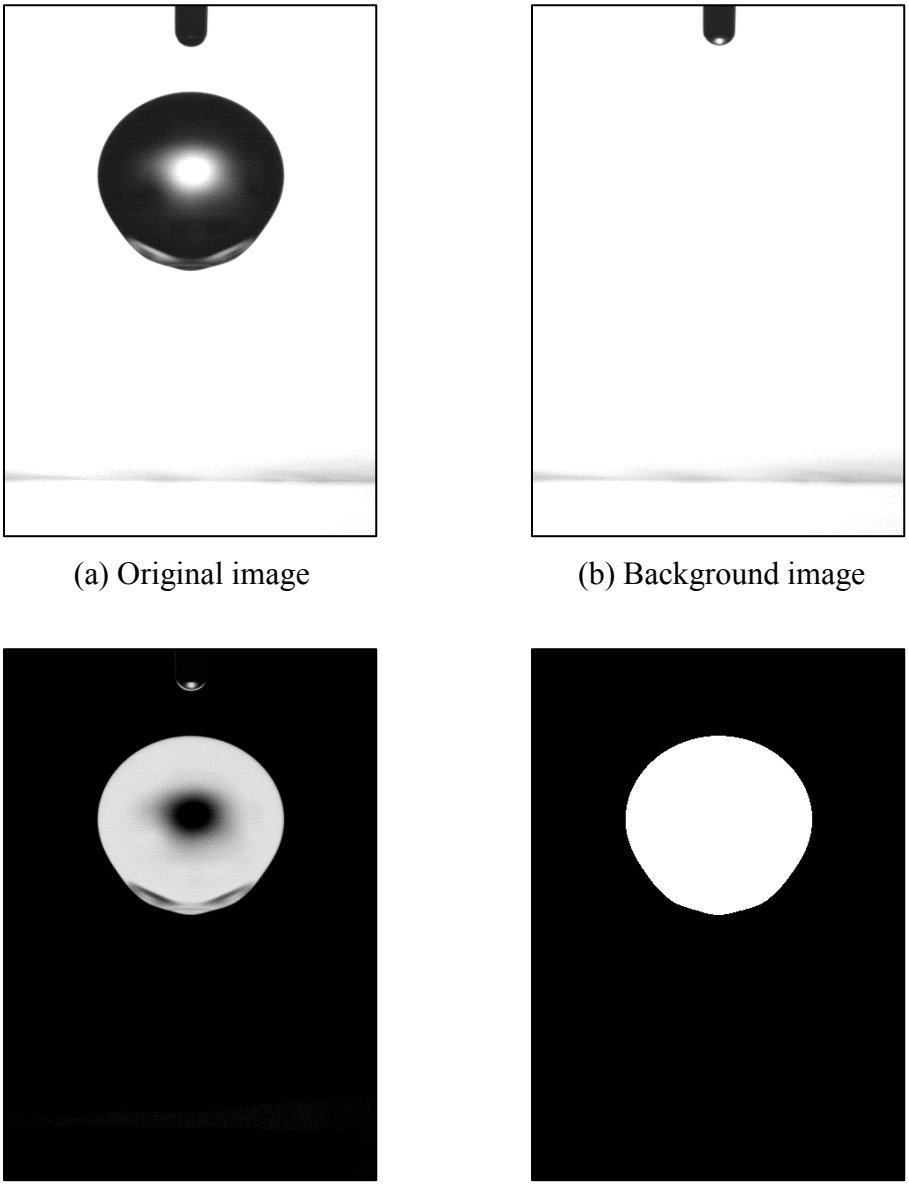

(a) Original image (b) Background image

(c) Image after removal of the background (d) Final processed image

Fig. 5.3 Image processing

The procedure has been summarized in Fig. 5.3. The accuracy of the data obtained from the method would depend on the quality of the captured image of the gas-liquid interface. The binarization was carried out based on a threshold value such that RGB values above the threshold were set to 255, *i.e.* white, and the values below it to 0, *i.e.* black. The resulting interface would depend on the threshold value. The threshold value was determined by a trial and error method. The interface was obtained using different threshold values and compared with the original image. The threshold value that gave an appropriate fit to the gas-liquid interface in the image interface was chosen as shown in Fig. 5.4(b).

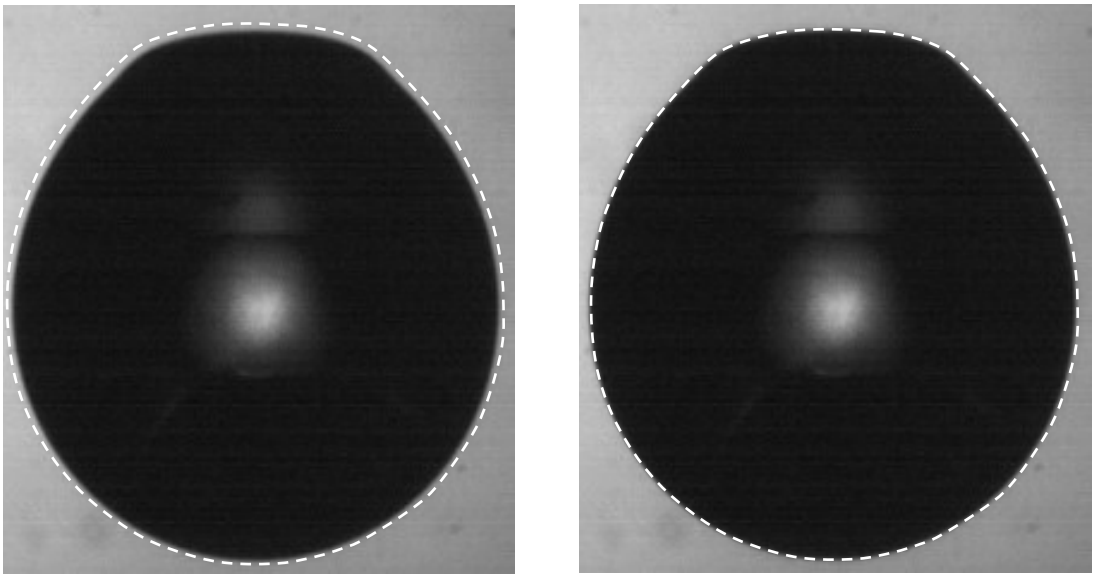

(a) Inappropriate threshold value (b) Appropriate threshold value

Fig. 5.4 Effect of threshold value on the interface detection

5.4 Experimental results

The surface tension in the presence of surfactant at adsorption-desorption equilibrium state can be computed using von Szyszkowski's equation (von Szyszkowski, 1908):

$$\sigma = \sigma_0 - RT\Gamma_\infty \ln\left(1 + La\right) \tag{5.1}$$

where σ_0 is the surface tension for pure water (=72 mN/m), R the gas constant, T the temperature of the fluid, Γ_∞ the saturation concentration of the surfactant at the gas-liquid interface, and *La* the Langmuir number defined by

$$La = \frac{c\chi}{\psi} \tag{5.2}$$

where c is the concentration of the surfactant at the interface, χ the adsorption coefficient, and ψ the desorption coefficient. The value of Γ_∞, χ, and ψ for Toritron X-100 is 2.9×10^{-6} mol/m^2, 50 m^3/mol·s, and 0.033 s^{-1} (Lin *et al.*, 1990), respectively. The surface coverage of the surfactant, *Se*, can be computed by

$$Se = \frac{La}{1+La} \tag{5.3}$$

The estimated value of surface tension from Eq. (5.1) and *Se* for several concentrations of the surfactant is shown in Table 5.1.

The above values of surface tension are correct only if the adsorption-desorption equilibrium state has been reached with the surface tension constant everywhere at the gas-liquid interface. This was verified by investigating the effect of the surfactant concentration on the drop size at the time of detachment from the needle tip. As the drop grows in size, the gravitational forces would become stronger and at a certain drop size the surface tension force would be balanced by the gravitational force. This can be considered to occur just before detachment as shown in Fig. 5.5 and the following relationship is established (Tate, 1864) at this instant if the surface tension is constant everywhere on the interface:

$$d \propto \left(\frac{D_T\sigma}{\rho g}\right)^{1/3} \tag{5.4}$$

where D_T is the diameter of the needle tip and d the equivalent drop diameter calculated from the volume of the drop, V, at the time of detachment from the syringe tip by

$$d = \left(\frac{6V}{\pi} \right)^{1/3} \tag{5.5}$$

where V is calculated in the image processing method. First, the centroid of the drop in the x-direction, X_G, is computed and this is assumed to be the axis of rotation. The volume of the drop can be then computed by

$$V = \sum_{y=a}^{b} \pi R_y^2 \Delta_{Res} \tag{5.6}$$

where Δ_{Res} is the spatial resolution of the image, and a and b the upper and lower limit of y, respectively, between which the volume calculation is carried out and R_y the radius of the drop at y. The procedure is shown in Fig. 5.6. The repeatability of the experiment was also checked by carrying out several runs for clean water and measuring the drop volume at the time of detachment. The calculated values of the drop volume were within ±5% of the average value as shown in Fig. 5.7.

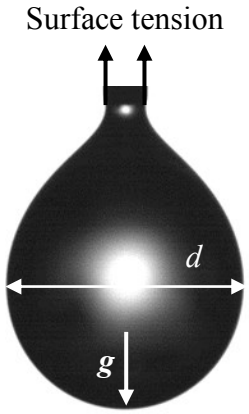

Fig. 5.5 Balance of surface tension and gravity

Table 5.1 Surface tension and *Se* for several concentrations of Toritron X-100

c [mmol/m^3]	*Se*	σ [mN/m]
0.5	0.43	68.0
1	0.60	65.4
3	0.82	59.7
6	0.90	55.4
8	0.92	53.5
10	0.94	52.0

Table 5.2 Model parameters for several concentrations of Toritron X-100

c [mmol/m^3]	Φ_E [°]	Φ_{mda} [°]	Φ_{mdr} [°]	l_a	l_r
0	77.81	108.56	39.81	2.82×10^{-8}	2.56×10^{-8}
0.5	74.48	109.27	47.29	2.95×10^{-8}	7.58×10^{-8}
1	74.36	108.97	49.09	2.55×10^{-8}	3.93×10^{-8}
3	72.28	107.06	48.84	2.89×10^{-8}	5.44×10^{-8}
6	70.89	105.77	36.87	4.27×10^{-8}	4.36×10^{-8}
8	74.66	102.32	39.81	9.08×10^{-8}	2.90×10^{-8}
10	70.92	103.25	36.87	6.20×10^{-8}	4.81×10^{-8}

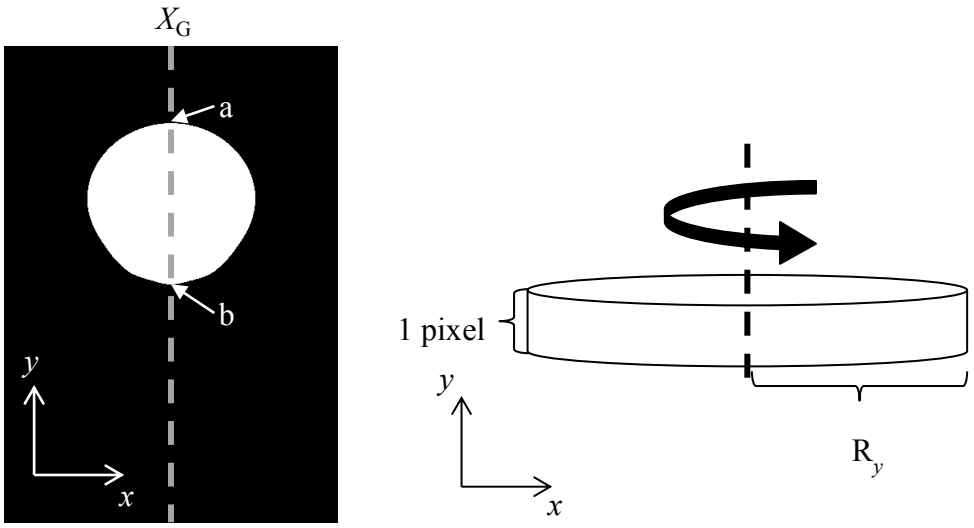

(a) Processed image (b) Volume calculation for one pixel

Fig. 5.6 Pictorial representation of volume calculation

The drop diameters *d* for several concentrations of Toritron X-100 were computed from image processing and were plotted against $\sigma^{1/3}$ in Fig. 5.8 to check whether the liquid had reached adsorption-desorption equilibrium state. The effect of surfactant concentration on drop size at the time of detachment is also shown in Fig. 5.9. The linear relationship between *d* and $\sigma^{1/3}$ was confirmed which shows that the surfactant adsorption at the interface had reached the equilibrium state and hence, the surface tension values were calculated using Eq. (5.1).

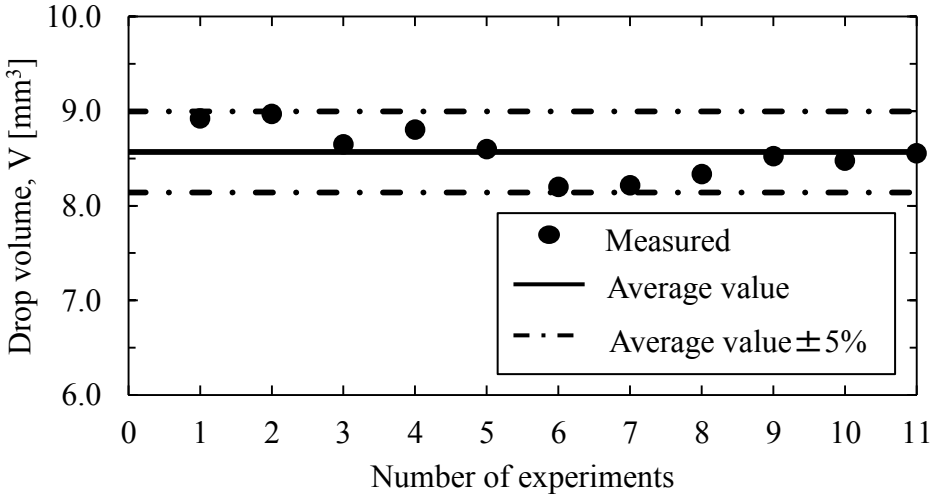

Fig. 5.7 Repeatability of the experiment

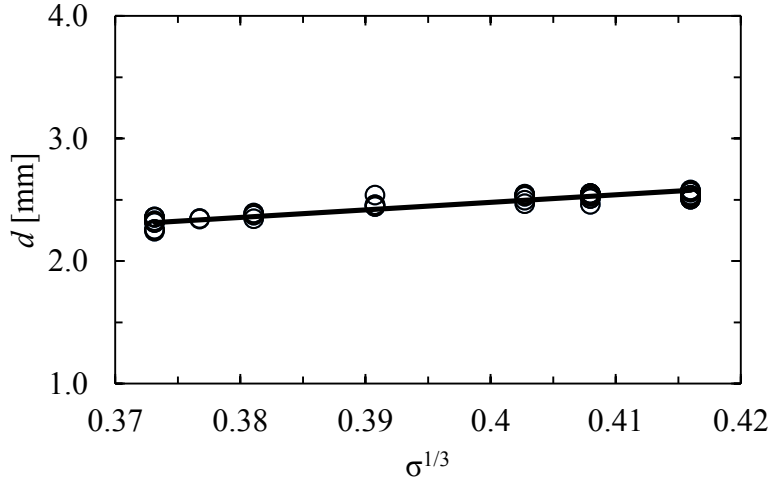

Fig. 5.8 Effect of surface tension on the drop size

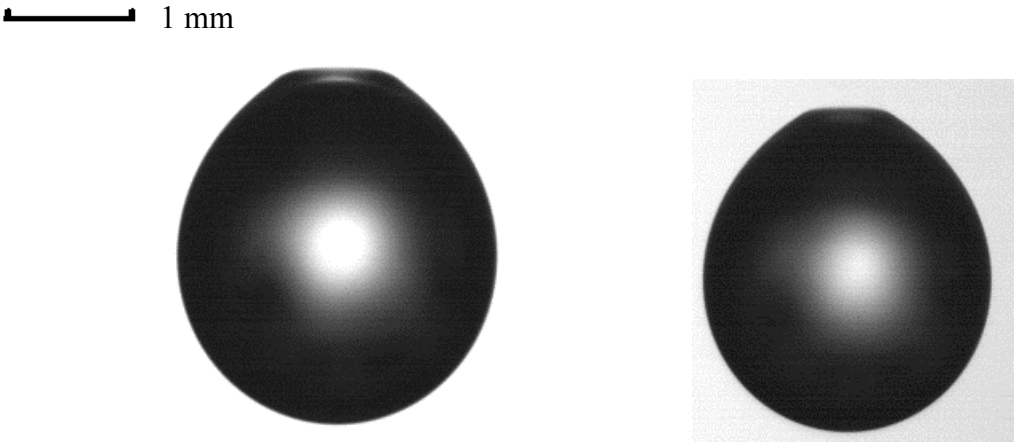

(a) Pure water, d=2.6 mm (b) c = 10 mmol/m^3, d=2.3 mm

Fig. 5.9 Drop size just after detachment from the needle

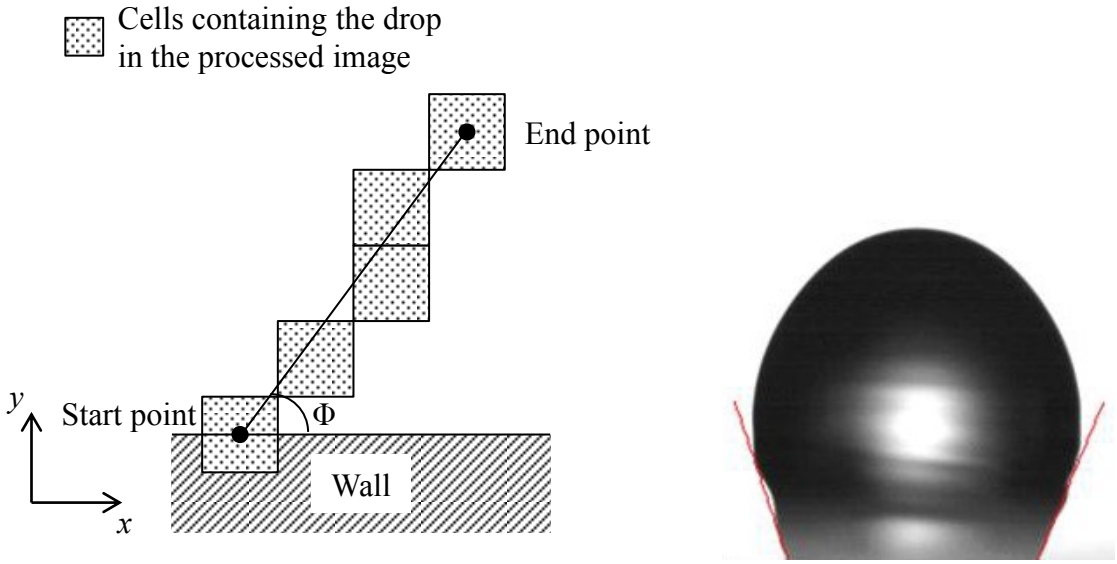

(a) Photographed image (b) Contact angle detection

Fig. 5.10 Contact angle measurement using image processing

Next, the contact angle for contaminated drops was evaluated using the dynamic contact angle model proposed by Yokoi *et al.* (2009). The contact angle was also measured using the image processing method. After obtaining the binarized image of the drop, the co-ordinates of the solid surface are inputted to search for the three phase contact point. The

three phase contact point is chosen as the start point as shown in Fig. 5.10(a). The end point is chosen as the interface cell at a distance of the specified number of pixels in the *x*-direction, 4 in the case of Fig. 5.10(a). The angle made by the line joining the start and the end point and the solid surface is the contact angle. The number of pixels in the *x*-direction used for selecting the end point was 12. The static contact angle measured using this number of pixels for pure water gave the least error when compared with the theoretical value. The model parameters for the dynamic contact angle model for several concentrations of Toritron X-100 are shown in Table 5.2. Figure 5.11 shows a comparison of the contact angle obtained experimentally and from the dynamic contact angle model for pure water and c = 10 mmol/m^3. Finally, a comparison of the transient behaviour of drop wetting length and height for c = 3, 6, and 10 mmol/m^3 are shown in Figs. 5.12 and 5.13, respectively.

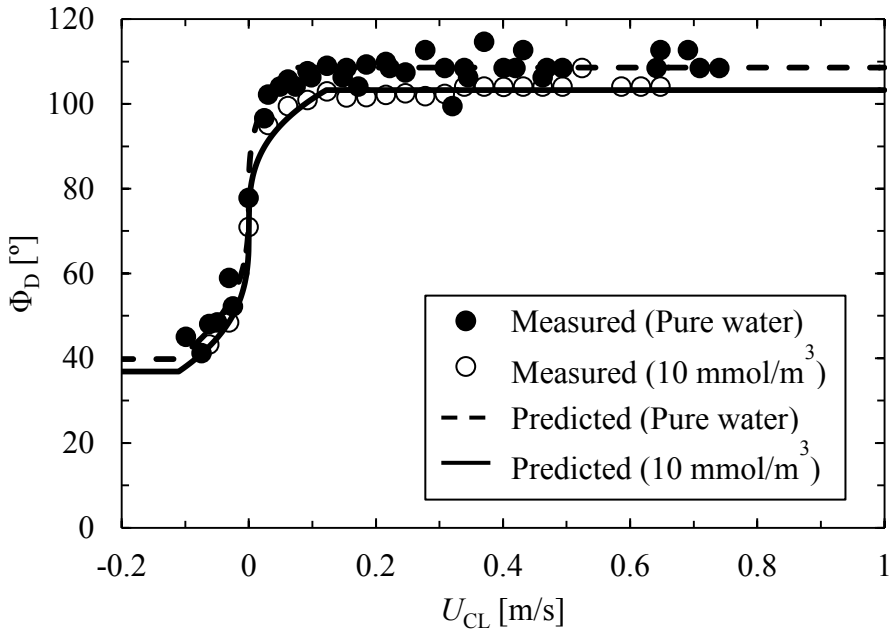

Fig. 5.11 Comparison between contact angle measured experimentally and calculated from the dynamic contact angle model

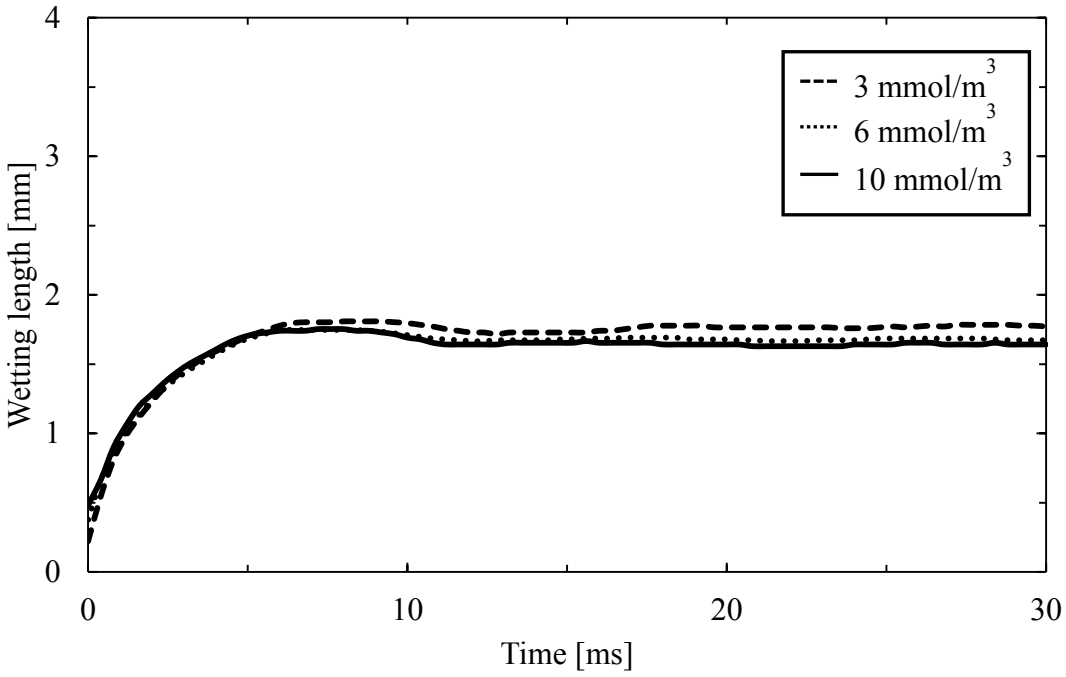

Fig. 5.12 Drop wetting length for several concentrations of Toritron X-100

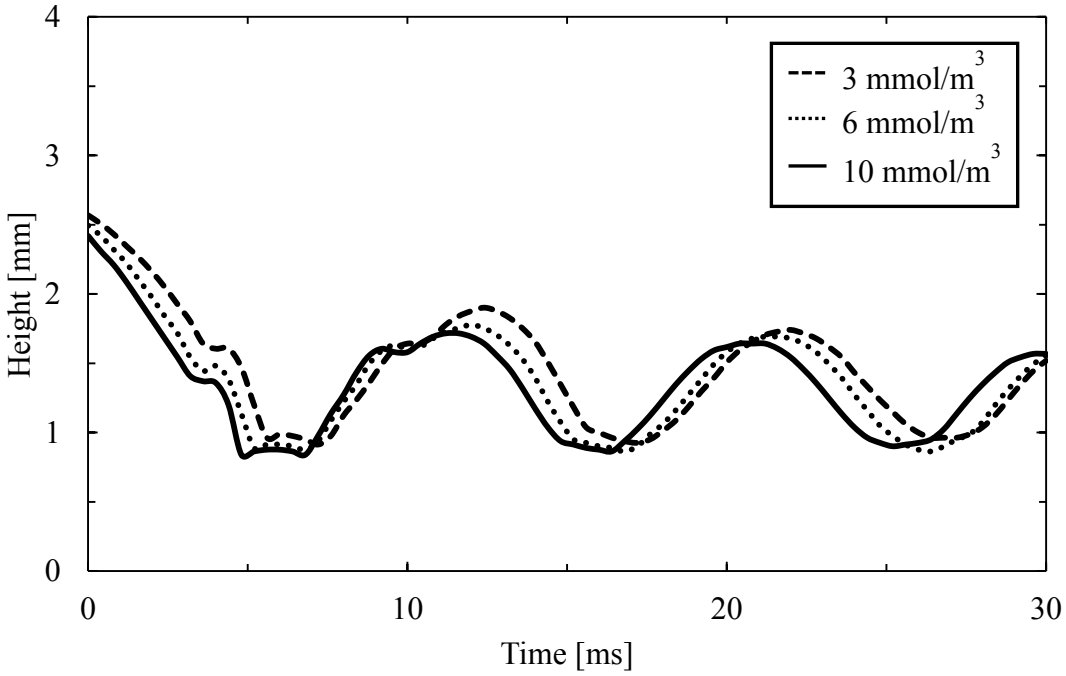

Fig. 5.13 Drop height for several concentrations of Toritron X-100

5.5 Wetting of a solid plate by contaminated drops

Prediction of the motion of a contaminated water drop on the solid plate using the dynamic contact angle model was carried out. Since the drop was injected slowly until it detached itself, a stationary drop with the shape at the time of detachment shown in Fig. 5.14(a) was used as the initial condition for the drop. The drop shape at the instant just after detachment from the needle tip is shown in Fig. 5.14(b). A 200×300 mesh was used. The cell size was uniform, $\Delta = 2.5\times10^{-5}$ m, and the time step was 1×10^{-6} s. The prediction of the wetting of a solid plate by a drop was carried out for surfactant concentrations of 3, 6, and 10 mmol/m^3. The distance of the drop from the solid plate, h, the height of the drop, l, and the width of the drop, w, for the three concentrations are shown in Table 5.3. Prediction was carried out using both the combinations of HF with BFA and CSF with ALE. The time taken by the drop to make contact with the plate in the experiment was 22.4 ms and was calculated to be 25 ms and 30 ms with the former and latter, respectively. Time evolutions of the wetting length for c = 3, 6, and 10 mmol/m^3 are shown in Figs. 5.15, 5.17, and 5.19, respectively while those of the drop height for c = 3, 6, and 10 mmol/m^3 are shown in Figs. 5.16, 5.18, and 5.20, respectively. Oscillations of drop height are better captured by HF with BFA than CSF with ALE where the height becomes constant after a certain time resulting in artificial dampening of the wetting behaviour. The prediction of the wetting length is also in better agreement for HF with BFA. The present results are in good agreement with the experiment. The wetting and dewetting motions are well predicted by only accounting for the surface tension reduction effects due to the surfactant and without solving the surfactant transport equation as was confirmed in our study.

Table 5.3 Initial condition for the drop

c [mmol/m^3]	w [mm]	h [mm]	l [mm]
3.00	2.42	2.77	2.59
6.00	2.29	3.01	2.64
10.00	2.22	3.04	2.52

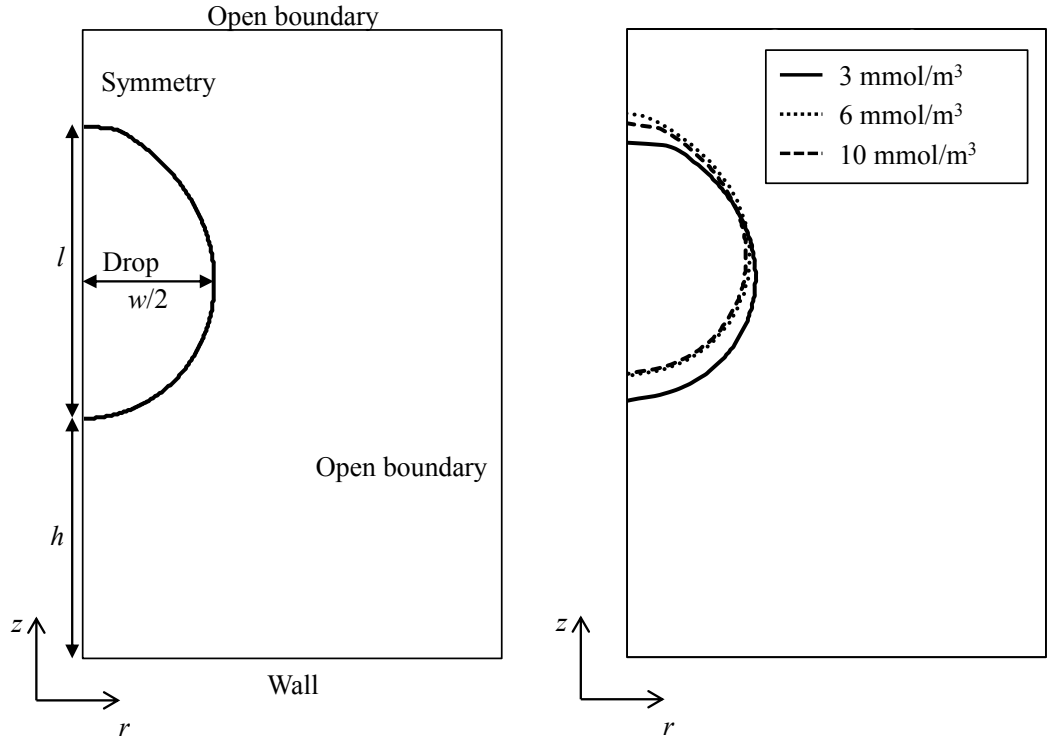

(a) Schematic of the initial condition (b) Drop shape just after detachment

Fig. 5.14 Initial condition

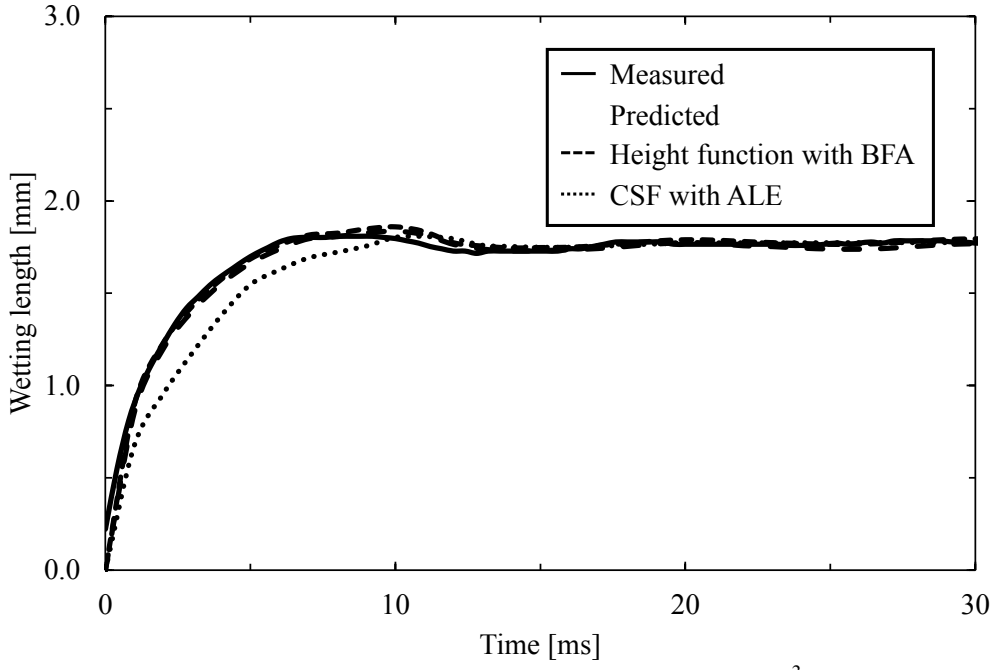

Fig. 5.15 Drop wetting length, c = 3 mmol/m^3

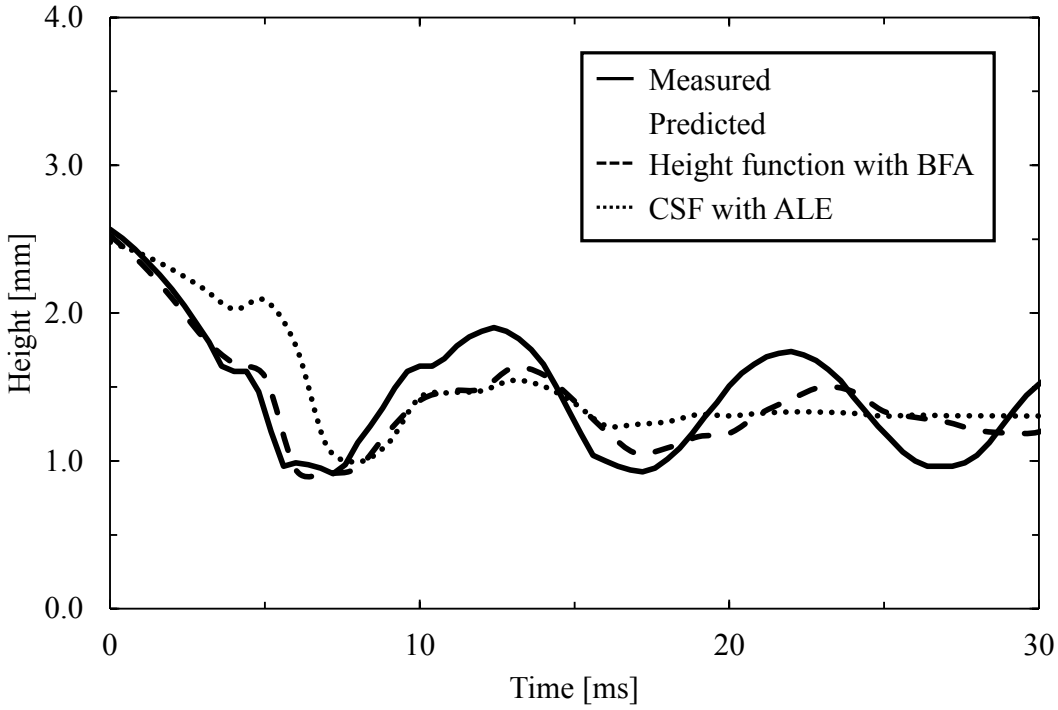

Fig. 5.16 Drop height, c = 3 mmol/m^3

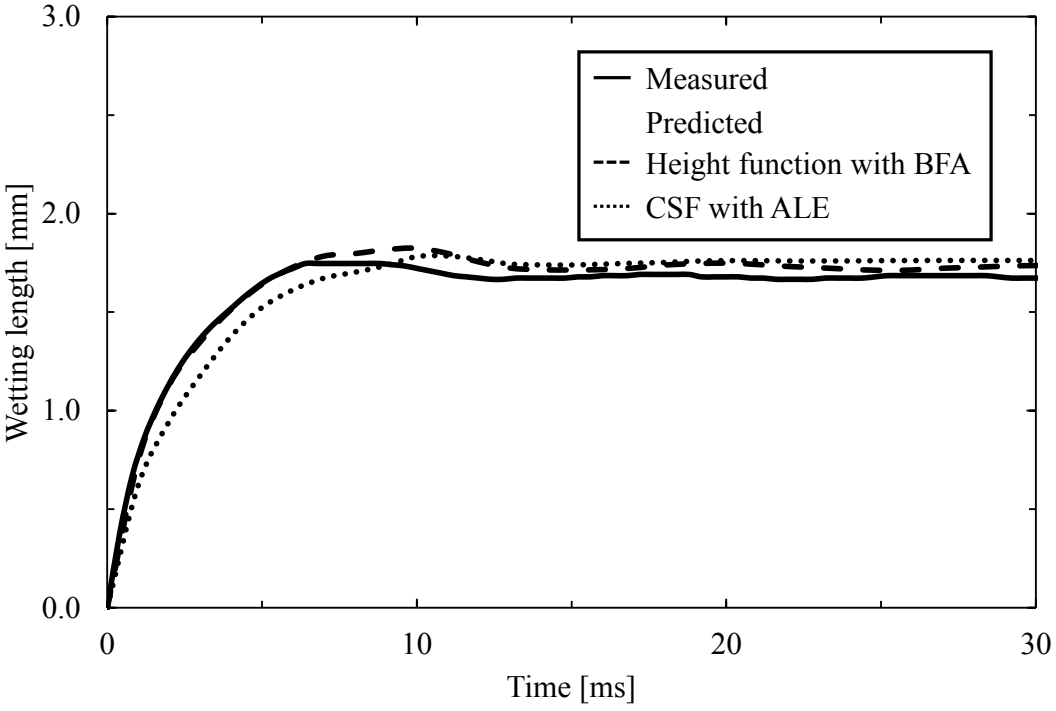

Fig. 5.17 Drop wetting length, c = 6 mmol/m^3

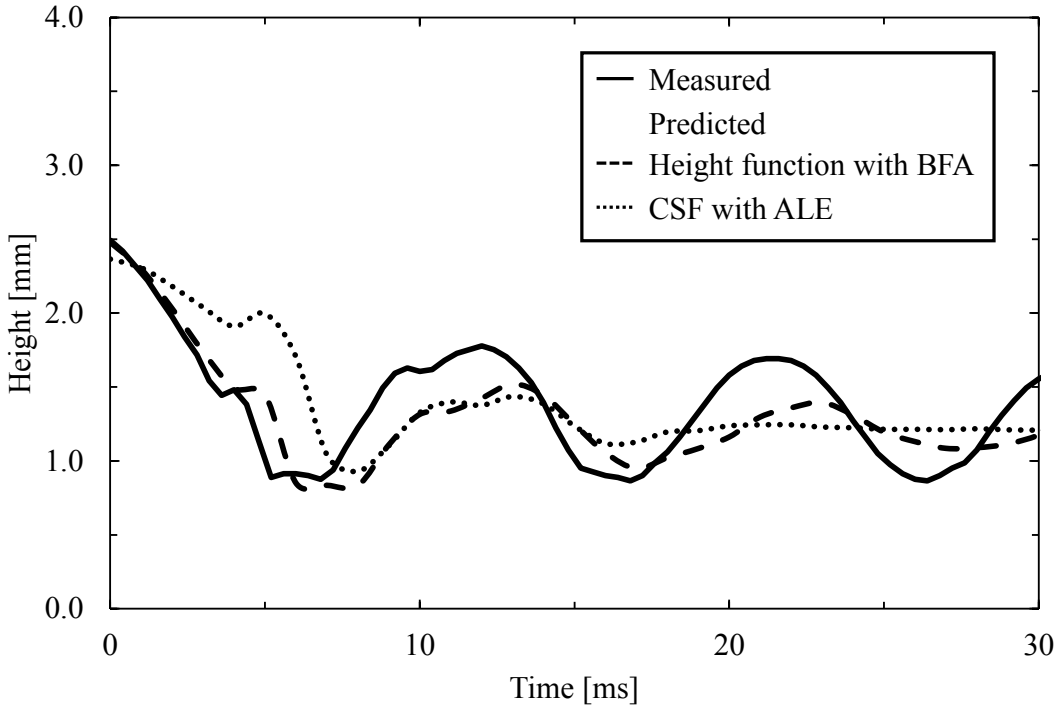

Fig. 5.18 Drop height, c = 6 mmol/m^3

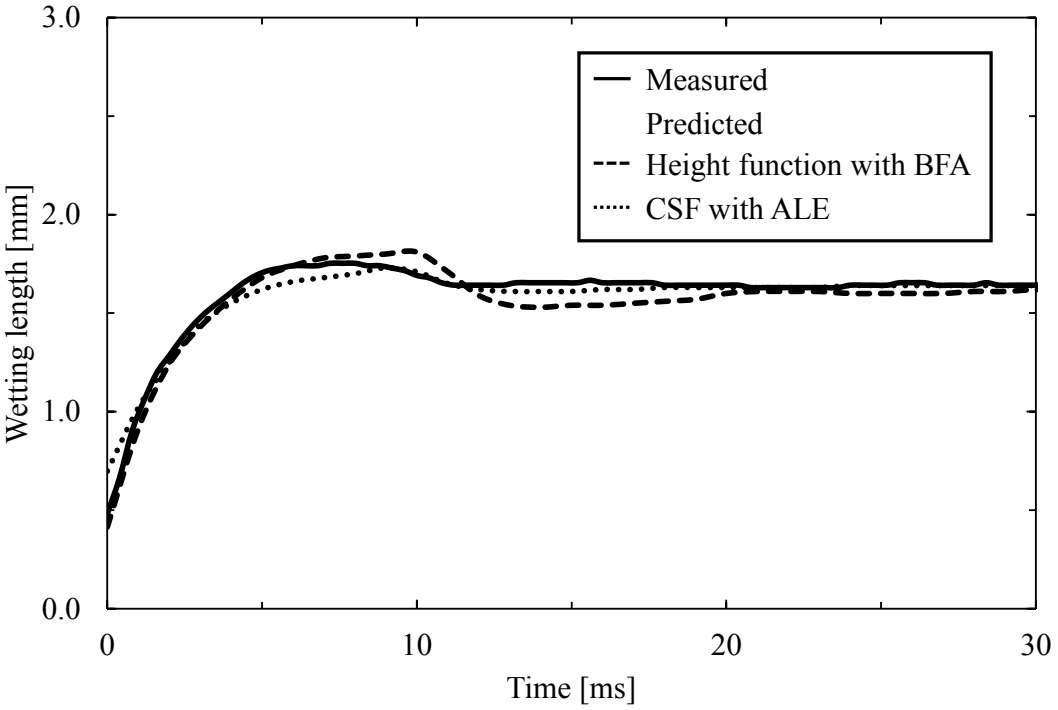

Fig. 5.19 Drop wetting length, c = 10 mmol/m^3

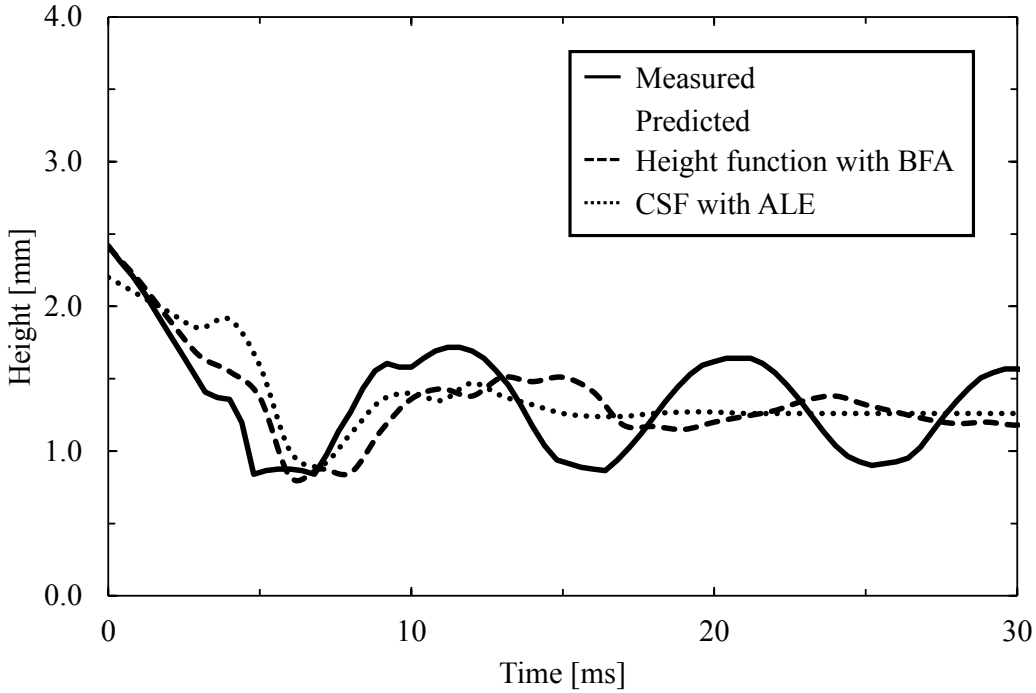

Fig. 5.20 Drop height, c = 10 mmol/m^3

5.6 Simulation of a coating process using an inkjet

Simulation of an inkjet coating process was carried out to demonstrate the applicability of the present method to industrial problems. The motion of tiny droplet starting from the injection of fluid from the nozzle to its wetting behaviour on a solid plate was predicted. First, a clean water droplet at 25 °C and 1 atm was simulated. A tapered inkjet head was used for injection as shown in Fig. 5.21(a). The outer diameter of the inkjet head was set at 50 μm while the inner diameter changed from 40 μm to 30 μm over a height of 10 μm. The mesh was 40×200. The cell size was uniform, $\Delta = 1.0\times10^{-6}$ m and the time step was 5×10^{-10} s. The fluid injection was carried out in a step wise manner for 1.25 μs at a velocity of 10 m/s. The dynamic contact angle model for a clean water droplet on a glass surface was used. The predicted droplet motion is shown in Fig. 5.21. The time required for the droplet to pinch off was 6 μs. The phenomena such as formation of droplet tail and its breakup to form satellite droplets have been captured.

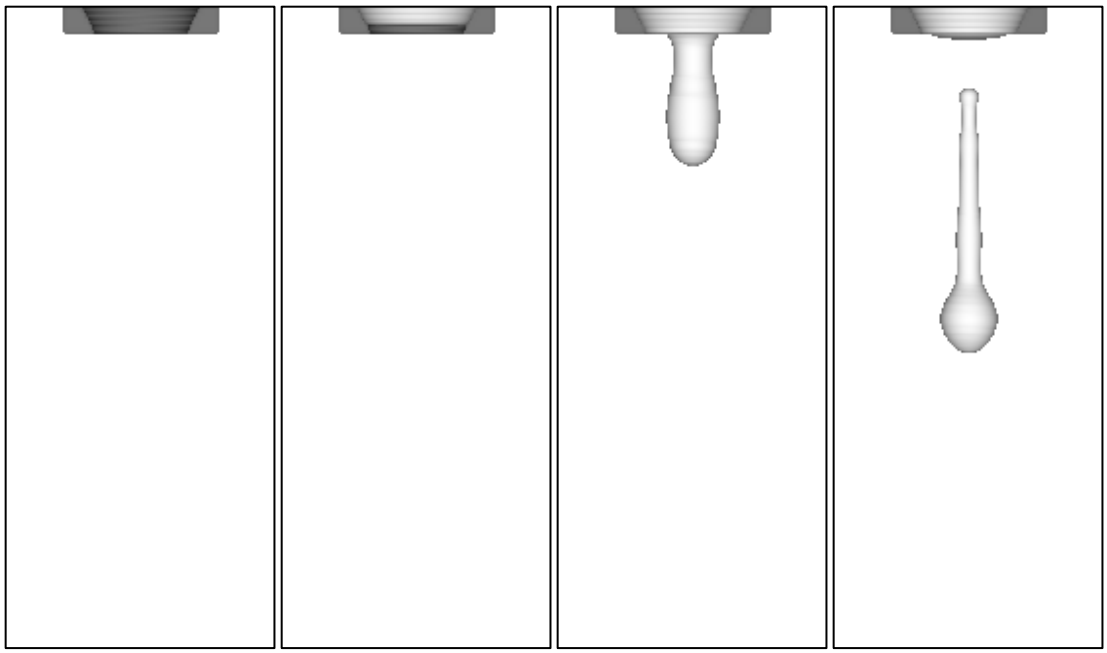

(a) t = 0 s (b) t = 2.5 μs (c) t = 5 μs (d) t = 7.5 μs

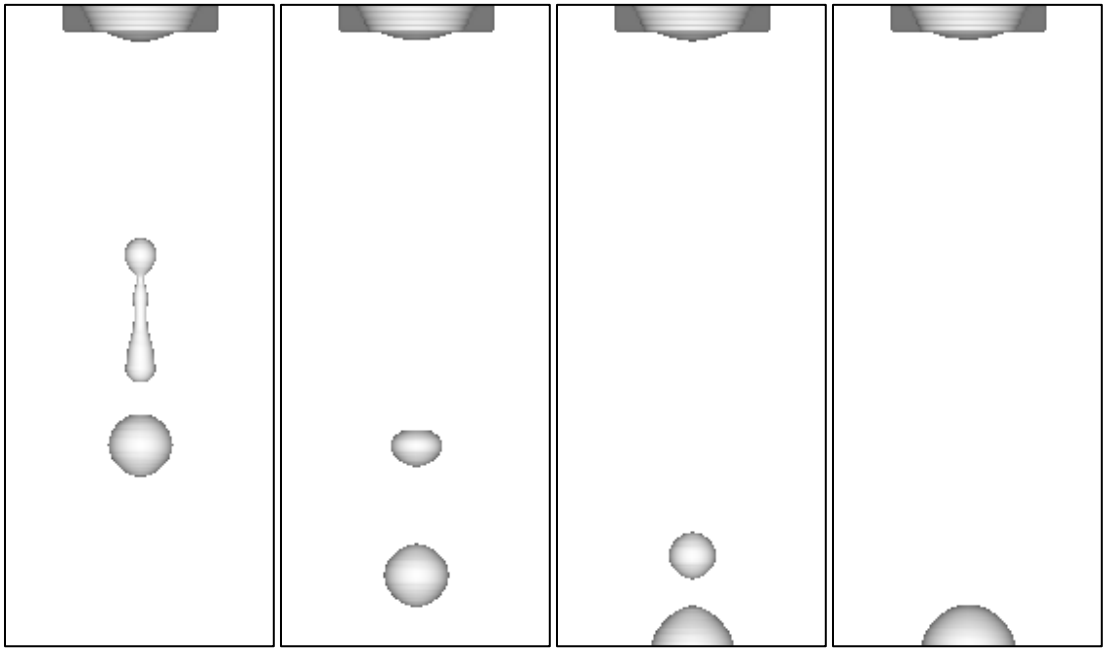

(e) t = 13.5 μs (f) t = 22.5 μs (g) t = 35 μs (h) t = 100 μs

Fig. 5.21 Droplet injection from a nozzle head (V_{Jet} = 10m/s, σ = 72 mN/m)

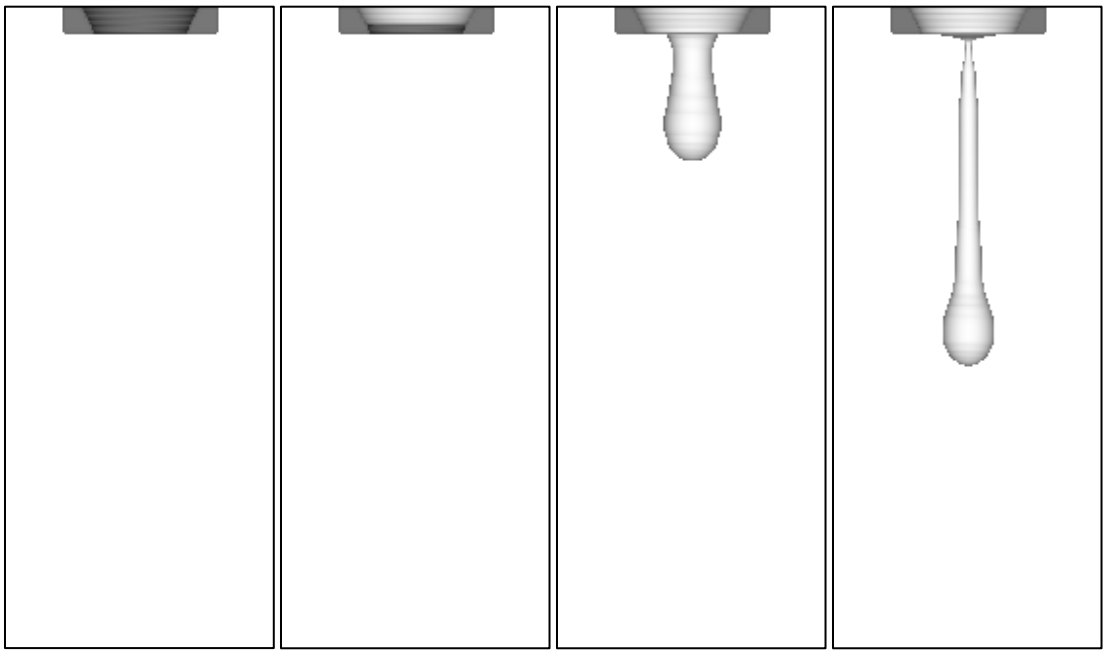

(a) t = 0 s (b) t = 2.5 μs (c) t = 5 μs (d) t = 7.5 μs

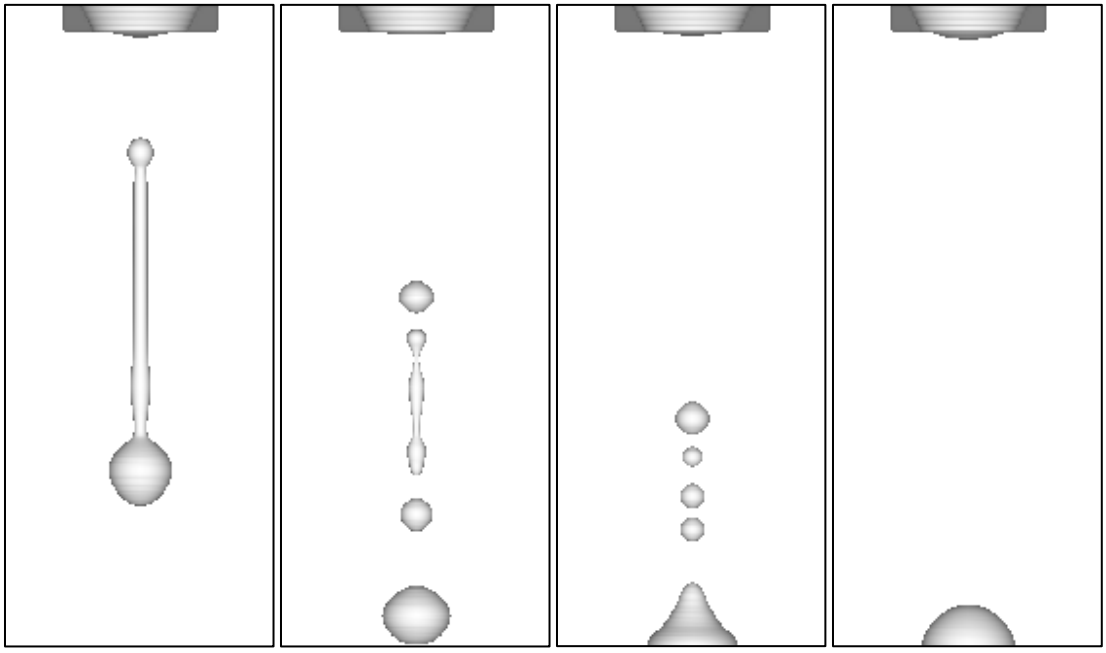

(e) t = 13.5 μs (f) t = 22.5 μs (g) t = 35 μs (h) t = 100 μs

Fig. 5.22 Droplet injection from a nozzle head (V_{Jet} = 10m/s, σ = 36 mN/m)

The effect of contamination on the formation of satellite was also investigated by reducing the surface tension to 36 mN/m while keeping the other physical properties the same as clean water. The results are shown in Fig. 5.22. The time required for the droplet to pinch off increased to 7.9 μs in the presence of contamination. The lowering of surface tension also caused formation of more satellite droplets as can be confirmed by comparing Figs. 5.21(g) and 5.22(g). In most of the coating methods based on inkjet printing, the surface to be coated is moved continuously to increase the speed of coating. An increase in satellite droplets is undesirable since they may fall at sites other than the target locations. The increase in pinch off time and number of satellite droplets with decrease in surface tension is consistent with the results reported in the literature (Wu *et al*. ,2004(a) & (b)).

The present method is being applied to industrial coating process to investigate the behaviour of droplets on different substrates under various conditions to obtain an insight into how various process conditions affect the coating behaviour. The scope of the method can be further broadened by incorporating the energy conservation equation and phase change to model evaporation of the solvent. The transport of the volume fraction with phase change is given by

$$\frac{D_K \alpha_K}{Dt} = -\frac{S}{\rho_K} \tag{5.7}$$

where S is the rate of mass loss per unit volume of phase K. A simple simulation of an evaporating neutrally buoyant drop of R = 1 mm without solving the flow equations was carried out to demonstrate the modelling of phase change. A 50×50 mesh was used and R/Δ was 10. The mass loss per unit area of the interface was set at 10 kg/m^2·s. The shape at different time instants is shown in Fig. 5.23. An artificial distortion in shape is noticed as the drop becomes smaller. The reason for this is the decrease in resolution since the mesh size was not being modified as the drop size decreased. Apart from this, challenges are present in the accurate modelling of the evaporation rate, S, which depends on parameters such as the local concetration of the solvent in the gas phase, temperature etc.

Implementation of grid refinement methods such as adaptive mesh refinement (AMR) and accurate modelling of evaporation rate can enable the present method to be applied to the investigation of droplet drying on a surface as well.

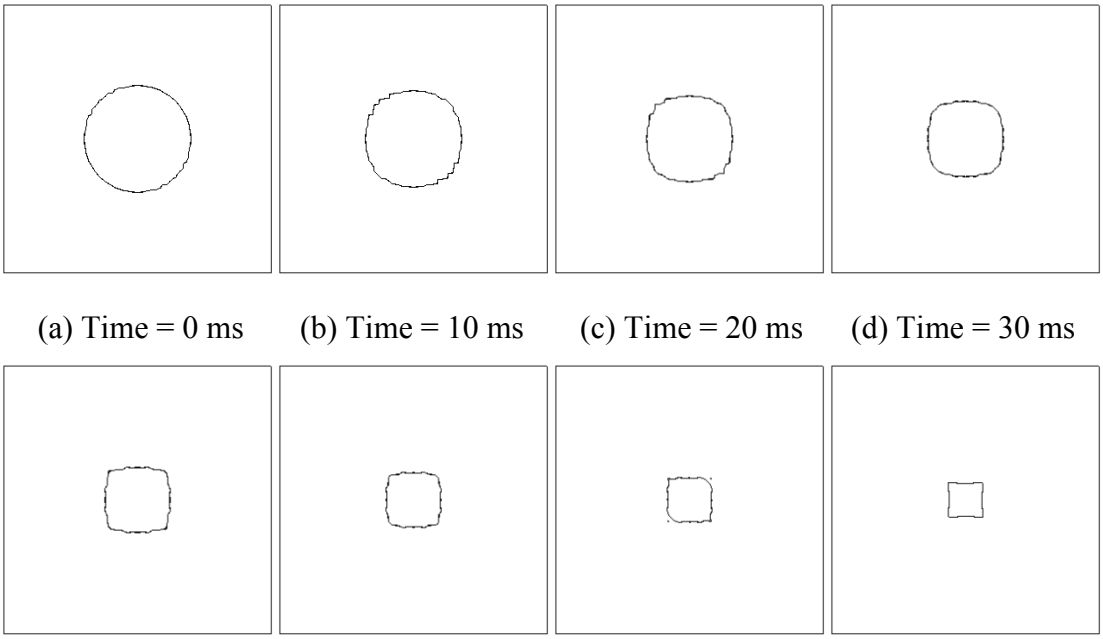

(a) Time = 0 ms (b) Time = 10 ms (c) Time = 20 ms (d) Time = 30 ms

(e) Time = 40 ms (f) Time = 50 ms (g) Time = 60 ms (h) Time = 70 ms

Fig. 5.23 Evaporation of neutrally buoyant drop

5.7 Conclusions

Falling drop experiments were carried out for water drops with several concentrations of surfactant to examine the effect of contamination on the motion of drops on a solid plate. The repeatability of the experiment was confirmed. The adsorption-desorption equilibrium of the surfactant on the interface was confirmed by checking the effect of surface tension on the drop size at the time of detachment from the needle tip. Hence, the surface tension at different concentrations of the surfactant was estimated using von Szyszkowski's equation

(von Szyszkowski, 1908). The contact angle was measured and modelled using the dynamic contact angle model proposed by Yokoi *et al.* (2009).

The wetting of a solid plate by contaminated drop for c = 3, 6, and 10 mmol/m^3 was predicted to check the accuracy of the present method. Finally, the simulation of a coating process using an inkjet was carried out to demonstrate the applicability to industrial problems. The following results were obtained:

(1) The presence of contamination caused a reduction in the contact angle.

(2) The motion of a contaminated water drop on a solid plate was accurately predicted using the balanced-force algorithm with the height function and the model of dynamic contact angle proposed by Yokoi *et al*. (2009).

(3) The reduction in surface tension caused an increase in the time required for the droplet to pinch-off and also increased the number of satellite droplets.

References

von Szyszkowski, B., Experimentelle studien über kapillare eigenschaften der wäßrigen lösungen von fettsäuren, *Zeitschrift für Physikalische Chemie*, 1908, 64, pp. 385-414.

Jang, D., Kim, D., Moon, J., Influence of fluid physical properties on ink-jet printability, *Langmuir*, 2009, 25, pp. 2629-2635.

Lin, S. Y., McKeigue, K., Maldarelli, C., Diffusion-controlled surfactant adsorption studied by pendant drop digitization, *AIChe Journal*, 1990, 36, pp. 1785-1795.

Sikalo, S., Wilhelm, H. D., Roisman, I. V., Jakirlic, S., Tropea, C., Dynamic contact angle of spreading droplets: Experiments and simulations, *Physics of Fluids*, 2005, 17, 6, 062103, pp. 1-13.

Tate, T., On the magnitude of a drop of liquid formed under different circumstances, *Philosophical Magazine*, 1864, Series 4, pp. 176-180.

Wu, H., Hwang, W., Lin, H., Development of a three-dimensional simulation system for micro-inkjet and its experimental verification, *Materials Science and Engineering*, 2004, 373, pp. 268-278.

Wu., H., Lin, H., Kuo, Y., Hwang, W., Simulation of droplet ejection for a piezoelectric inkjet printing device, *Materials Transcations*, 2004, 45, 3, pp. 893-899.

Yokoi, K, Vadillo , D., Hinch J., Hutchings, I., Numerical studies of the influence of the dynamic contact angle on a droplet impacting on a dry surface, *Physics of Fluids*, 2009, 21, 072102, pp.1-12.

Chapter 6

Conclusions

6.1 Conclusions

In this dissertation, a new numerical method was developed to predict the motion of gas-liquid interface in the presence of complicated solid geometries. The transport of the fluid phase is carried out using a new scheme based on the VOF method and an immersed boundary method is used to handle of the complex solid geometries. An efficient and accurate method was developed for practical applications involving gas-liquid interface of length scales ranging from mili to sub-micron meters without increasing the computational cost. The method is easy to extend to three-dimensional problems. The performance of the developed method was demonstrated by carrying out several numerical tests and simulations. The results were compared with existing numerical methods as well as experiments.

In chapter 2, a new VOF based method, THAINC, for transporting the gas-liquid interface was proposed. The reconstruction of the interface is based on a tangent hyperbolic function as proposed in THINC (Xiao *et al*., 2005). The tangent hyperbolic function in the present method is devised to be dependent on the inclination of the interface in contrast to THINC. This results in elimination of artificial wrinkling of the interface present in THINC. The proposed method does not need to geometrically reconstruct the interface configuration

in a computational cell as in PLIC-type methods. Owing to this feature, implementation of this method to three-dimensions is easier compared to the methods using geometric reconstruction. The method is also easy to program. Its ability to effectively represent the interface was checked by carrying out several advection tests. The proposed method has lower errors in the transported shape and the volume in the advection tests than THINC, THINC/WLIC, Donor-Acceptor, and 1st order upwind schemes. The accuracy of THAINC was investigated by comparing the simulation results of a rising bubble and wetting of a solid plate by a drop with those reported in the literature. The predicted motions of the gas-liquid interface in both cases were in good agreement with the experiments. THAINC is also able to capture the gas-liquid interface within two cells with good volume conservation. There is no overshooting or undershooting of the phase indicator function.

In chapter 3, a numerical method, THAINC-IB, for predicting the motion of gas–liquid interface in the presence of complex solid geometry in the flow domain was developed. The transport equations of the gas-liquid interface in the presence of solid phase in the computational cell were derived. The proposed method is a combination of THAINC and an immersed boundary method. The transport of the fluid phases is based on the THAINC whereas the immersed boundary method proposed by Fadlun *et al*. (2000) is adopted to deal with complicated solid geometries. Hence, it has all the properties of THAINC such as easiness in extension to three-dimensional problems and low computational costs.

The occurrence of errors in advection due to the presence of solid in computational cells was investigated by a horizontal and a diagonal advection of a fluid square between parallel solid walls. The errors in the transported shape and the volume using THAINC-IB were small. The proper implementation of the immersed boundary method was checked by simulating a single phase flow in the presence of staggered arrangement of cylindrical tubes. The calculated pressure drop across the bundle of cylindrical tubes for different Reynolds number were in good agreement with the values reported in the literature. The capability of THAINC-IB to handle two-phase flow in the presence complex solid geometry was examined by simulating the flow of a liquid layer through the same arrangement of

cylindrical tubes and a dam break problem in the presence of a dyke. The large pressure drop across the bundle of tubes caused an increase in liquid height upstream of the bundle of tubes, which is physically reasonable. The motion of the water column in the dam break problem was in good agreement with the experiments. These tests confirmed that THAINC-IB preserves the sharpness of the interface within two cells even after large interface deformation.

In chapter 4, the effect of numerical treatments for evaluation of surface tension force on the prediction of the motion of gas-liquid interface of length scales varying from mili to sub-micron meters was investigated. Normal vector calculations based on the ALE like scheme and BFA, and interface curvature calculations based on CSF and HF were compared. First, simulations of a static circular drop of 1 mm in radius were carried out to validate the code. The results were the same as those in literature, *i.e.* the normal vector calculation based on BFA gives lower errors than the ALE like scheme, the interface curvature calculated using HF yields lower errors than CSF, and the errors are negligibly small when the theoretical value of curvature is used with BFA.

Simulations were carried out for smaller droplets ranging from a few micron to sub-micron meters to check the accuracy of the methods at such length scales. Numerical errors in the pressure and velocity remained at the same order even when the droplet size was reduced. Simulations of droplets adhering to walls were also carried out for the droplets of the same sizes to investigate the effect of wall treatment implementation on the accuracy. The errors in this case were also of the same order. The combination of balanced-force algorithm with height function for surface tension force calculation yields the lowest error.

The applicability to coating processes was checked by carrying out simulation of wetting of a solid plate by drops of mili and sub-micron meter size. The motion of a clean water drop of radius 1.14 mm on a solid plate was accurately predicted using the balanced-force algorithm with the height function and the dynamic contact angle model proposed by Yokoi *et al*. (2009). The smaller water droplet of radius 0.1 μm exhibited no oscillatory behaviour

in contrast to the larger drop due to stronger surface tension forces. HF with BFA predicted the contact angle in the equilibrium state better and caused smaller spurious currents than CSF with ALE.

In chapter 5, the effect of contamination on the motion of a drop on a solid plate was investigated. Falling drop experiments were carried out for water drops with different concentrations of surfactant. The data was obtained from the experiment using image processing. The adsorption-desorption equilibrium of the surfactant on the interface was confirmed by checking the effect of surface tension on the drop size at the time of detachment from the needle tip. Hence, the surface tension at different concentrations of the surfactant was estimated using von Szyszkowski's equation (von Szyszkowski, 1908). The contact angle was measured and modelled using the dynamic contact angle model proposed by Yokoi *et al.* (2009). The presence of contamination caused a reduction in the contact angle.

The motion of contaminated drop for c = 3, 6, and 10 mmol/m^3 on a solid plate was simulated and compared with the experimental results. The prediction using the balanced-force algorithm with the height function and the model of dynamic contact angle proposed by Yokoi *et al*. (2009) was in good agreement with the experiments. The wetting and dewetting motions were well predicted by only accounting for the surface tension reduction effects due to the surfactant and without solving the surfactant transport equation. Finally, the simulation of a coating process using an inkjet was carried out to demonstrate the applicability to industrial problems. The effect of surface tension on the injection of the fluid was investigated. The reduction in surface tension caused an increase in the time required for the droplet to pinch-off and also increased the number of satellite droplets which was consistent with the results reported in the literature.

In summary, THAINC-IB is proved to be an efficient method for the prediction of motion of gas-liquid interface, both clean and contaminated, of length scales varying from

mili to sub-micron meter in the presence of complex solid geometry while preserving the interface sharpness and volume conservation.

Appendix A

Height function for axisymmetric coordinates (Ferdowsi, 2012)

The heights used for curvature calculation are equivalent heights calculated from the total fluid volume in a stencil and can be computed in all directions of Cartesian co-ordinates by simply adding the volume fraction, Eq. (4.14), since the cross-sectional area is constant. Hence, Eq. (4.14) can be used for calculating the height in *z*-direction but not in *r*-direction since the cross-sectional area is dependent on *r*.

The calculation of height in *r*-direction requires a different calculation method to incorporate for the changing cross-sectional area of the computational cell in the *r*-direction. First, i_1 and i_0 for each individual stencil is identified, Fig. A.1, and then I_1 and I_0 is chosen from them such that all the three height calculations begin and end at the same location. The stencil which is sufficient to capture the interface is outlined with thick black line as shown in Fig. A.1. The total fluid volume within an individual stencil is computed by

$$\mathrm{V}_{i,j} = \sum_{k=I_1}^{k=I_0} \alpha_{k,j} 2\pi r_k \Delta r \Delta z \tag{A.1}$$

Two arrangements of the interface are possible where the dispersed fluid phase is closer to the axis of symmetry and vice versa as shown with Fig. A.1 (a) and (b), respectively. The effective height can be computed by satisfying the following condition for the former arrangement,

$$\left(\frac{r_0 + h_{i,j}}{r_0} \right)^2 = \frac{\mathrm{V}_0 + \mathrm{V}_{i,j}}{\mathrm{V}_0} \tag{A.2}$$

and

$$\left(\frac{r_0 - h_{i,j}}{r_0}\right)^2 = \frac{\mathrm{V}_0 - \mathrm{V}_{i,j}}{\mathrm{V}_0} \tag{A.3}$$

for the latter. r_0 is the distance of the starting point of the stencil, I_1, from the axis of symmetry and V_0 is the volume contained by r_0 computed by

$$\mathrm{V}_0 = \pi r_0^2 \Delta z \tag{A.4}$$

The interface normal used to compute the curvature is defined by

$$\boldsymbol{N} = \begin{cases} \left(\dfrac{\partial h}{\partial r}, -1\right) & \text{, stencil aligned with } z\text{ - direction} \\ \left(-1, \dfrac{\partial h}{\partial z}\right) & \text{, stencil aligned with } r\text{ - direction} \end{cases} \tag{A.5}$$

Substituting Eq. (A.5) into Eq. (4.12) yields

$$\kappa_{\mathrm{HF}} = \begin{cases} \dfrac{-\dfrac{\partial^2 h}{\partial r^2}}{\left[1+\left(\dfrac{\partial h}{\partial r}\right)^2\right]^{3/2}} - \dfrac{\dfrac{\partial h}{\partial r}}{r_i\left[1+\left(\dfrac{\partial h}{\partial r}\right)^2\right]^{1/2}} & \text{, stencil aligned with } z\text{ - direction} \\ \dfrac{-\dfrac{\partial^2 h}{\partial z^2}}{\left[1+\left(\dfrac{\partial h}{\partial z}\right)^2\right]^{3/2}} + \dfrac{1}{r_{\mathrm{int}}\left[1+\left(\dfrac{\partial h}{\partial z}\right)^2\right]^{1/2}} & \text{, stencil aligned with } r\text{ - direction} \end{cases} \tag{A.6}$$

where r_i is the distance of the cell (i, j) from the axis of symmetry and r_{int} the distance of the interface from the axis of symmetry given by

$$r_{\mathrm{int}} = \begin{cases} r_0 + h_{i,j} & ,\ N_r < 0 \\ r_0 - h_{i,j} & ,\ \text{otherwise} \end{cases} \tag{A.7}$$

The first and the second order derivatives of h, with respect to r and z, are computed by the second-order centred difference scheme using Eqs. (4.16) and (4.18), respectively.

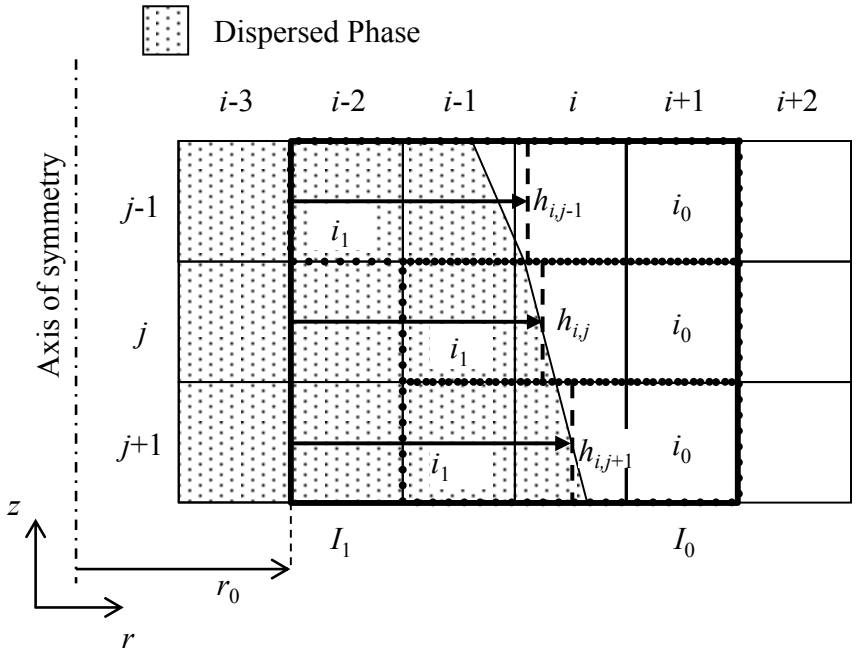

(a) Dispersed fluid phase closer to the axis of symmetry

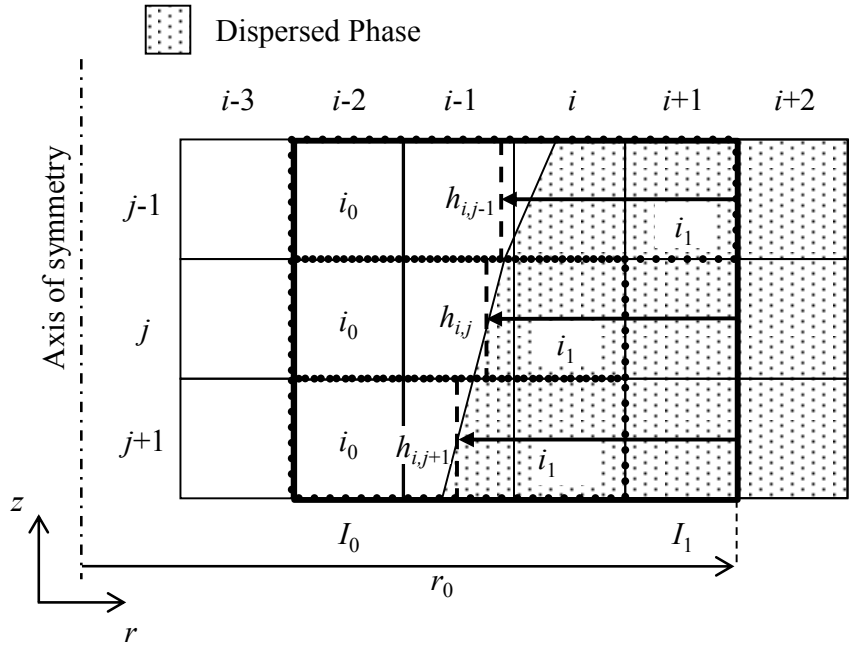

(b) Continuous fluid phase closer to the axis of symmetry

Fig. A.1 Height calculation for r-direction

References

Ferdowsi, P. A., Combined numerical and thermodynamic analysis of drop imbibition into an axisymmetric open capillary, PhD thesis, Graduate Department of Mechanical & Industrial Engineering, University of Toronto.

Acknowledgements

First of all, I would like to express deep gratitude to my supervisors Prof. Akio Tomiyama and Prof. Kosuke Hayashi whose continuous support, patient guidance and valuable suggestions have helped me to complete my studies. Their feedback has been instrumental in my growth as a researcher.

I am also grateful to my employer Sumitomo Chemical Co. Ltd., Japan for funding my studies at Kobe University. I would also like to thank my team members at Sumitomo Chemical for their support which helped me to maintain a balance between my work at Sumitomo Chemical and studies at Kobe University. I would like to specially thank Dr. Naoki Shimada for constantly providing constructive feedback and motivating me during this period.

I would also like to offer my special thanks to members of the laboratory of Energy and Environmental Engineering, Kobe University especially Masaaki Kitano, Shogo Hosoda and Shinpei Ojima for all their cooperation.

Finally, I would like to take this opportunity to thank my wife and family back in India for all their patience and love. Their support and encouragement have helped me to sail through the difficult times and been instrumental in lifting my spirits up whenever I felt demotivated.

Thank you all once again for all the help and support.

Abhinav Dhar

January, 2015

Doctoral Dissertation, Kobe University

"Interface tracking method for prediction of droplet motion in the presence of solid geometry", 137 pages

Submitted on January 20, 2015

The date of publication is printed in cover of repository version published in Kobe University Repository Kernel.

Following paper was submitted with the doctoral dissertation for doctoral dissertation defense.

N. Shimada, R. Saiki, A. Dhar, K. Mizuta, A. Tomiyama, "Liquid mixing in a bubble column", Journal of Chemical Engineering of Japan, 45(9), 632-638 (2012)
http://dx.doi.org/10.1252/jcej.12we021